# A MODELLING STUDY IN HARNESSING METAL-ORGANIC FRAMEWORKS FOR CHALLENGING GAS SEPARATIONS

CHRISTOPHER CAMPBELL

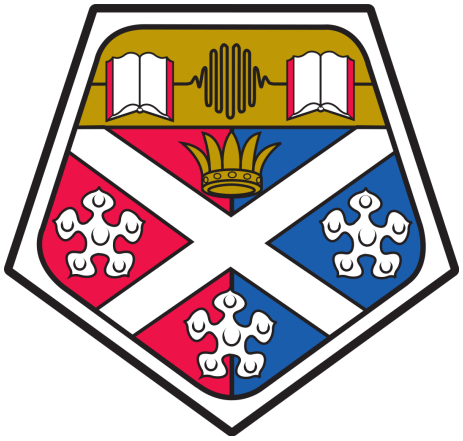

University of Strathclyde

Department of Chemical and Process Engineering

Doctorate in Philosophy

Dr. Miguel Jorge (First Supervisor)
Dr. Ashleigh Fletcher (Second Supervisor)

March 2018

Dedicated to the loving memory of Rena Mackinnon.

1930 – 2013

## ABSTRACT

The separation of gases is a complex and often expensive issue within industry, with energy-intensive distillation techniques often being the accepted solution. The discovery of tailorable Metal-Organic Frameworks (MOFs), however, is introducing an alternative route through separation techniques such as Pressure Swing Adsorption (PSA). Their tailorabiltiy promotes higher gas selectivities, the caveat is that experimentally assessing the full range of MOFs is unfeasible. Computational modeling could therefore be utilised to better evaluate the complete MOF pool. However, a unique subset of MOFs containing Coordinately Unsaturated Sites (CUS) are not well described computationally by standard forcefields. This work will therefore focus on developing a CUS model based off the work of Fischer et al.[1], which couples traditional modeling techniques with high level theory Quantum Mechanical (QM) methods, to tackle this challenging MOF class.

This thesis outlined a refined CUS model which was capable of capturing ethylene adsorption in HKUST-1. Furthermore, the model was able to use the same CUS parameters from HKUST-1 and transfer them to model other copper-paddlewheel MOFs. This adsorbent transferability is of especial importance for large-scale screening applications, limiting the required number of QM calculations for modeling CUS-containing MOFs. The new model also demonstrated marked improvement in simulating the binary adsorption of ethylene/ethane in HKUST-1, compared with standard forcefields. This validation was key as the main focus of this work was for application in multi-component systems, i.e gas separation.

The CUS model was also successful expanded to carbon monoxide adsorption, which required further development of the CUS procedure. The updated CUS model showed a large improvement in describing carbon monoxide adsorption behaviour in HKUST-1, over currently available models. Importantly, the adsorbent transferability, demonstrated for ethylene adsorption in copper-paddlewheel MOFs, was also retained using the updated CUS procedure.

The results of this computational study illustrate a new and exciting approach to capturing this complex CUS interaction. Furthermore, it highlights the great potential of MOFs in challenging gas separations.

# PUBLICATIONS

## 0.1 JOURNAL PUBLICATIONS

A Transferable Model for Adsorption in MOFs with Unsaturated Metal Sites: *Christopher Campbell, Carlos A. Ferreiro-Rangel, Michael Fischer, José R. B. Gomes and Miguel Jorge.*
*Journal: The Journal of Physical Chemistry C*

A New Model for Predicting Adsorption of Polar Molecules in MOFs with Unsaturated Metal Sites: *Christopher Campbell, Michael Fischer, José R. B. Gomes and Miguel Jorge.*
*Journal: Pending Acceptance*

## 0.2 ORAL PRESENTATIONS

British Zeolite Association: July 2015- Chester (England)

*Harnessing MOFs with Open Metal Sites for Challenging Gas Separations– A Monte Carlo Simulation Study*

`http://www.bza.org/annual-meeting`

Collaborative Computational Project 5: Sep 2015- Lancaster (England)

*A Study of MOFs with Open Metal Sites for Challenging Gas Separations*

`http://www.ccp5.ac.uk/events`

Fundamentals of Adsorption: May 2016- Friedrichshafen (Germany)

*A Study of Simulating Open Metal Sites in MOFs*

`http://dechema.de/en/foa2016.html`

Multifunctional, Hybrid and Nanomaterials: March 2017- Lisbon (Portugal)

*An Accurate and Transferable Molecular Model to Predict Adsorption in Metal Organic Frameworks with Open Metal Sites*

`http://www.hybridmaterialsconference.com`

Thermodynamics Conference: Sept 2017- Edinburgh (Scotland)

*An Accurate Molecular Model to Predict Competitive Binary Adsorption in Metal Organic Frameworks with Open Metal Sites*

`http://thermodynamics2017.efconference.co.uk/`

*In science one tries to tell people,*
*in such a way as to be understood by everyone,*
*something that no one ever knew before.*
*But in poetry,*
*it's the exact opposite.*

— Dirac [2]

## ACKNOWLEDGMENTS

C.C. thanks EPSRC for a doctoral training grant (EP/M506643/1 and EP/L505080/1). A visit of C.C. to Bremen was funded by the MAPEX Center for Materials and Processes, University of Bremen, through a Ph.D. Research Grant.

I would like to thank both J.R.B Gomes and M.Fischer for their insightful discussions and great help throughout my studies; as well as hosting me during my PhD studies.

I would also like to express my gratitude to both my supervisors, Dr. Miguel Jorge and Dr. Ashleigh Fletcher, for their constant support during my doctorate.

Finally, a thank you to my siblings; Tina, Jonny, Jamie, Niall and David; girlfriend Roisin; and to my mum and dad; for continually helping me during my long studies.

# CONTENTS

# LIST OF FIGURES

## LIST OF TABLES

## LISTINGS

Part I

# INTRODUCTION

This section will look into the structure that makes up Metal-Organic Frameworks (MOFs) and their potential role within industry as adsorbents. Furthermore, it will delve into some of the motivations behind better describing the adsorption mechanisms involving MOFs and more specifically the reason molecular modelling is required.

# 1

# INTRODUCTION

The research into Metal-Organic Frameworks (MOFs) has gained increasing interest within the scientific community in recent years.[3] These porous materials are made up of organic linkers and metal centres that can be combined into three-dimensional nanoporous polymer frameworks. The interest in these materials is primarily rooted in their very high attainable porosities and in their tailorability, derived from the various possible choices of organic ligands and metals that can create a variety of topologies and binding sites. The sheer number of MOF variations becomes apparent when looking at the Cambridge Structural Database, which currently contains over 50,000 MOF structures.[4] This number is expected to continue to grow rapidly with the development of computational software designed to identify potentially undiscovered MOFs.[5, 6]

The polymer's metal centre can be in the form of a metal ion or cluster. These metal centres are interconnected by organic linkers using metal coordination bonds, expanding the material into three dimensions, creating 3D cages which allow diffusion through interconnected pore windows. The organic linkers are predominantly made up of hydrocarbons, which can be extended in length, primarily through the addition of hydrocarbon groups such as aromatic rings, as in the case of the NOTT-100 MOF family.[7] This linker control therefore enables tailoring of the sizes of both these MOF pores and the windows which connect the pores, introducing the possibility of controlled diffusion effects for different adsorbate molecules.[8]

The control of the general structural characteristics and binding sites of MOFs, combined with the high porosities, provides exciting prospects for MOFs to be used in various applications. These materials are being actively researched for applications both in large scale processes such as catalysis, gas storage and adsorption separation, and also more specialised roles such as chemical sensors and

drug delivery vehicles.[9] While there is a great potential for MOFs to become important materials for a variety of industries, it should be remembered that their development is still very much in its infancy. Currently, one of the few MOFs to be manufactured commercially is HKUST-1 (Cu-BTC), sold under the name 'Basolite C300', which was only discovered and properly characterised in 1999.[10] As such, new MOFs are constantly being discovered and existing MOFs are continuing to be shaped into more suitable forms for a given application.

The research into MOFs is continuing to innovate with new pre/post synthesis techniques making MOFs more industrially attractive and interesting materials. For example, the organic linkers can be post-synthesis functionalised with a variety of groups, such as -OH, -Br and $NH_2$. This has been shown to increase the affinity of a MOF to certain compounds[11], improving their selectivity for practical gas separations. This control over binding sites has highlighted MOFs potential uses in applications such as catalysis[11], drug delivery[12] and as chemical sensors.[13]

Interpenetration is another phenomenon that can be found, and utilised, in MOFs where large void volume would have been found with the presence of only a single MOF structure.[14] Subsequently, additional overlapping MOF structures form to create an intertwining MOF lattice. This has the benefit of creating potentially stronger adsorption sites in the smaller pores and improves structural stability, but at the cost of a reduced pore volume.[14] This can again amplify effects for a desirable binding site by doubling their presence within a MOF lattice and also give some control over pore sizing, albeit not with much scope for small adjustments.

Another structural feature that can be found within MOFs is flexibility. This can occur when using certain organic linkers in which the linkers can reversibly collapse down into a closed pore state and also expand up into an open pore state, depending on the experimental conditions. The degrees of flexibility within MOFs vary considerably, in which some can be considered rigid, partially flexible (e.g ring rotation occurs) or fully flexible (e.g breathing, transforming between a fully open and fully closed state).[15] The potential triggers for changes in a flexible

MOF structure are many, including pressure, temperature and photosensitivity.[15] One of the most closely studied MOFs with regards to flexibility is MIL-53, which shows a 35% reduction in cell size between its open and closed states.[16] These large changes in MOF pores can lead to interesting adsorption isotherms, in which small changes of pressure can lead to dramatic uptakes in adsorption, as pores switch from the closed to open state. This response to pressure can be utilised within a number of applications, for example gas storage in which a high working capacity (difference of adsorbed amount) could potentially be achieved across a relatively small pressure range, if it falls within this flexible pressure region.

Additionally, some MOFs contain binding sites known as Coordinatively Unsaturated Sites (CUS), also known as Open Metal Sites (OMS). CUS occur when the metal within the MOF is not fully coordinated; this enables it to form strong coordination bonds with certain adsorbates such as unsaturated hydrocarbons through electron donation from the $\pi$ orbitals of the hydrocarbon to the metal site.[17] This unique adsorption mechanism puts CUS-containing MOFs in a prime position as potential adsorbents for gas separation processes. The CUS can exploit differences in electron donation capabilities for certain gas mixtures, such as ethane/ethylene[18], where only the ethylene gas will be able to form these coordination bonds with the MOF[19], producing a high gas selectivity. The formation and adsorption mechanisms for CUS will be discussed in much greater detail in Chapter 3.

It will be this latter phenomenon of CUS that will be the main focus of this thesis, relating to adsorption-based separation of gas mixtures. This is because currently within industry a large number of gas separations are achieved through energy intensive techniques such as distillation[20], which exploit differences in boiling points to separate the gas mixtures. This technique becomes very costly for gas mixtures when the components have similar boiling points, such as for ethane/ethylene mixtures in which this separation makes up 75-85% of ethylene production costs.[21] Therefore alternative gas separation techniques such as swing adsorption have the potential scope to greatly reduce the energy cost of various gas separations.

Swing adsorption separation works by exploiting the selectivity of the adsorbent for components of a gas mixture under given conditions. There are many variations, including Pressure Swing Adsorption (PSA), Temperature Swing Adsorption (TSA) and Vacuum Swing Adsorption (VSA).[22] In the case of PSA, to promote adsorption, high pressures would be used and then lowered during regeneration of the adsorbent. VSA can actually be considered a subset of PSA.[23] However, rather than operating at higher pressure and lowering to ambient, it adsorbs at ambient pressures and drops to very low pressure for the regeneration stage. Finally, TSA uses lower temperatures to increase adsorption for the separation stage, while higher temperature can be used for the desorption step.[24] Additionally, it should be noted that these swing adsorption processes can also be combined [25], perhaps requiring less extreme conditions than would be required individually or increasing effectiveness of the regeneration step.

These swing adsorption systems may all operate using the Skarstrom cycle, which has been used commercially, and therefore will be the procedure highlighted for these techniques,[26] albeit simplified. A gas mixture enters an adsorption chamber, at an extreme condition (i.e high pressure for PSA); the selected adsorbent should preferentially adsorb the unwanted component while enabling the desirable component to diffuse through. Eventually, the adsorbent will begin to saturate and the unwanted gas will breakthrough, at this stage the gas mixture should be redirected to a second adsorption chamber. While the second chamber is being utilised, the extreme condition in the first vessel should be reversed (i.e low pressure for PSA), enabling desorption of the unwanted component followed by venting [26]. The advantage of this procedure is that it enables the swing adsorption to operate as a cyclic process.

It should be noted that it is also feasible for the adsorbent to be preferentially adsorbing the wanted gas component, as would be the case in most ethane/ethylene gas separations using CUS-containing MOFs. This does however require a further desorption step, typically using an inert gas or applying vacuum, which would increase operating costs of the process.[27]

All the adsorption swing techniques mentioned will still share the same reliance on the selectivity of the adsorbent to make it a viable alternative to techniques such as distillation. The control over MOF structure and binding sites, already discussed, promote it as a viable candidate for various gas separations. The issue lies with how to assess potential adsorbent performance of such an intimidatingly large pool of MOFs. Experimentally, it would only be possible to evaluate a very small fraction of the available MOFs due to the time-consuming nature of adsorption experiments. Furthermore, there are various safety concerns associated with performing experiments at some of the more extreme adsorption conditions. For example, Tagliabuea et al. [22] highlight that assessment for natural gas purification would need to be conducted at pressure ranges across 3-17 bar to replicate the likely conditions for currently available industrial PSA equipment.

As such, there is potential for computational modelling to play a pivotal role in adsorbent material design, e.g. through high through-put adsorption screening of MOFs. This would be using computational modelling to identify the MOFs with the best selectivity for a given gas mixture composition through adsorption simulations. This computational screening could enable the large range of MOFs to be narrowed to a select few high-performing MOFs to be further studied using more traditional experimental methods, for a given application. This approach has already been suggested by groups such as Watanabe et al.[28] which examined the performance of 30,000 MOFs in $CO_2/N_2$ separation, before the highest simulated performers where experimentally evaluated. This approach not only enables a greater pool of MOFs to be investigated but, as mentioned, also has the key advantage of allowing hypothetical/unsynthesised MOFs to also be tested. This last advantage could become increasingly important due to recent developments in computational approaches, which enable vast numbers of stable hypothetical MOFs to be identified.[6, 28, 29]

This step into using computational screening of MOFs, however, has a strong reliance on simulations being able to accurately replicate the adsorption mechanisms and the MOF structures. The great number of unique structural and binding features found within MOFs introduces many layers of complexity to this endeavour. For instance, MOFs with interpenetration may not be 100 % interpenetrated, with some localised areas of the MOF still retaining the single MOF structure,[30] which would be challenging to properly account for within simulations. This defect type, as well as many others, are only just beginning to be understood in regards to both experiment and simulations. An interesting introduction to this subject can be found in works such as Fang et al.[30] and Sholl et al.[31]; the author would also recommend recent work by Sarkisov[32] which focuses on simulation techniques for accounting for defects.

The issue of accounting for flexibility is also a challenge when simulating MOFs. The inclusion of moving framework atoms within simulations requires a significant increase in computing power[33] as well as a reliance of proper models for describing the framework's structural behavior. Jimenez et al.[34] illustrated the need to properly account for flexibility within the simulation of flexible MOFs, showing that neither the open nor the closed state of the MOF ZIF-8 could adequately capture the full adsorption isotherm for nitrogen. One new approach has been proposed by Gee et al.[33] which uses a hybrid simulation method to efficiently capture flexibility, using a combination of Monte Carlo and Molecular Dynamics (explanations of these methods can be found in Chapter 2). The description of flexibility within simulations, however, still remains a complex challenge and will require a fine balance between accuracy and computing cost.

As mentioned, it is CUS in MOFs that will be the main focus of this thesis, which also causes complications within simulations. The challenge of simulating CUS comes from trying to account for the coordination bonding, found for some adsorbates.[1][35] Standard forcefields are not designed to account for this type of interaction and therefore can lead to very inaccurate predictions of adsorptions in this class of MOFs.[35] This deficiency regarding CUS-containing MOFs, for certain adsorbates, is well known in the research community, and therefore they are

routinely omitted in even recently published screening simulation papers.[36]

As such, this work will conduct an evaluation into the current performance of available molecular models for MOF adsorption with a focus on CUS-containing MOFs and their potential to be expanded to large-scale screening of MOFs, see Chapter 3. The first major aim of the project will be to develop a model capable of simulating individual olefin/paraffin adsorption isotherms on a wide range of MOFs. The adsorbates were mainly selected due to the availability of experimental data for comparison.[37] This validation into the transferability of the model is a key step, as without the model being transferable to other MOFs it cannot be applied in a large-scale screening approach. Subsequently, the model will be applied to predict competitive binary adsorption of olefin/paraffin (Chapter 4). Chapter 5 focuses on extending the model to cope with more polar adsorbates (e.g CO) in which electrostatic interactions play a key role. Finally, Chapter 6 will attempt to look into a new MOF structure which exhibits interesting structural properties, such as interpenetration and flexibility. Overall, the goal will be to develop a new model which provides detailed insight into the molecular level adsorption mechanisms on MOFs with CUS, and constitutes a useful tool to design new materials for challenging separations.

Part II

# BACKGROUND THEORY

This section will focus on two levels of simulation, namely Quantum Mechanics and Classical Simulations. The use of structural analysis software will also be discussed briefly at the end of the chapter.

# 2

# THEORY

This thesis uses two main theories in unison, quantum and classical. Quantum techniques make use of high levels of theory, as they rely on understanding the systems using quantum mechanics and therefore correctly describing the behavior of sub-atomic particles. This has the advantage of often being highly accurate and provides in-depth physical understandings of the underlying phenomena of interest. Therefore this theory can be used effectively to generate potential energy surfaces within a system. This approach, however, has the drawback of being very computationally expensive and time consuming, and therefore can usually only be applied to very small systems. This is turn means that it can be hard to relate quantum approaches to experimental observables.

Classical approaches are much more simplistic, they focus on describing the behavior of atoms/molecules or groups of atoms/molecules. This may initially not seem much lower level than that of quantum theory, but the reader must appreciate the sheer number of sub-atomic particles in a group of atoms and the difficultly in attempting to capture how they all interact simultaneously. Classical methods enable the user to study much larger systems and therefore, through the use of thermodynamics and statistical mechanics, relate simulations to experimentally relevant properties and observables. The drawback of this is that the way in which atoms/molecules interact must be correctly described, and this can be challenging with simplistic representations of atoms/molecules. Therefore there is a constant balance to be found within classical theory between accurately representing the system while retaining low computational cost to enable the theory to be applied to large enough systems. Often these interactions are derived empirically, tuning atomistic interactions in an attempt to replicate experimental properties.

The background theory behind these two main methods utilised in this project will be discussed within this section; however this is not meant to be a comprehensive explanation of these approaches and, as such, relevant external resources will be suggested at the appropriate points of each section. Additionally, some of the more general inputs for the software may be elaborated within. The more specific details of simulation/calculation inputs can be found within the relevant results chapters.

## 2.1 CLASSICAL SIMULATIONS

This section will provide a brief explanation of the foundation behind classical theory and the requirement for a model to describe a simulated system. Due to quantum theory being higher level it should likely be described first. However, classical theory is the main basis of this thesis and introduces some key concepts utilised in both theories more seamlessly.

### 2.1.1 *Simulation Methods*

In experiments, a thermodynamic macrostate property at equilibrium, such as temperature, is normally averaged across a given time to ensure the correct equilibrium value is measured. This is important as the macrostate property is really a reflection of a collective set of microstates, e.g the velocity of a group of molecules, which will continually fluctuate over time. Molecular dynamics (MD) is a simulation technique that utilises this idea of averaging a set of microstates over time to predict macrostate properties. For instance, a MD system could be set up and the average temperature calculated based on the number and speed of the molecules present, utilising Newton's equations of motion.[38] If a heat source were to be added, not only could the new equilibrium temperature be found but also the evolution of temperature gradient within the system with respect to time. This is a major advantage of MD simulation; it enables not only equilibrium properties to be studied but also the stages before equilibrium is reached. The drawback of this is that attaining equilibrium can be very time consuming, especially as systems grow in size to better reflect a real system.

Therefore, when it is only the final equilibrium value of the thermodynamic property which is of interest, this computer cost associated with the pre-equilibrium stage of MD can sometimes be reduced by using a different technique called Monte Carlo (MC).

MC is different to other simulation techniques as it does not follow the concept of time. Whereas, in some simulations, the complete history of the system affects its path and trajectory, the MC method relies only on the previous state.[39] This means the molecules do not need to follow a physically realistic trajectory but can be instantly transported to a new location. This enables equilibrium to be achieved much faster as the full trajectories of each atom do not need to be followed towards equilibrium, greatly reducing simulation time. This can be advantageous for certain cases, for example in which there is a gas adsorbing in a MOF with an accessible pore but only through a very constricted pore window. In MD simulations it would take a very long time for the system to reach equilibrium as diffusion through that window will require very specific orientations/energies from the MOF and adsorbates. This is not an issue for MC as the adsorbate can be translated and inserted directly into that pore space, reaching equilibration much faster. However, in this scenario if the pore window was actually too constricted to enable diffusion through, when using molecular dynamics (MD) if an adsorbate molecule tried to fit through the cage window it would be, correctly, unable to enter the cage, as it would first have to be in a state were it overlapped with framework atoms. However, in MC the pore space would still be available if the pore was large enough to fit adsorbate molecules and therefore it would lead to overestimation of adsorption capacity. It should be noted, that this MC issue can be solved by inserting a blocking atom into the inaccessible cages within the framework structure, a technique discussed later within this thesis (Chapter 3).

### 2.1.2 *Statistical Mechanics and Ensembles*

A link is required between the microstates simulated in MC and MD simulations, and the macrostate properties wanting to be studied, which is found in statistical mechanics. An ensemble is defined as a large collection of microstates used to replicate a given system's macrostate, therefore depending on the system wanting to be studied a different ensemble is used. The system being simulated can have a variety of thermodynamic constraints set; Energy (U), chemical potential ($\mu$), temperature (T), pressure (P), number of particles (N) and volume (V). Generally, three variables are kept fixed, allowing the relationship between certain unfixed variables to be investigated, each of these variations represents a specific ensemble type. According to the first postulate of statistical mechanics, if the microstates have the same energy, volume, and number of particles, then they occur with equal frequency in the ensemble.[40] From this it can be deduced that the time averaged macrostate properties being studied are equivalent to the average of a large enough ensemble[38], becoming exact as the ensemble size (i.e the number of microstates) tends towards infinity; this concept is known as ergodicity. This relationship can be better seen in Equation 1, for variable V at microstate i and where $P_i$ is the probability of that microstate occurring within the ensemble:

$$\overline{V} = \langle V \rangle_{Ensemble} = \sum_{Microstates}^{\infty} V_i.P_i \tag{1}$$

This Equation draws a parallel between experiment and simulation, as much as in experiments the variable must be averaged over a long enough time to ensure equilibrium, $\overline{V}$; MC simulations must be sampled over a large enough ensemble.

One of the most used ensembles is the Canonical Ensemble, which refers to a system with a constant N, V and T. This can be visualised as a constant volume system surrounded by an infinite reservoir with which it can exchange energy, thereby enforcing the constant temperature of the system. As the system is now able to exchange energy, each microstate within the system has an associated probability of occurring, based on its corresponding energy via the Boltzmann factor.

[38] The collection of all possible microstates is known as the partition function, shown in Equation 2.[41]

$$Q(N, V, T) = \frac{1}{\Lambda^{3N} N!} \int dr^N \cdot exp[-\beta \cdot U(r^N)] \tag{2}$$

where

- $Q$ Partition Function
- $\Lambda$ Thermal de Broglie Wavelength
- $\beta$ $1/k_b.T$ ($k_b$ is the Boltzmann constant)
- $U$ System Energy
- $r$ atom-atom distance
- $N$ Number of atoms

It follows therefore that the probability of a microstate, i, can be expressed as a ratio of its energy against that of the partition functions, shown in Equation 3.[40] The partition function's role is to act as a normalising factor, relating the energy of the microstate i to that of every possible microstate within the system.

$$P_i = \frac{exp(-\beta(U_i))}{\sum_j exp(-\beta(U_j)} \tag{3}$$

where

- $P$ Probability
- $i/j$ microstates

This concept of probability is utilised within the Metropolis method for Monte Carlo (MC) simulations.[42] In the Canonical ensemble, no atoms can be added or removed, but simply moved. The Metropolis method outlines a procedure to decide when a move is accepted, which is based on the old and new systems' energy:

1. Select a random particle and calculate its current energy $U(r^N)$
2. Displace the particle position by $\vec{\Delta}$.
   ($r' = r + \vec{\Delta}$). Then calculate this particle's new energy $U(r'^N)$
3. Accept the move with the probability based on the equation:

$$acc(r \rightarrow r') = min(1, exp(-\beta[U(r'^N) - U(r^N)])) \tag{4}$$

4. Generate random number (Ranf) between 0-1
5. If Ranf < acc ($r \rightarrow r'$) then accept move

The acceptance ratio (acc) in Step 3 sets the probability of the translation move being accepted. If there is a drop in energy after the move then the move will always be accepted, as $acc(n \rightarrow' n)$ will equal one and therefore will always be greater than Ranf. If there is not a drop in energy after the move then it will have a probability of being accepted based on the Boltzmann factor within Equation 4, becoming less likely to be accepted the more unfavourable the move.

The use of random numbers to introduce probability into the acceptance ratio is key as it enables unfavourable moves to also be accepted. This is important as the system must be ergodic (every microstate must be accessible within a finite number of MC steps).[41] This probability also allows energy barriers to be overcome in certain situations and local minima escaped, so that even more favourable states may be found, which involve a temporary unfavourable position. The use of probability, however, has a strong reliance on the random number generator in step 4, if it does not generate numbers between 0-1 uniformly then it will introduce a bias which could lead to incomplete sampling of the microstates.

The Canonical Ensemble can be used to derive various other useful ensembles; the one utilised within this thesis is known as the Grand Canonical ensemble. This ensemble swaps the constraint on N for $\mu$, making the system fix $\mu$, V & T (rather than N, V & T). This can be visualised as a constant volume system surrounded by an infinite reservoir with which it can exchange both energy and molecules. Thereby, enforcing the constant temperature and chemical potential of the system,

while allowing number of atoms to fluctuate. This leads to a slightly more complex partition function (Equation 5) than found in the Canonical Ensemble (Equation 2), as the new functional must account for fluctuations in the number of atoms in the system.[41]

$$Q(\mu, V, T) = \sum_{\infty}^{N=0} \frac{exp[\beta \cdot \mu \cdot N]V^N}{\Lambda^{3N} N!} \int dr^N \cdot exp[-\beta \cdot U(r^N)] \tag{5}$$

where

$\mu$ Chemical potential

Monte Carlo again can probe this system using random steps, however, now there are three move types; consisting of insertions, deletions and translations of molecules.[41] The probability of accepting each of these move types will again relate to system energy depending on the Boltzmann distribution (as previously seen in Equation 3), but will also require a new term considering the chemical potential and number of molecules within the system. Equation 6 shows the relationship between probability of state i occurring within the Grand Canonical system (based on the new partition function in Equation 5):

$$P_i = \frac{\frac{V^N}{\Lambda^{3N} N!} \cdot exp(-\beta(U_i - \mu.N_i))}{Q(\mu, V, T)} \tag{6}$$

This probability distribution shown in Equation 6 leads to the acceptance criteria for each of the move types using the same metropolis method illustrated previously for the Canonical ensemble. In Equation 7, it can be seen that the acceptance ratio is exactly the same as in the Canonical example, this is because no atoms are being created or destroyed meaning a term relating to number of molecules is not required. In Equations 8 and 9, a new term must be included to account for the volume (V) freed up or taken by these move types.

**Translation:**

$$acc(r \rightarrow r') = min(1, exp(-\beta[U(r'^N) - U(r^N)])) \tag{7}$$

**Insertion:**

$$acc(N \rightarrow N+1) = min(1, \frac{V}{\Lambda^3(N+1)} exp(-\beta[\mu - U(N+1) + U(N)])) \tag{8}$$

**Deletion:**

$$acc(N \rightarrow N-1) = min(1, \frac{\Lambda^3 N}{V} exp(-\beta[\mu + U(N-1) - U(N)])) \tag{9}$$

This section briefly covered the Canonical and Grand Canonical ensembles as they are the most relevant to the work conducted in this thesis. However, it is worth noting there are many other important ensembles; such as the isothermal-isobaric ensemble which keeps temperature, pressure and number of particles constant. This enables the study of the relationship between system energy and system volume. For a more detailed discussion of ensembles the author would suggest the work by Frenkel et al.[41] and a more recent publication by Tuckermann et al.[43]

### 2.1.3 *Models*

In the previous section, the conditions for acceptance of moves were discussed, which required the energy of the system to be known. This entails determining the change in potential energy within the system after a move. For example, if a molecule is moved across a system (translated) the potential energy change will be calculated by comparing the molecule in both the old and new molecule positions, based on the attractive/repulsive relationship between this molecule and the surrounding atoms already in the system. However, before delving into how this potential energy is calculated it is important first to know the types of interactions which make up these attractive/repulsive effects. There are four main intermolecular (non-bonding) forces which we group under the term 'van der Waals' forces:

1. Pauli Exclusion Principle- This principle states that two or more electrons cannot share the same quantum state, preventing molecules from collapsing. This is the repulsive term within van der Waals Forces; it relates to the large repulsion felt between atoms when their electron clouds begin to overlap and therefore occurs at short atom-atom distances.

2. London Dispersive Forces- This is a weakly attractive force occurring from electrons in adjacent atoms forming temporary dipoles instantaneously, for both polar/non-polar molecules. This interaction is created by induced dipoles which will dissipate if the atoms move away from each other.

3. Electrostatics- This force can be either attractive or repulsive. It occurs from the interaction between molecules' permanent multipoles, as well as charged ions. When positively charged sites approach negatively charged sites it is an attractive interaction, whereas if the two sites have the same charge then it will be repulsive. Generally, for molecules the forces are attractive as the molecules can orientate themselves in such a way as to enable opposite poles to be facing each other.

4. Polarization- This is an attractive interaction. It is the interaction between permanent multipoles and induced multipoles. As a polar molecule approaches a polarisable molecule it induces a temporary complementary dipole, much like in the London Dispersive forces in which it is two polarisable molecules approaching each other.

#### 2.1.3.1 *Repulsive & Dispersive Interactions*

In molecular simulation the repulsive 'Pauli Exclusion Principle' and attractive 'London Dispersive Forces' are usually described together through the use of the Lennard Jones (LJ) potential, shown in equation 10.

$$U = 4\epsilon\left[\left(\frac{\sigma}{r}\right)^{12} - \left(\frac{\sigma}{r}\right)^{6}\right] \tag{10}$$

where

$r$ Interacting atom-atom distance

Its two main parameters can be seen in Figure 1, where epsilon ($\epsilon$) represents the attractive depth and sigma ($\sigma$) represents the separation distance at which the potential energy equals zero. The sigma value effectively denotes the end of the repulsive region, were orbitals of the two molecules would no longer overlap. The $r^{-12}$ term in Equation 10 refers to the Pauli repulsion interaction, whereas $r^{-6}$ is the dispersive interaction. One additional parameter used is a high cut-off, shown in Figure 1. Due to the large power terms, on both the interactions, the interaction energy decays quickly in relation to r. Therefore calculations can be stopped at relatively short distances as the LJ potential becomes insignificant. This greatly improves computing efficiency. Additionally, it should be noted that there are many other potentials such as Buckingham[44] or Morse[45], but LJ potential is by far the most common to represent these interactions.

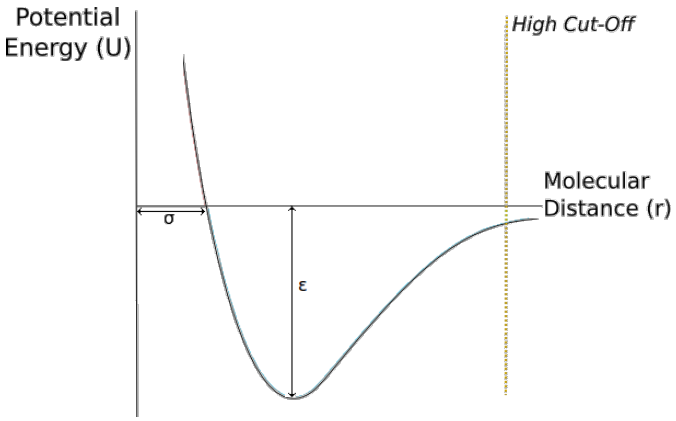


Figure 1: Illustration of LJ potential.

A collection of sigma and epsilon values for each atom type is known as a forcefield. There are many different forms of forcefields which control various aspects of a molecular system; from bond strength, bond angles to non-bonded interactions. In this work's GCMC simulations, when referring to a forcefield it relates to how an atom or collection of atoms interact. For example to simulate how a framework's copper atom and oxygen adsorbate atom (e.g from a water molecule) would interact, you have to obtain the forcefield values for copper and the forcefield values for oxygen from a water model. To predict how they would interact you would mix these values; commonly this is done through the Lorentz-Berthelot combining rules, shown below:

$$\sigma_{ij} = \frac{\sigma_i + \sigma_j}{2} \tag{11}$$

$$\epsilon_{ij} = \sqrt{\epsilon_i \cdot \epsilon_j} \tag{12}$$

#### 2.1.3.2 *Electrostatics and polarization*

The interaction of both electrostatics and polarization require a polar molecule or ion, therefore for adsorption in MOFs if the adsorbate molecule is non-polar (e.g methane) then these interactions can be ignored. For polar adsorbates, the electrostatic interaction of two atoms can be determined using Coulomb's law:

$$U_{Elec} = \frac{q_i \cdot q_j \cdot e^2}{4\pi \cdot \epsilon_0 \cdot r} \tag{13}$$

where

- $i/j$ Different atoms
- $q$ Static point charges
- $r$ Pairwise atom-atom distance
- $e$ Elementary charge ( 1.60217662 x $10^{-19}$C)
- $\epsilon_0$ Vacuum permittivity (8.854187817 x $10^{-12}$ F.m$^{-1}$)

The polarization interaction, on the other hand, is very complex and computationally expensive to calculate. This is due to a polarization interaction being heavily dependent on the effects of various surrounding atoms simultaneously, therefore it must be solved using a many-body approach rather than pairwise. It is therefore normally accounted for using an effective point charge, implicitly determining the polarization effects within the point charges of the electrostatic calculation. The advantage of this approach is that it is simple to incorporate into existing simulations and greatly saves on computational cost. However, it should be noted that it is an estimation and the importance of polarization could be expected to increase with more polarizable molecules. There are a few research groups calculating polarization interactions explicitly relating to MOF adsorption, such as Pham et al.[46]

The electrostatic interaction has a very slow decay with respect to potential energy across the particle pairwise distance. This means that for a 3D GCMC system where periodic boundary conditions are used, Equation 13 would lead to a poorly converging sum (a brief explanation of periodic boundary conditions can be found at the end of this section). Therefore the truncation method (high cut-off) used with

the LJ potential should not be applied, as doing so would introduce a large error due to a significant portion of potential energy being unaccounted for within the system. One of the most commonly used solutions to this issue is the Ewald summation[47], which calculates the full electrostatic potential by treating the long and short range interactions independently.

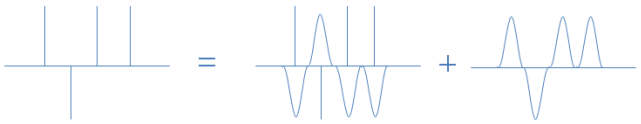

Figure 2: Representation of the Ewald Summation.

Firstly, the Ewald summation assumes that the system has a net neutral charge. It surrounds each point charge (Particles i with charge $q_i$, Equation13) within the system with an equal and opposite charge distribution, such that the sum of this charge distribution will cancel out $q_i$. This charge cloud is represented by the common Gaussian distribution, shown in Figure 2 . The resulting potential attributed to a charged and screened particle decays quickly to zero across large distances, meaning they can be summed without large associated computing costs.

This charge screening distribution must then be determined to isolate the potential relating solely to the point charges, this is illustrated in Figure 2. This compensating charge distribution is calculated using a rapidly converging Fourier series.[41][38] The final form of the Ewald summation can be seen below:

$$U_i = \frac{1}{2}\sum_{j=1}^{N}\frac{q_i \cdot q_j}{4\pi\cdot\epsilon_0}\left(\underbrace{\sum_{|n|=0}^{\infty}\frac{\operatorname{erfc}\left[\frac{|r_{ij}+n|}{\alpha}\right]}{|r_{ij}+n|}}_{\text{Real Space}} + \underbrace{\frac{4\pi}{V}\sum_{k\neq 0}\frac{\cos(k\cdot r_{ij})}{k^2}\cdot e^{-\frac{k^2\cdot\alpha^2}{4}}}_{\text{Fourier Space}}\right) + \underbrace{\frac{q_i^2}{4\pi\cdot\epsilon_0\cdot\alpha\cdot\sqrt{\pi}}}_{\text{Self-Correction Term}} \tag{14}$$

where

| | |
|---|---|
| $1/2$ | Factor accounts for double counting (summing) of $i/j$ interactions |
| $q_{i/j}$ | Point charges |
| $r_{ij}$ | Pairwise distance |
| $V$ | Unit cell volume ($L_x \cdot L_y \cdot L_z$) |
| $n$ | Real space lattice vectors ($n_x L_x \cdot n_y L_y \cdot n_z L_z$) |
| $\alpha$ | Gaussian width for screening (higher value, higher computing cost) |
| $k$ | Fourier space lattice vectors ($2\pi\frac{k_x}{L_x} \cdot 2\pi\frac{k_y}{L_y} \cdot 2\pi\frac{k_z}{L_z}$) |

In Equation 14, the Fourier term is solving the charge screening distribution within Fourier space and then converting it into real space. This enables the real space term to only have to deal with the quickly converging short range electrostatic interactions. The final term is simply used to correct for atom self-self interaction which would be counted within the former summations. Overall, this technique enables electrostatics to be calculated with high accuracy, while remaining computationally efficient. This should be considered a brief overview into the Ewald summation; the author would recommend introductory works such as Toukmaji et al.[47] and for a more in-depth look into derivation of the relevant equations, Lee et al.[48]

#### 2.1.3.3 *Elecrostatics- Wolf Summation*

The Ewald summation was the main technique used within this work for calculating MOF-adsorbate interactions, as accurately capturing this relationship is key to correctly describing adsorption (especially at low coverage). Although Ewald summation was designed to balance computational cost with accuracy, it is still a relatively computationally expensive technique. This becomes an issue when inserting a high number of adsorbates as the adsorbate-adsorbate interaction rapidly increases. As such, a method called the Wolf summation is used to describe these interactions. The Wolf summation is a much newer method than that of Ewald summation, proposed by Wolf et al.[49] in 1999. It has many similarities to that of the Ewald summation and therefore only the major assumptions behind the method will be discussed.

A major issue with any truncation within electrostatics is that the interaction sphere selected will almost never be neutral.[49] Wolf et al. overcome this issue of truncation by utilising a term to always neutralise the system no matter the cut-off selected. This term is found by observing that it is the outer charges on the surface of the interaction sphere that cause this imbalance. Therefore by removing the energy of the surface of the interaction sphere, the neutral energy inside the sphere can be determined[50]:

$$U_{Elec,Neutral} = \underbrace{\frac{1}{2}\sum_{i=1,j\neq i}^{N}\sum_{r_{ij}<R_{cut}}\frac{q_i \cdot q_j}{r_{ij}}}_{\text{Energy of Whole Sphere}} - \underbrace{\lim_{r_{ij}\to R_{cut}}\frac{q_i \cdot q_j}{r_{ij}}}_{\text{Energy of Sphere Surface}} \tag{15}$$

where

| | |
|---|---|
| $1/2$ | Factor accounts for double counting (summing) of i/j interactions |
| $q_{i/j}$ | Point Charges |
| $r_{ij}$ | Pairwise Distance |
| $R_{Cut}$ | Cut-off Radius for Interaction Sphere |

This shifts the sphere energy away from the true value by a constant, which is corrected using the term below:

$$U_{Elec,Shift} = \frac{1}{R_{Cut}}\sum_{i=1}^{N} q_i^2 \tag{16}$$

The Wolf summation in this form however would require a prohibitively high value of $R_{Cut}$ for acceptable convergence [50], greatly increasing computing cost. As such, a damping factor ($\alpha$) is used to compensate for lowering $R_{Cut}$, in which high values of the damping factor allow smaller $R_{Cut}$ to be applied. The final form of the Wolf summation is as follows:

$$
\begin{aligned}
U_{Elec,Neutral} = & \frac{1}{2} \sum_{i=1, j \neq i}^{N} \sum_{r_{ij} < R_{cut}} \frac{q_i \cdot q_j}{r_{ij}} \cdot (erfc(r_{ij}\alpha)) \\
& - \lim_{r_{ij} \to R_{cut}} \frac{q_i \cdot q_j}{r_{ij}} \cdot (erfc(r_{ij}\alpha)) \\
& - \left( \frac{(erfc(r_{ij}\alpha))}{R_{Cut}} + \frac{\alpha}{\sqrt{\pi}} \right) \sum_{i=1}^{N} q_i^2
\end{aligned}
\tag{17}
$$

The final Equation 17, leads to a computationally fast method of determining electrostatics, however as it is not exact (unlike Ewald summation) it was only utilised for the adsorbate-adsorbate interaction. Although, in this work it has been decided to use both the Ewald and Wolf summations, studies involving MOFs have shown that the drop in accuracy for using just Wolf summation is not significant.[51]

### 2.1.4 *Computational Techniques*

This section will briefly elaborate on a number of techniques used within the GCMC simulations to improve computational efficiency.

#### 2.1.4.1 *Periodic Boundary Conditions*

The early sections tried to illustrate how simulations could replicate real experimental systems, this however did not address the question of how to feasibly simulate such a large system. The technique called 'periodic boundary conditions' is often used, in which a small unit cell is mirrored in each of its axes (for adsorption in 3D MOFs this will be x, y, z). This can be better visualised in Figure 3, which shows the unit cell (boxed) being replicated in 2 dimensions. When a molecule passes through a boundary wall it will be translated to the opposite side of that wall's boundary, as illustrated by the dotted line molecule in Figure 3. This technique is often used to simulate bulk fluids, however it is also especially effective for the MOF crystal structures being used within this work. This is because the MOF is essentially a small unit cell being replicated constantly and therefore can be simulated by making the simulated unit cell the smallest repeating unit of the MOF. When the atom passes through the boundary wall and re-enters the opposite unit cell wall it is effectively in the same surrounding MOF environment it would have found itself if it simply moved through a larger unit cell.

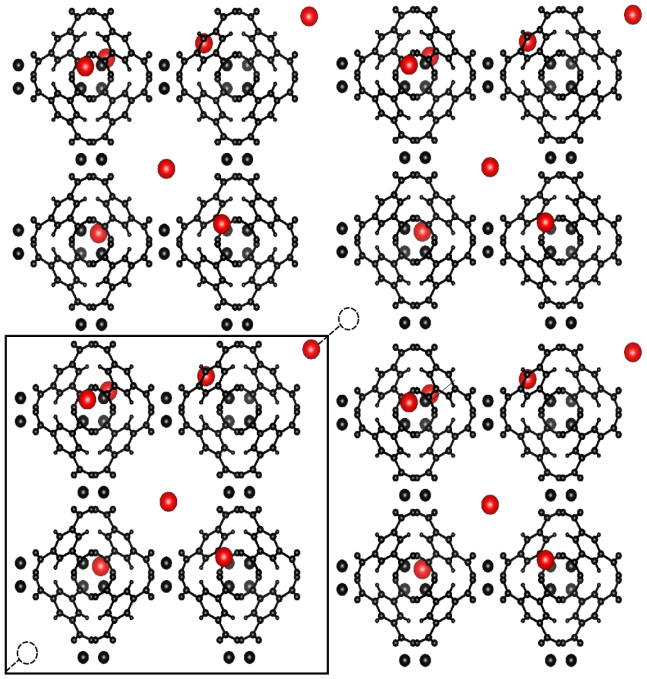

Figure 3: Illustration of periodic boundary conditions for a GCMC adsorption system (black- MOF atoms, red- adsorbate atom ).

It therefore allows infinite systems to be simulated while the simulation only holds a finite amount of real atoms (i.e within the box), vastly saving on computational power required. However, when using this technique it is important that 'finite size effects' do not occur; this means that the size of the initial unit cell does not affect the outcome of the simulation. Essentially, the unit cell must be large enough that it can replicate a real system. This can be tested by increasing the unit cell size, if the initial cell is large enough the outcome of the simulation should not be affected.

#### 2.1.4.2 *Potential Mapping*

The technique of potential mapping is an important method within GCMC simulations to save on computing costs. A potential energy map (PMAP) is created for each type of LJ interaction site within the adsorbate (i.e carbon dioxide would require, 1x carbon PMAP and 1x oxygen PMAP). It is formed by inserting an individual LJ site into the unit cell and translating it within an even spacing to form an energy grid, see Figure 4. Therefore, during simulations when the same interaction

site is inserted it can calculate the adsorbate-adsorbent interaction strength from interpolation of the nearest grid points in the relevant PMAP, rather than doing a full LJ calculation for all surrounding atoms. The initial computing cost of creating the pmaps is greatly offset when multiple simulations are required to be run. In the case of adsorption simulations, multiple pressure points are required and often at different temperatures, all of which can use the same PMAPs. However, the grid points within the pmap must be fine enough to enable accurate interpolation, with a finer grid requiring higher upfront computing costs.

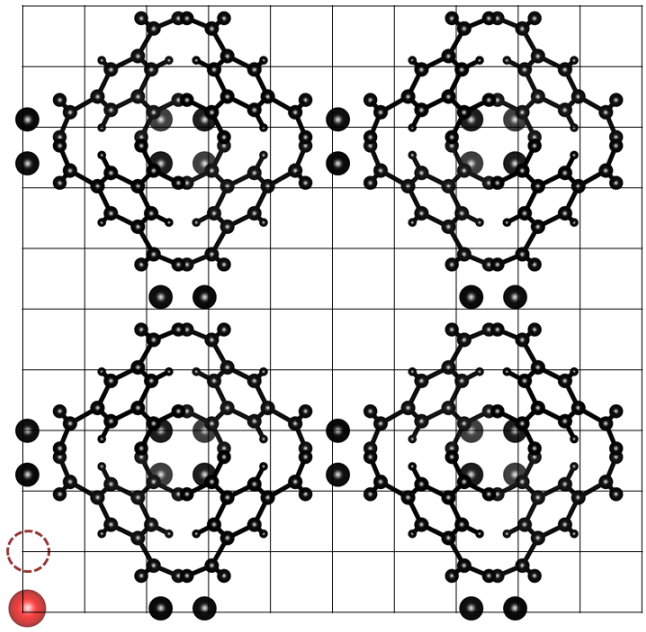

Figure 4: Illustration of creation of a pmap within a grid for a GCMC adsorption system (black- MOF atoms, red- adsorbate atom ).

This technique is also used for electrostatics, known as an EMAP. However, within electrostatics only one emap is required, formed by a probe atom, which is a pseudo-atom that has no LJ parameters but has a point charge of +1.0. This is because the only changing variable for different electrostatics sites in an adsorbent would be the point charge (rather than in LJ sites where it would be both $\sigma$ and $\epsilon$), therefore each electrostatic interaction site can be directly scaled against just one EMAP. This is especially useful for EMAPs due to the high computing costs associated with their calculation.

#### 2.1.4.3 *Biasing*

In GCMC simulations, it has been so far discussed as completely randomised moves probing the given system. This leads to a large number of wasted move attempts as the method probes areas/configurations in which the move type would be highly unlikely to be accepted (e.g trialling moves on top of existing framework atoms). One of the major advantages of using MC techniques is biasing, which can be implemented to improve the number of accepted moves, thereby greatly increasing the speed of simulations.[41] One such technique is configuration biasing; this separates a trial molecule's potential based on orientation dependent and independent parts. It then trials a number of orientations for the molecule and improves the likelihood of an energetically favourable orientation to be generated. In any form of biasing, however, the acceptance rules must also be altered to ensure that the likelihood of reversibility of GCMC is maintained, and that the system is correctly sampled.[52]

Snurr et al.[52] proposed a cavity bias which can be especially useful in adsorption simulations, greatly increasing the likelihood of inserting moves being accepted. It probes a number of possible insertion points to evaluate if there is a sufficiently large enough radius to accept an inserted molecule, it then randomly selects one of the suitable cavity points. In this work a similar technique is used based on potential energy, obtained from potential maps. This biasing uses the potential of the maps to identify highly favourable unit cell points for the given adsorbate and prioritises these sites for certain move types. The only biased move types used in this thesis's GCMC simulations are the insertion and deletion moves. Both these becomes increasingly important the more densely packed the unit cell becomes, the cost being a more complex acceptance procedure.

### 2.1.5 *Forcefields*

In the Models Section, the use of forcefields to describe the interactions between atoms/molecules has been discussed. However, how these forcefields are formed has not been elaborated on. Generally, there are two main routes to parameterising a forcefield. One is tuning the forcefields empirically in an attempt to replicate an experimental observable or various experimental observables. This can lead to various different parameters being generated for the same atom, depending on the desired experimental property/properties to be matched against. Another, more recently used, route is to use high level theory such as quantum mechanics to tailor the forcefield against.

In general, to describe van der Waals interactions it is the former method that is utilised. For instance, TraPPE aims to quantitatively replicate phase equilibria and various other thermophysical properties while limiting the use of pseudo-atoms[53][54], forcefield sites which don't relate to the physical presence of an atom. Furthermore, some of these forcefields attempt to implicitly account for electrostatic interactions, thereby substantially saving on computing power by not having to explicitly calculate electrostatics techniques, through methods such as Ewald/Wolf summations.

The right forcefield to use therefore depends on the desired output and also the system conditions being used. For the framework atoms in this work, two well known forcefields will be used, the Universal Force Field (UFF) [55] and DREIDING [56], due to their extensive use in describing adsorption in MOFs.[57] UFF is required as the DREIDING forcefield does not contain many values for metals which are commonly found in MOFs. Due to the number of different adsorbates being used, the forcefields utilised will be listed within their relevant chapters, however the Transferable Potentials for Phase Equilibria (TraPPE[53]) is one of the most common.

#### 2.1.5.1 *United Atom*

In the aforementioned forcefields, the use of united atoms is a common technique within molecular simulations to increase computational efficiency. Essentially, a collection of atoms in a molecule are grouped into one single bead and treated as one interaction site. This greatly reduces the number of interactions required to be calculated, saving on computing power. The single site is then re-parameterised to accurately replicate the effective binding characteristics of the group of atoms (i.e in LJ potential $\sigma$ and $\epsilon$).

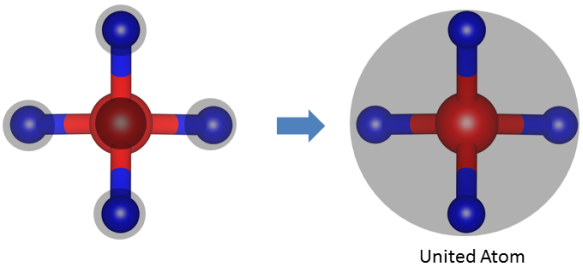


Figure 5: Methane represented by 5 atomic sites (left), coarse grained methane represented by 1 atomic site (right).

An example of this can be seen in Figure 5, which shows the united atom representation of methane found in the TraPPE forcefield. The methane is reduced from five interaction sites to just one. However, the detailed shape of the methane molecule is lost and, therefore, orientation of the methane molecule will not be captured in the simulation. This is an important point, as it highlights that in systems where orientation of the molecule is key then care must be taken when using coarse-graining. Finally, it is important not to group too many atoms within a single bead as too much structural information of the molecule may be lost and description of the effective binding characteristics of all the atoms will be poor. Still, these coarse grained forcefields have been shown to perform well for various small olefin and paraffin adsorbates in adsorption in MOFs[18][1][58], which will be a major focus of this work.

#### 2.1.5.2 *Point Charges*

When a van der Waals forcefield does not include electrostatics implicitly, depending on the adsorbate, the electrostatic interactions will likely need to be explicitly determined. In GCMC simulations this is commonly done through the use of point charges (see Ewald section), in which atoms and pseudo-atoms are assigned a charge to attempt to replicate the system's electrostatic behavior. Similar to van der Waals forcefield parameterising this can be done through semi-empirical/empirical fitting to replicate an experimental observable, such as measured ionization energies.[59]

Additionally, this can also be achieved through quantum mechanical techniques. Quantum software can be used to generate a target output, such as an electrostatic potential surface, and then a fitting procedure is used to assign and optimise assigned point charges to the system in an attempt to replicate the specified target. The difficulty in this approach is that there are various quantum softwares which can be used and also many fitting procedures that are available, depending on the output desired to be fit against.

This is just a very general description of point charge assignment and the author would like to recommend the reading of works by Nazarian et al.[60] for a short introduction into the various available methods.

### 2.1.6 *GCMC Procedure*

In Figure 6, the full GCMC procedure used in this thesis can be seen. Initially, the MOF structure is provided, with the assumption that the MOF remains rigid throughout the simulations. The necessary pmaps and emaps are then generated on this structure. Once the GCMC simulation begins, a certain percentage of the initial simulation steps (move attempts) is isolated as the system attempts to reach equilibrium at the specified pressure. After the equilibration stage is complete, the system begins recording the configuration information within the unit cell for conversion to adsorbed amount later in the procedure, this is known as the sampling stage.

Once the GCMC simulation is completed, the sampling configuration information must be transformed into relevant results, during the post GCMC conversion stage. Firstly the number of molecules in a unit cell can be used to determined the mmol/g adsorbed. The number of adsorbate molecules can be converted to mmol using Avogadro's constant, while the unit cell can be represented by mass using the density of the MOF. However, this is the absolute amount adsorbed, whereas in experiment it is the excess adsorbed that is measured. Excess adsorbed is the amount of adsorbate present minus the amount of adsorbate that would be present, at the same conditions, in the absence of the adsorbent. Therefore the absolute adsorbed values were converted to excess using the Myers and Monson method[61], see Equation 18.

$$\eta_{\text{Excess}} = \eta_{\text{Absolute}} - V_p . \rho_v \tag{18}$$

where

- $\eta$ Adsorbed amount
- $V_p$ MOF pore volume
- $\rho_v$ Bulk gas density

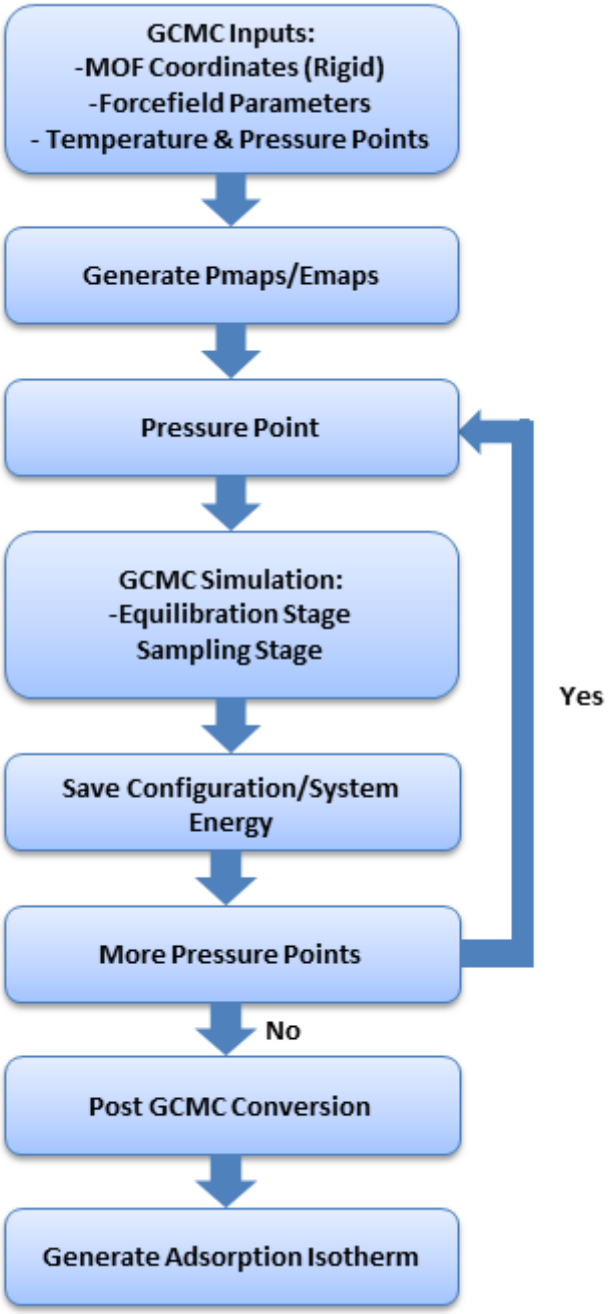


Figure 6: Representation of the GCMC procedure.

## 2.2 QUANTUM THEORY

In the quantum theory section, the main focus will be a subsection of this field known as Density Functional Theory (DFT). DFT is an approach used to determine the energy of a given system of particles through solving the Schrödinger equation. This section will look into the major assumptions behind this method as well as some of the key parameters utilised within the code.

### 2.2.1 *Concept*

In the late 19th century and early 20th century there were a number of discoveries that led to how the atom is thought of today. The culminations of experimental evidence suggested that the atom is made up of negatively charged electrons and a positive nucleus[62], raising the question why did they not collapse together due to attraction. Bohr proposed in 1913 that classical physics did not govern the behavior of atoms but that a new set of laws, now known as quantum mechanics, did. This lead to Schrödinger's equation which aims to describe the time evolution of an atomistic system due to these quantum effects[62]. It can describe the allowed energy levels of a quantum system through wavefunctions, by assuming that particles can be thought of as wave-like in nature. These wavefunctions can be represented by vectors, and will contain all the information regarding a particle's state within a system (e.g positions and velocities).

The time-independent many-body Schrödinger's equation can be seen below for an isolated system and must be solved to determine the ground state (lowest energy) of the system[63][64][62]:

$$\hat{H}\Psi\Big(\underbrace{\{r_i\}}_{\text{Electrons}}\ \underbrace{\{R_I\}}_{\text{Nuclei}}\Big) = E\Psi\Big(\underbrace{\{r_i\}}_{\text{Electrons}}\ \underbrace{\{R_I\}}_{\text{Nuclei}}\Big) \tag{19}$$

where

| | |
|---|---|
| $\hat{H}$ | Hamiltonian Operator |
| $\Psi$ | Wavefunction, describing quantum state of particles (Eigenstate) |
| $r/R$ | Position Vectors |
| $E$ | Eigenvalue (Proportionality Constant) |

In a quantum system, for every observable (e.g energy) there is a corresponding linear operator. The operator maps one quantum state to another state:

$$\underbrace{\hat{A}}_{\text{Operator}} \quad \underbrace{\Psi}_{\text{Orginal State}} = \underbrace{\Phi}_{\textbf{New State}} \tag{20}$$

However, when the operator maps from one state to the exact same state, a scalar factor is required:

$$\hat{A}\Psi = \underbrace{A_k}_{\text{Scalar Factor}} \Psi \tag{21}$$

This scalar factor is known as an eigenvalue, and is equal to the value of the observable operator type at that quantum state. Therefore in Equation 19, if the Hamiltonian operator is for energy states, then the eigenvalue will be the system energy for that wavefunction's quantum state.

The Schrödinger's equation must be solved for each particle in the system, this means that for a 3D system of, for example, 4 nuclei and 20 electrons this becomes a 72 dimensional problem (3 coordinates for each particle). This situation can be improved by applying the Born-Oppenheimer approximation, which assumes that the wavefunctions of the nuclei and of the electrons can be decoupled. This is because the nuclei are much heavier and therefore slower than the electrons, therefore while the electrons are finding their ground state the nuclei are essentially stationary. This means that the Coulomb potential associated with the nuclei can be treated as a static external potential ($V_{ext}$). The wavefunctions found in the Schrödinger's equation can therefore be simplified in Equation 22 enabling electron wavefunction to be solved separately:

$$\Psi\big(\{r_i\}\{R_I\}\big) = \Psi_{Electrons}\{r_i\} \cdot \Psi_{Nuclei}\{R_I\} \tag{22}$$

The form of the energy Hamiltonian operator for a many-body system with fixed nuclei then takes the form [64][65]:

$$137\hat{H} = \underbrace{-\frac{h^2}{2M_e} \cdot \sum_i \nabla_i^2}_{\text{Kinetic Energy}} + \underbrace{\sum_i V_{ext}(r_i)}_{\text{Coulomb Electron-Nuclei}} + \underbrace{\frac{1}{2}\sum_{i=1}\sum_{j>1}\frac{e^2}{|r_i - r_j|}}_{\text{Coulomb Electron-Electron}} \tag{23}$$

where

| | |
|---|---|
| $h^2$ | Reduced Planck's constant |
| $M_e$ | Reduced Mass of an electron |
| $\nabla$ | Gradient Vector operator |
| $V$ | potential of external field acting on particle |
| $e$ | Charge |
| $r$ | particle position |

This use of the Born-Oppenheimer approximation does simplify the Schrödinger's equation. However, for large systems it still leaves solving Schrödinger's equation near impossibly demanding in terms of computing power, for anything other than hydrogen-like systems. In the previous example, with 4 nuclei and 20 electrons, using this approximation only reduces the dimensional problem from 72 to 60. It is at this stage that 'Density Functional Theory' (DFT) can offer a solution.

Density Functional Theory relies on two fundamental assumptions (first and second Hohenberg-Kohn theorems, respectively)[65]. These assumptions are related to a new variable known as electron density, which can be thought of as an expectation factor of the number of electrons within a given volume:

1. The ground state energy of a many-electron system depends only on a unique functional of the electronic density (n(r)).

$$E = E(n(r)) \tag{24}$$

2. The correct ground state electron density is the one that minimises the energy of the electronic density functional.

$$E(n(r)) > E_{min}(n_{min}(r)) \tag{25}$$

The electron density can be determined in terms of the wavefunctions, as shown in Equation 26. If the energy of the system is expressed in terms of the electron density this reduces the dimensional problem from depending on 3N to just 3 spacial dimensions:

$$n(r) = \psi^*(r_1, r_2, r_3, r_n)\psi(r_1, r_2, r_3, r_n) \tag{26}$$

This problem can be further simplified if the electrons are though of as a point charge interacting with a field of electrons. Therefore, rather than solving all the electrons simultaneously, each electron can be solved individually[62]:

$$\psi(r_1, r_2, r_3, r_n) = \psi(r_1) \cdot \psi_2(r_2) \cdot \psi_3(r_3) \dots \psi_n(r_n) \tag{27}$$

$$\implies n(r) = 2\sum_i \psi_i^*(r)\psi_i(r) \tag{28}$$

Finally the energy (E) of the system can be expressed in terms of electron density[66]:

$$E_{system} = E_{known} + E_{unknown} \tag{29}$$

$$\begin{aligned} E_{known} = & \underbrace{-\frac{h}{M_e} \cdot \sum_i \int \psi_i^* \nabla^2 * \psi_i \, d^3r}_{\text{Kinetic Energy}} + \underbrace{\int V_{ext}(r) n(r) d^3r}_{\text{Coulomb Electron-Nuclei}} \\ & \underbrace{+ \frac{e^2}{2} \int\int \frac{n(r)n(r')}{r - r'} d^3r \cdot d^3r'}_{\text{Coulomb Electron-Electron}} \end{aligned} \tag{30}$$

In equation 29, the unknown term is correcting for the electron exchange and correlation energy and relates to the quantum electron interaction. This arises as the DFT calculation treats the electrons as interacting with an electron density field rather than specific electrons. This exchange and correlation energy tries therefore to account for effects such as how the movement of an electron would affect surrounding electrons and vice versa.[63] The exact form of the exchange correlation functional is unknown, however, and therefore is approximated based on the electron density.

### 2.2.2 *Exchange Correlation Functionals*

The simplest form of the exchange correlation functional is the 'Local Density Approximation' (LDA). This assumes that an inhomogeneous electron system is locally homogeneous. It therefore calculates the exchange correlation energy by integrating the exchange correlation energy density over the volume of each specific point, assuming a homogeneous electron gas with the exact same electron density (local constant density)[65][62]:

$$E_{xc}^{LDA}(n) = \int d^3r \cdot n(r) \cdot \epsilon_{xc}^{homo}(n(r)) \tag{31}$$

where

$E_{xc}$ Exchange Correlation Energy

$n(r)$ Electron Density

$\epsilon_{xc}$ Exchange Correlation Energy density (homogeneous gas)

This could be quite a good approximation for treating perfect bulk metal systems but is less effective for treating heterogeneous molecular systems. Therefore, the LDA functional was further developed into the Generalized Gradient Approximation (GGA) functional. This exchange correlation functional corrects the LDA functional with a term accounting for electron density's gradient, as shown in Equation 32. This can improve exchange correlation energies for systems in which the electron density rapidly fluctuates.[63] It can however lead also to worse DFT results when the gradients become so large that the expansion breaks down.[65]

$$E_{xc}^{GGA}(n) = \int d^3r \cdot n(r) \cdot \epsilon_{xc}^{homo}(n(r), \nabla n(r)) \tag{32}$$

where

$\nabla$ Gradient of Electron density

There are many other forms of improved exchange correlation functionals however, such as:

1. Meta-GGA functionals, which correct the GGA functional with a term accounting for kinetic energy density.[63]

2. Hybrid functionals, which include a percentage of an exact term to account for exchange effects.[63]

The use of more complex exchange correlation functionals is by no means a guarantee of better DFT results, as illustrated by GGA functionals. Indeed, often in these complex functionals more fitting parameters and empirical parameters are required, therefore they may work very well for systems similar to the systems

being parameterised against but can lack transferability. As these functionals are approximations, choosing the best exchange correlation functional for the system being investigated is of the utmost importance. Therefore substantial literature research should be conducted for each system to determine the most suitable exchange correlation functional.

### 2.2.3 *Kohn-Sham Scheme*

The previous section has shown the need for electron density but has not delved into how this value is determined. This approach relies on solving a set of single electron wave functions using the Kohn-Sham scheme, see Equation 33.[66][67] This is based of the one electron Schrödinger's equation but for a non interacting system, assuming it will still have the same electron density as that of an interacting system.

$$\Big[\underbrace{-\frac{\hbar}{2M_e}\cdot\nabla^2}_{\text{Kinetic Energy}} + \underbrace{V(r)}_{\text{Electron-Nuclei}} + \underbrace{V_H(r)}_{\text{Electron-Electron}} + \underbrace{V_{xc}(r)}_{\text{Exchange-Correlation}}\Big]\cdot\psi_i(r) = \epsilon_i(r)\cdot\psi i(r) \tag{33}$$

where

$V_H$ is the Electron-Electron Coulombic interaction (Hartree Energy)

The ground state electron density can then be determined using the Kohn-Sham scheme through a self-consistency loop (Figure 7).

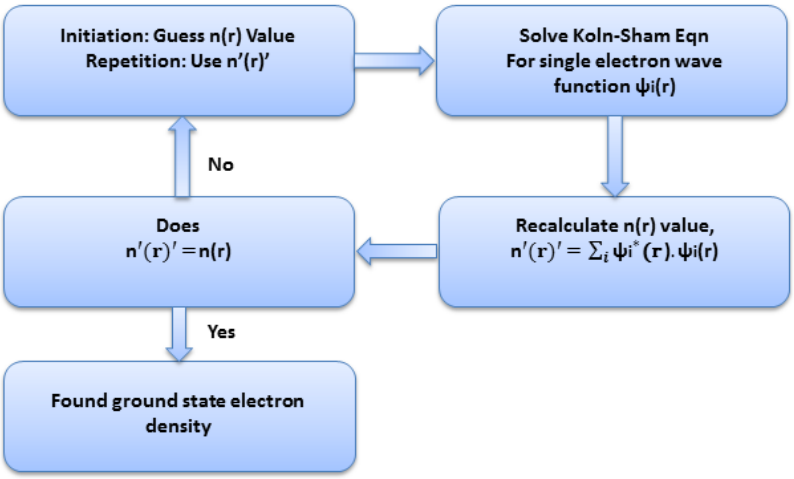


Figure 7: Representation of the Kohn-Sham scheme. The starting point of the scheme being the initial guess of n(r).

### 2.2.4 *Cluster vs Periodic*

The DFT calculations can be carried out on both cluster or periodic systems. Cluster calculations do not use periodic boundary conditions and therefore they can be very useful for studying a molecule in isolation. Furthermore, they can also be used to study local interactions. For example, if an adsorbate's interaction with a region of an adsorbent is short range, the binding mechanism could be studied by running a calculation on just that local cluster of the adsorbent. This can vastly save on computational cost, due to being able to calculate across a small system rather than the full adsorbent structure. The drawback of this technique however is that the user loses information about the long range effects of the rest of the system. This may become especially important when studying long range intermolecular interactions, such as electrostatics.

Periodic DFT calculations do apply periodic boundary conditions and therefore the unit cells used in the calculation are generally much larger. For crystals the full

repeating unit of that system much be used, to maintain the proper structure of the crystal. As would be expected, this does increase computational cost, but has the benefit of capturing the entire system accurately. This can be especially advantageous for describing the spins of metals, as well as capturing the aforementioned long range interactions.

### 2.2.5 *Basis Sets*

The wavefunctions used within DFT hold the key information about each particle within the system. These continuous functions are described in DFT by mathematical 'basis sets', which are normally a finite number of basis functions describing a molecular orbital through linear combinations of individual atomic orbitals.[68] This section will focus on plane wave and Gaussian basis sets due to their prevalence in DFT simulations.[69]

Gaussian basis sets are made up of primitive Gaussian functions, also known as Gaussian Type Orbitals (GTO), which are centred on the relevant atom's nucleus position.[70] An example of a simple s-type (Spherical) form of these functions can be seen in Equation 34. A combination of these functions can better capture the physical nature of an atomic orbital and therefore the Gaussian basis set will take the form in Equation 35. Finally, multiple Gaussian basis sets can be combined to describe just one atomic orbital, leading to double-zeta (two basis sets describing one atomic orbital) and triple-zeta (three basis sets describing one atomic orbital) basis sets.[62]

$$g_r = e^{-\zeta_\nu (x^2+y^2+z^2)} \tag{34}$$

$$\varphi_r = \sum_{\nu=1}^{N_\infty} c_\nu \cdot g_\nu(r) \tag{35}$$

where

$g_r$ Gaussian basis function

$\zeta$ Controls width of orbital

$\varphi$ Gaussian basis set

$c$ Contraction coefficient (enables weighting of each basis function)

A major benefit of using Gaussian basis sets is that relatively small basis sets can describe a molecular orbital well.[62] However, these basis set types can suffer from 'Basis Set Superposition Error' (BSSE) when simulating two monomers together.[70] This occurs as two monomers approach, the monomers can utilise the basis functions from each other, artificially stabilising each other and helping to better describe their own molecular orbitals. This in itself would not be considered an error except it is done so inconsistently, leading to varying descriptions of the molecular orbitals depending on molecular distances. The effect on the energy of the system can be accounted for using the 'Counterpoise Correction' (CP)[71] technique in which the BSSE value can be predicted by putting monomer A in the presence of the basis sets of monomer B without the actual atoms present and vice versa, therefore the effect of the basis set stabilisation can be contrasted with that of the full monomer A - monomer B calculation, as shown in Equation 36.[71]

$$E_{AB}^{CP} = E_{AB}^{AB(basisSet)} - E_{A}^{AB(basisSet)} - E_{B}^{AB(basisSet)} \tag{36}$$

In the case of molecular systems described by periodically repeated unit cells, a very convenient approach to describe their molecular orbitals relies on the utilisation of plane waves. These plane waves basis sets are made up of non-local wave functions, and therefore are not restricted to an atomic site (as Gaussian basis sets are). The use of plane waves would normally require using an infinite basis set, however by assuming periodic boundary conditions Bloch's theorem suggests that the system can be solved by summing over the first Brillouin zone (unit cell within Fourier Space).[72] Fourier space is used as it commonly can solve calculations involving periodic systems more efficiently (see e.g Ewald Sums Section 2.1.3.2).

An additional requirement of this technique is to determine only the valence electrons using plane waves and capture the core electrons using a pseudopotential. The pseudopotential is a simple potential which loses the oscillatory potential behaviour of the inner core electrons, but after a certain cut-off replicates the potential of a full all-electron wavefunction. This is advantageous as the mathematical problem becomes easier to solve (less electrons) and the chemistry is not affected (bond breakage/formation involves valence electrons and consideration of only valence orbitals and some vicinal orbitals is enough). If plane waves were used to describe core electrons, the computational cost would be prohibitively high. Moreover, the resulting pseudopotential is normally found to be quite small suggesting they do not have a key role in the DFT calculations.[72] It is worth noting that these pesuopotenitals are sometimes applied to Gaussian basis sets, especially for heavier atoms, but are not an absolute necessity. These assumptions lead to the wavefunction of the valence electrons being determined through Equation 37.[72]

$$\psi_i = \sum_G c_k(G) \cdot e^{i(k+G)\cdot r} \tag{37}$$

where

| | |
|---|---|
| $\psi_i$ | Wavefunction |
| $k/G$ | Fourier (Reciprocal) Lattice Vector |
| $c$ | Contraction Coefficient (enables weighting of each basis function) |

The accuracy of the calculations employing plane waves basis sets is affected by the selection of the following additional parameters. The first is the number of k points used to sample the first Brillouin zone (k point sampling).[62] This must be sufficiently high to obtain the correct energy of the system, as such it is determined through convergence testing, increasing k until the energy of the system does not vary within a certain set tolerance. For large unit cell sizes, the number of required k points is expected to be relatively small; while the opposite is true for small real space unit cells. The second required input is the 'Energy Cut-off' which is a limit of the plane waves within Fourier space. This takes the form of a sphere cut-off for mathematical simplicity, and can be seen in Equation 38. It represents a lower limit of the kinetic energy for the plane waves[62], essentially limiting the

number of plane waves used within a basis set. This value is again found through convergence testing.

$$\frac{[K+G]^2}{2} < E_{Cut} \tag{38}$$

For each basis set type there are different advantages and drawbacks, a list of some of the more general attributes are provided below[62][69]:

Table 1: Advantages/Disadvantages of Gaussian and plane wave basis sets

| **Gaussian** | **Planewaves** |
|---|---|
| + Computationally efficient | + Uses fast Fourier transforms |
| + Good description using small basis sets | + Easily proceduralised convergence testing |
| + Can perform all-electron calculations (pseudopotential not essential) | + Unbiased by atom centering |
| +/- Atom centered | + No BSSE |
| - BSSE | +/- Implicitly periodic |
| - Systematic improvement is difficult | - Often requires pseudopotentials |
| | - High cut-off required for systems where the wave functions vary rapidly |

### 2.2.6 *Additional Notes*

This section has covered a brief discussion into the workings of DFT, for a more in-depth view however the author would like to recommend further reading from works such as by Martin[53] and Kohanoff.[62] Additionally, it should be noted that this is only one quantum mechanical technique for studying electronic structures, there are many others worth investigating such as coupled cluster[73], MP2[74] (based on Møller-Plesset perturbation theory) and Hartree-Fock.[74][75]

## 2.3 STRUCTURAL ANALYSIS SOFTWARE- POREBLAZER

As various MOFs will be studied in this work, it is important to understand the underlying MOF structures being simulated. The open source software Poreblazer[76] was therefore used as a structure analysis tool for all MOF structures. Among other metrics, Poreblazer calculates the framework density, pore volume, accessible surface area and geometric pore size distribution, enabling a better understanding of the number of cage types within each MOF.

It computes the density of the MOF by dividing the mass of the MOF, provided in a unit cell, by the unit cell volume. The accessible surface area is found by 'rolling' a probe nitrogen atom along the surface of the MOF, using a provided collision distance away from the MOF atoms. 'Rolling' is not strictly correct as the simulation is actually generated through a Monte Carlo procedure but provides a good visual approximation of the technique. The pore volume is estimated by probing the MOF unit cell with a spherical guest, helium, in the MOF; only accessible pores are included, which requires the probe to have a path from one side of the unit cell to the opposite side without overlapping with framework atoms. Finally for the pore limiting diameter and percolation dimensions, the largest cluster of atoms are found within the MOF's unit cell. The pore limiting diameter is then calculated based on any path that permits a guest molecule to diffuse through the structure. The percolation in a dimension is determined based on the length of the largest cluster in the MOF. If the cluster's length is longer than or equal to the unit cell length, in the relevant dimension, it is then consider percolated for that dimension.

# Part III

# RESULTS CHAPTERS

# 3

# OLEFIN ADSORPTION IN CUS-CONTAINING MOFS

## 3.1 INTRODUCTION

As touched upon in Chapter 1, Metal-Organic Frameworks (MOFs) are an exciting new class of materials with many potential applications within industry. The focus of this chapter will be on using these materials for adsorption separation processes to potentially replace some of the highly energy-intensive distillation processes currently used within industry. Olefin/paraffin separations are currently among the most energy-intensive industrial processes run on a large scale[77], with production of plastics, such as polyethylene and polypropylene, demanding large quantities of both ethylene and propylene. The separations of ethane/ethylene and propane/propylene account for 0.3% of the world's annual energy consumption[20]. However, the replacement of conventional distillation with adsorption processes relies on an effective choice of adsorbent materials.

Recent works have aimed to use large-scale computational screening to identify promising MOFs for adsorption-based applications. In the work by Wilmer et al.,[6] a building-block method based on existing MOF structures was utilised to build 130,000 MOFs structures, most of them hypothetical. The authors then went on to computationally analyse physical characteristics of the MOFs as well as methane uptake capacities, which were adequately confirmed through experiment for some of the highest-performing existing MOFs. The success of computational screening studies like the example above is highly dependent on the model being used for adsorption predictions.[35][78] When the model fails to describe the correct adsorption mechanism, the results can be disastrous. An example of this was highlighted in work by Keskin et al.[78], which investigated a model for hydrogen adsorption in IRMOF-1 previously proposed by Yang et al.[79] The model had been fitted against experimental data up to 1 bar and reproduced the experimen-

tal isotherm well within this region. However, Yang et al.[79] went on to use the model to predict adsorption up to 100 bar; Keskin et al.[78] later compared this to their experimental values and observed that the simulation uptake of hydrogen was over double the experimental value. The need for robust models is therefore paramount for obtaining reliable results in molecular simulation, even when considering seemingly simple adsorbates such as hydrogen.

MOFs containing Coordinatively Unsaturated Sites (CUS), also known as Open Metal Sites (OMS), provide a unique simulation challenge in creating a model which can accurately describe the coordination bond that occurs with particular adsorbates. There are various MOFs that develop unsaturated metal centres upon the activation step prior to adsorption[80]. This occurs when the MOF's metal sites are not fully coordinated to organic linkers but rather to a guest molecule, for instance the solvent used in synthesis; upon removal of this molecule the metal is left with a free unsaturated site. These sites have demonstrated selective adsorption for many practical applications, strongly adsorbing gases such as $CO_2$[81], $C_2H_4$[17] and $H_2$[82]. This selectivity feature is promising in the aforementioned case of olefin/paraffin separations, which are generally achieved through costly cryogenic distillation, and for which these CUS-containing MOFs have the potential to be attractive materials for gas separation through alternative techniques such as Pressure Swing Adsorption (PSA)[83]. In the case of olefins, the double bond of the hydrocarbon can strongly coordinate with the metal centre of the MOF as explained by the Dewar-Chatt-Duncanson model.[84][85] As discussed by Nechaev et al[19], this occurs through an electron donation from the olefin's $\pi$-orbital to the vacant orbital of the metal centre, with back donation occurring from the metal's d-orbital to the antibonding $\pi$-orbital of the adsorbate.[86–88] The presence of these CUS introduces additional complexity in simulations. Standard forcefields were not originally designed to account for these complex orbital interactions[35] but rather deal solely with van der Waals forces. In the case of some highly polar adsorbates, such as water, the inclusion of Coulomb electrostatics within these standard forcefields may lead to relatively good agreement between simulation and experiment[89], however this is highly dependent on the selection of point charges. For non-polar adsorbates such as ethylene, the role of electrostatics has been ob-

served to be insignificant and cannot account for the increased adsorption at the CUS[18]. This would suggest that the better performance of standard models for polar adsorbates is caused by electrostatics dominating the adsorption mechanism and not by correctly capturing this orbital interaction.[90] Therefore a fully transferable model is still required to treat CUS interactions consistently.

A number of approaches have been proposed to address this failing, generally achieved through either re-parameterisation of the existing forcefields[86], accounting for polarization effects in the case of certain adsorbates[91] and/or through coupling of Grand-Canonical Monte Carlo (GCMC) simulations with quantum mechanical calculations.[1, 57, 92]

The work by Lamia et al.[86] focused on the prior method of refitting the LJ parameters, based on a single experimental isotherm point, in this case for propylene adsorbing in HKUST-1. Lamia et al. observed improvement in adsorption isotherm agreement by just refitting the LJ well-depth parameter of the Cu-$CH_2$ interaction. However, later work by Jorge et al. illustrated that this method did not capture the correct adsorption mechanism and the short range nature of the orbital interaction[87]. In spite of this, this method is still being utilised, most recently in a paper by Luna-Triguero et al.[93] which looked at ethylene/ethane competitive binary simulations for MOFs containing CUS (this will be investigated further in Chapter 4).

Becker et al.[91] used explicit calculation of polarization effects to improve adsorption isotherm agreement with experiment for $CO_2$ in M-MOF-74, again for various different metal complexes. The isotherm agreement with experiment is good, especially considering that the polarization parameters were grouped from two literature sources fitted against experimental data, with the intention in the future to derive these parameters based on quantum mechanical calculations. The implementation of this method, however, required a number of scaling terms, simplification of polarization calculations to improve computation efficiency and removal of implicit polarization effects already accounted for within the standard forcefields used. Furthermore, agreement with experiment for methane adsorption

in M-MOF-74 was poor, raising questions on the transferability of this approach for different gases. The work by Pham et al.[46] has also illustrated the improvement in $CO_2$ molecular simulations in MOFs when implementing explicit polarization effects. Furthermore, earlier work by Forrest et al[94], and later related work by Franz et al.[95], showed that this method markedly improves agreement for hydrogen adsorption within CUS-containing MOFs. However, due to the additional computational costs and questions regarding whether this approach will work equally well on less polarizable hydrocarbon adsorbates, this method will not be pursued within this thesis.

The idea of coupling quantum-mechanical calculations with GCMC more directly has led to a successful description of both adsorption isotherms and mechanism through a variety of approaches. These methods normally fall into one of three categories: 1) using DFT energies directly in GCMC simulations; 2) refitting the entire adsorbate-MOF interactions based on DFT energy profiles; 3) refitting only the adsorbate-CUS interaction, again based on DFT energy profiles.

Chen et al. [92] directly utilised DFT calculations with a pairwise correction term (DFT/CC)[96] to obtain full energy grids to account for the solid-fluid interactions between methane and HKUST-1 in GCMC simulations, i.e they generated a PMAP (see Chapter 2) directly from DFT calculations. This has the advantage of not having to fit the energy profiles to a classical functional, however requires extensive computing power to generate the DFT potential energy map[35]. Also, it is only currently applicable to spherical adsorbates, which limits it potential transferability to other systems.

Dzubak et al.[57] used DFT calculations to successfully sample $CO_2$ adsorption in both Mg-MOF-74 and MOF-5 (only the former contains CUS). The DFT interaction energy profiles thus created were used to fit all interaction parameters using a modified Coulomb-Buckingham potential. The resulting GCMC simulations obtained good agreement with experimental isotherms. The transferability of this model was also tested by simulating adsorption of $CO_2$ in Zn-MOF-74. Interestingly, only the metal interaction had to be re-parameterised in relation to

Mg-MOF-74 to obtain good agreement with experiment. As highlighted by Fischer et al.[35], this transferability suggests that the CUS orbital interaction could potentially be treated independently from the other interactions. It is important to note, however, that the DFT fitting approach of Dzubak el al. led to significantly different parameters for atoms in similar chemical environments (e.g aromatic carbons) in MOF-74 and MOF-5. This raises questions about whether this DFT approach can be used as a replacement for standard atomic forcefields, as a balance must be struck between accuracy and transferability.

Recent work by Borycz et al[97] utilised a combined approach of LJ refitting/DFT implementation for $CO_2$ adsorption in M-IRMOF-10, for various different metal complexes. This approach refitted the LJ parameters between the oxygen atom of $CO_2$ with a metal center based on DFT interaction energy profiles. This has the advantage of not relying on experimental isotherms which can vary considerably depending on the MOF sample used. It does however require including a short range CUS interaction to the LJ fit and therefore maintaining the correct full profile could be potentially difficult for particularly deep attractive wells. It should be noted that the same group has in earlier work used a slightly more complex Buckingham potential to account for this CUS interaction, in the case of $CO_2$ adsorption in Fe-MOF-74.[98]

Koh et al.[99] also used DFT calculations, with vdW-DF2 exchange correlation functionals, to predict methane behaviour at the CUS of HKUST-1, but fit the energy profile to a Morse functional, relative to the $CH_4$-Cu distance. The other $CH_4$-framework atoms interaction were described using classical forcefields. This led to better agreement with experiment, especially in the high pressure region. However, as the full interaction energy (i.e including van der Waals) was captured in this profile, CUS parameters would be required for every different adsorbate being simulated. Furthermore, when testing transferability of these CUS parameters to other similar Cu-paddlewheel MOFs, agreement with experiment diverged slightly.

Mercado et al.[100] proposed an innovative method for capturing $CO_2$ adsorption in CUS (as well as $CH_4$ and $H_2O$), again for the M-MOF-74 class. DFT calculations were used to obtain the energy profile for $CO_2$ with the CUS, but only the repulsive forcefield parameters were refit to improve consistency with DFT calculations. This also led to improved adsorption agreement with experiment. The fitting procedure however was nontransferable to certain MOF types, which could cause issues if wanting to apply this approach to large-scale screening simulations. Additionally, fitting to DFT profiles required an iterative self-consistent approach which resulted in some large deviations between forcefield and DFT energies, especially in the case of methane fitting.

This chapter will present work that expands upon the method of Fischer et al.[1], which also utilises functionalisation of DFT energy profiles. Fischer et al[1] used DFT to obtain an interaction energy profile between ethylene molecules and HKUST-1 Cu atoms. The major difference of this approach, however, is that the CUS contribution is isolated rather than left grouped with the van der Waals contribution, as in all the approaches discussed above. The isolation is achieved by subtracting the contribution of other energy terms determined using classical forcefields from the DFT energy profiles. This approach seeks to capitalise on the transferability demonstrated by Dzubak et al.[57] between Mg-MOF-74 and Zn-MOF-74, which implied that the CUS interaction may be treated independently of other forces. The GCMC simulations then used classical forcefields to describe the van der Waals component of the intermolecular forces between the MOF and the adsorbate, while using a specific functional form to capture the CUS interaction alone. The resulting adsorption isotherms showed very good agreement between simulation and experiment across a variety of temperatures. A major strength of this approach is that the model is able to respond to improvements in the description of either CUS or van der Waals forces independently. Furthermore, as the non-orbital interaction will be captured through classical simulation methods, only one DFT interaction energy profile is required relative to the metal centre, describing the CUS contribution. The main advantage, however, is the prospect for the model to be transferable. For example, if the strength of the CUS contribution for the carbon-carbon $\pi$ bond is consistent across olefins, this enables the same

forcefield parameters to be used for various adsorbates. A later paper by Jorge et al.[18] in fact demonstrated that the same CUS parameters were transferable between ethylene and propylene without the need for any parameter adjustments.

Recent work by Heinen et al.[101] utilised a similar approach to that of Fischer et al.[1], isolating the CUS interaction from a DFT profile and treating it independently within the GCMC simulation. The key difference between the two methods was in how the CUS contribution was isolated. The group used the Amsterdam Density Functional (ADF)[102][103] package's energy decomposition scheme to isolate the CUS interaction, rather than using the classical forcefields approach discussed above. This led to a much lower orbital interaction energy at the minimum for the Heinen et al. work, which had to be compensated later through altering copper and oxygen classical forcefield values used to describe the van der Waals interactions. Transferability was not tested in the work of Heinen et al., but one can expect that this changing of classical forcefields would lead to difficulty in transferability, as such this approach was not pursued within this work.

Finally, there was a recent study by Kulkarni and Sholl[104], which used a DFT profile and isolated the ethylene interaction with the CUS of HKUST-1, by removing the interaction contribution of surrounding atoms. This was then fit to a pairwise Morse potential for the Cu-$CH_2$ interaction. This work shared a similar goal to that of the present chapter, of testing a DFT-based CUS functional approach for transferability to different copper paddlewheel MOFs. The Kulkarni method, however, has a number of important technical differences, which have lead to differing agreement with experiment. Furthermore, the focus of Kulkarni and Sholl[104] was on predictive simulation of MOF performance, whereas this chapter will focus on model validation. As such, a comparison of the differences in technical approaches will be discussed within the latter part of this chapter's Methodology section, to enable the reader to have a better appreciation of the background theory of this method.

Overall, this chapter will demonstrate that the proposed CUS model for ethylene is transferable not only to other adsorbates but also to other adsorbent materials

with unsaturated Cu sites. All MOFs studied here contain the copper paddlewheel motif found in HKUST-1 and used in our parameter fitting, but one of the MOFs introduces a different copper building unit. Furthermore, some technical improvements are reported in both the DFT and GCMC procedure. The ultimate aim is to develop a transferable method that correctly captures the CUS behaviour in a range of MOFs to enable effective computational screening of CUS-containing MOFs for challenging gas separations. Indeed, we show that our approach for describing the CUS interaction leads to very good agreement with experiment, and thus our forcefield can be used with confidence to make predictions of adsorption in this class of materials.

## 3.2 METHODOLOGY

This section will outline the procedure to model the interaction of ethylene with the HKUST-1 CUS, however for a more in-depth look into the earlier development of this model the reader is referred to previous papers.[1, 18, 58, 105] The procedure is comprised of 5 key stages:

1. Quantum-mechanical (QM) calculations to obtain the interaction profile between the adsorbate and the CUS.
2. Isolation of the CUS contribution in the DFT profile.
3. Fitting the resulting profile to a modified Morse functional.
4. Including the new CUS interaction site in GCMC simulation.
5. Validating GCMC adsorption isotherms against experiment.

The number of copper paddlewheel MOFs that the new model can be validated against is limited by the number of available experimental isotherms for ethylene adsorption. He et al.[37] published a number of new ethylene adsorption isotherms for six Cu-containing MOFs; HKUST-1, PCN-16, NOTT-101, MOF-505, UMCM-150 and UTSA-20. Therefore these MOF will be the focus of this transferability study. He et al.[37] also provide methane and ethane adsorption isotherms for these MOFs. As they are both saturated hydrocarbons, the CUS interaction will not play an important role in adsorption.[35, 77] Therefore comparison of simulations with experiment for these adsorbates can be used first to indicate whether the MOF structure and van der Waals interactions are being correctly described in GCMC simulations, before any discrepancies found within ethylene simulations can be attributed to the new CUS model. We have therefore carried out simulations of methane, ethane and ethylene at both 273 and 296 K on the six MOFs mentioned above. Initially, new CUS parameters for HKUST-1 were developed to improve upon those used in previous work[18], and as such the resulting simulated ethylene isotherms were compared to both experiment and simulations obtained using the previous CUS parameters. Furthermore, additional DFT energy profiles and CUS parameters were obtained for MOF-505 to confirm transferability of the

adsorption energies to different MOFs. New energy profiles and CUS parameters were also obtained for the different copper building unit present within the structure of UMCM-150 (see Results section).

### 3.2.1 *DFT calculations*

In this work the DFT calculations use the open source software CP2K[106, 107] with periodic boundary conditions, enabling the full MOF structure to be taken into account. CP2K uses a combination of basis sets from Gaussian-type orbitals and a plane-wave basis; for an explanation of these basis set types see Part 2.[106, 107] The exchange-correlation functional used was PBE[108], as this functional has been used successfully for this model in previous work.[1, 18] Additionally it has been shown to capture the correct binding distances for both hydrogen and ethyne on HKUST-1 CUS.[105, 109] PBE does however have limitations regarding treatment of dispersive interactions[110–112], which will be discussed and accounted for in the fitting procedure. The basis sets used for all atoms were double zeta plus polarization (DZVP) with PBE optimised Goedecker pseudopotentials[107, 113, 114]. The energy cut-off selected was 400 Ry, and convergence was checked by using higher values for selected cases, and the calculations used $\Gamma$ point sampling. Furthermore, spin polarization was accounted for in all DFT calculations. Initially, both the ethylene and the HKUST-1 structure were optimised independently and later used as reference energies to obtain the ethylene-MOF interaction energy from:

$$U_{Interaction}(r) = U_{complex}(r) - U_{HKUST\text{-}1}(r) - U_{ethylene}(r) \tag{39}$$

This differs from previous work[18], in which the original HKUST-1 CUS parameters were obtained using energy profiles from all-electron DFT cluster calculations ran with the DMol$^3$ code[115, 116] contained within the "Material Studio" package (see Chapter 2 for explanation of cluster calculations).[117] Small cluster models behave well in cases where the nature of the interaction is very localised but can

lead to inaccurate representations of molecular systems when long range effects are important[110]. As such, the decision was made to switch to periodic DFT calculations to remove this potential source of error (and in the process, validate the accuracy of previous cluster calculations). Furthermore and above all, using periodic DFT calculations improves consistency with later steps in the fitting procedure, which are also based on periodic boundary conditions (see Parameter Fitting).

The DFT optimisation protocol differed only slightly from the work of Jorge et al.[18] due to the introduction of periodic calculations; it should be noted, however, that both present and previous[18] DFT calculations use two adsorbing ethylene molecules on either side of a copper dimer to limit distortion of the copper building unit, as illustrated in Figure 8.

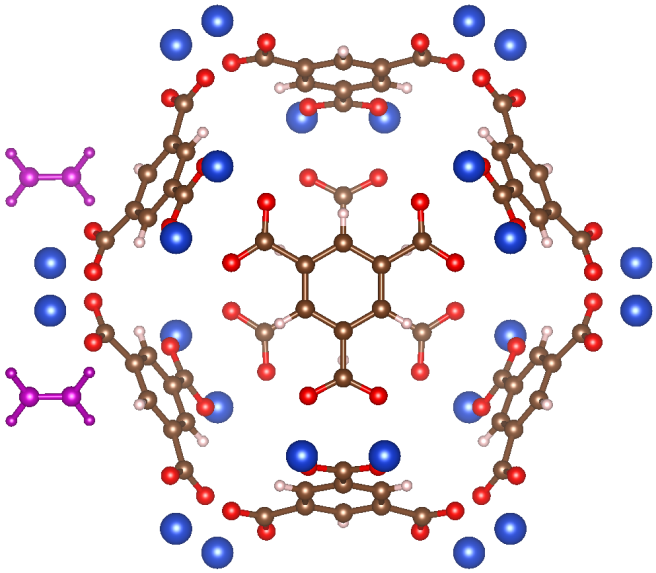

Figure 8: Illustration of two binding ethylene molecules (purple) in HKUST-1 primitive cell. Color code for atoms/molecules is: blue-copper, red-oxygen, brown-carbon, white-hydrogen and purple-ethylene.

Firstly, after the initial minimum energy geometry optimisation of the ethylene-MOF complex, the internal degrees of freedom of the adsorbate were kept entirely fixed while the adsorption energy profile along the Cu-Cu vector of the paddle-wheel was computed (see Figure 9). This was required as the adsorbate is now in a 3D cage and could move away from the relevant Cu-Cu vector at larger distances

from the metal, where the CUS interaction becomes weaker and van der Waals forces dominate. Conversely, as the DFT calculations were now periodic there was the opportunity to allow the entire framework to relax upon optimisation with ethylene; this was not possible in previous cluster calculations because it would lead to unphysical distortion of the MOF cluster. Table 2 compares the optimized energies and binding distances (Cu to the center of the ethylene double bond) obtained in a fully fixed HKUST-1 framework, a fully relaxed framework and a partially relaxed framework, in which only the Cu atoms were free to move. Using a fixed framework led to a slightly less favourable binding energy, and correspondingly larger binding distance, for ethylene, as observed previously.[1] However the difference in interaction energy between a partially restricted optimisation (Cu free to relax) and a non-restricted framework was not significant, and therefore the former approach was chosen to minimise computing time. Additionally, in Table 2 it can be seen that the difference in DFT interactions energies between cluster and periodic calculations is very slight, implying that either procedure would be suitable for obtaining energy profiles. It should be noted that the interaction energies shown in Table 2 do not properly account for dispersion interactions.

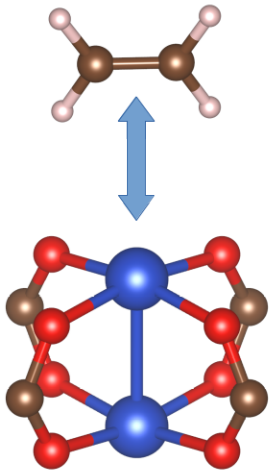

Figure 9: Illustration of Cu-Cu vector that ethylene molecules is moved upon within DFT calculations. Color code for atoms is: blue-copper, red-oxygen, brown-carbon, white-hydrogen.

The DFT obtained interaction energy profile for partially restricted optimisation of ethylene in HKUST-1 is shown in Figure 10, with respect to the distance from center of the ethylene molecule and the nearest copper site. The position of the ethylene molecules at the energy minimum, for all DFT optimisations, showed that the copper-copper vector was in line with the center of the ethylene molecule's double bond, as can be seen in Figure 9. This highlights the center of the ethylene double bond as the best site for the CUS interaction with the copper atoms, in the GCMC simulations.

Table 2: DFT calculations with different geometry constraints (*B.D - binding distance)

| DFT Calculation | Optimisation | Int. Energy (kJ/mol) | *B.D (Å) |
|---|---|---|---|
| Cluster[18] | Relaxed Copper | -23.3 | 2.60 |
| Periodic | Fixed Framework | -21.5 | 2.74 |
| Periodic | Relaxed Copper | -23.3 | 2.63 |
| Periodic | Relaxed Framework | -23.7 | 2.61 |

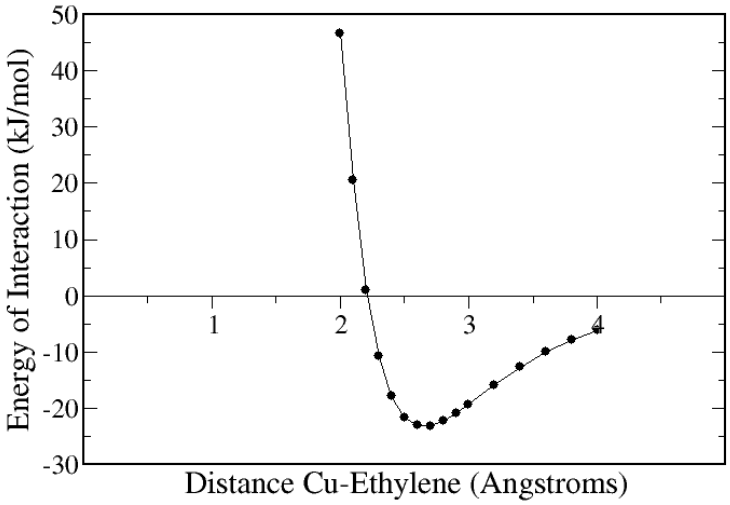


Figure 10: Illustration of interaction energy obtained for the DFT profile of ethylene in HKUST-1, using PBE.

### 3.2.2 *Parameter fitting*

Once the interaction energy profiles between the adsorbate and the metal site of a MOF were calculated using DFT, the CUS contribution must be isolated before it can be fit to a given functional form, and this requires assumptions about the DFT energies. The first assumption is that electrostatics do not play a significant role in ethylene adsorption on MOF frameworks. Jorge et al.[18] simulated adsorption isotherms for ethane and ethylene in HKUST-1 both explicitly including and ignoring electrostatic interactions. The difference between the isotherms was negligible, indicating that the above assumption is reasonable and the electrostatic contribution to the energy profile can be disregarded.

The second major assumption is that the PBE exchange-correlation functional does not capture any dispersive van der Waals interactions near the Cu site; PBE often predicts very low or negligible binding in van der Waals complexes[110–112], which suggests that this assumption is at least reasonable. This then implies that the energy of interaction obtained in DFT arises solely from the Cu-$\pi$ interaction and the repulsive contribution[1]:

$$U_{Cu-\pi}(r) = U_{DFT}(r) - U_{Rep}(r) - \underbrace{U_{Disp}(r) - U_{Electro}(r)}_{\text{Zero}} \tag{40}$$

To isolate the Cu-$\pi$ interaction, the repulsive contribution must thus be determined. This was achieved using in-house software to calculate the Lennard-Jones potential energy profile along the Cu-Cu vector in a fully periodic structure, based on the classical models that will be used later in GCMC simulations. The use of periodic GCMC simulations in this step is a primary reason to use periodic DFT calculations to obtain DFT energy profiles, for a more consistent isolation procedure. The Weeks-Chandler-Andersen (WCA) approximation[118, 119] was then applied to isolate the repulsive contribution in the LJ potential. This assumes that by truncating the LJ potential at the minimum energy value and then adding this

value to the remaining potential profile gives the repulsive energy, as shown in Figure 11.

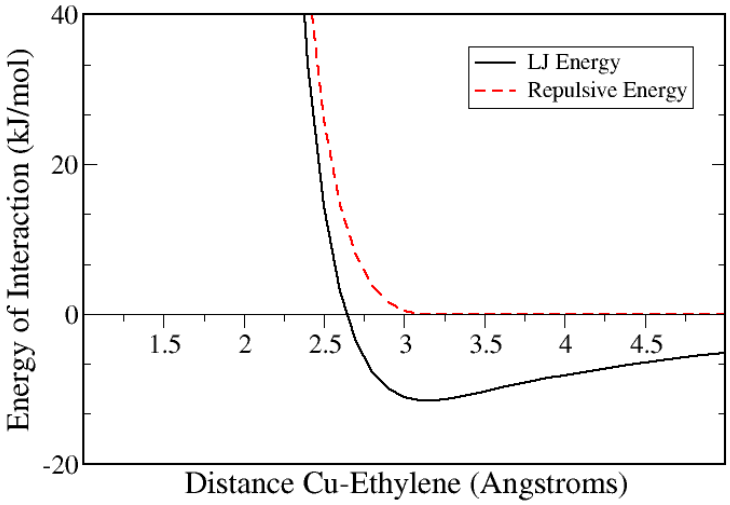


Figure 11: Illustration of the WCA approximation to estimate repulsive interactions.

The now isolated Cu-$\pi$ profile represents the attractive interaction energy between the olefin double bond and the copper atom due only to the CUS, and will need to be fit to a function for use in GCMC simulations as a single interaction site. The location of the CUS site was chosen to be at the center of the ethylene double bond; this was because it was found to be the closest point to the copper within the DFT calculations and also made sense physically as it is the double bond which donates the electron to the CUS (Figure 12).

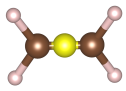

Figure 12: CUS site located on ethylene molecule, Color code for atoms is: brown-carbon, white-hydrogen and yellow-CUS site.

The CUS interaction site has the functional form of a 5-parameter modified Morse potential[1], shown in equation 41. This includes a power law term enabling the short range nature of the CUS interaction to be fully captured.

$$U_{function}(r) = D_o \cdot \left[ exp\left(\alpha\left(1 - \frac{r}{R_o}\right)\right) - 2 \cdot exp\left(\frac{\alpha}{2}\left(1 - \frac{r}{R_0}\right)\right)\right] - \left(\frac{A}{r}\right)^B \quad (41)$$

In this equation, $R_o$ corresponds to the distance of the minimum in the Morse potential, while $D_o$ represents the depth of this minimum, akin to the role of $\sigma$ and $\epsilon$, respectively, in the LJ potential. The $\alpha$ constant reflects the flexibility of the curve, while the final two parameters $A$ and $B$ are purely empirical terms.

In previous work[87] equation (3) was fitted to the energy profile over a range of binding distances between 2 and 5 Å, as shown in Figure 13.

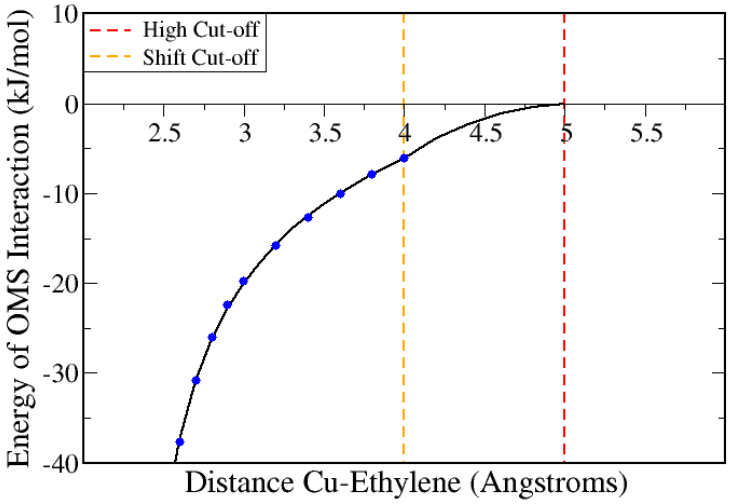


Figure 13: Previous work's cut-off scheme shown for the periodic DFT based CUS interaction, using the modified Morse potential. Black line- newly parameterised CUS interaction and Blue Circles- DFT Cu-$\pi$ binding energy.

A high cut-off at larger separation distances was then introduced into the GCMC simulations for this Cu-$\pi$ interaction to avoid an unrealistic enhancement of adsorption energies away from the Cu atom[18]. This would contradict the short-range and highly directional nature of the Cu-$\pi$ interaction, and may violate the

requirement that the unsaturated copper can only form a coordination bond with one adsorbate molecule at a time. This was complemented by a smooth shift cut-off region to avoid a discontinuity in the potential. As an adsorbate molecule's binding distance enters the shift cut-off region, its interaction energy will steadily tend towards zero as the binding distance approaches the high cut-off value. The final cut-off scheme has the following form:

$$U_{Cu-\pi}(r) = \begin{cases} U_{function}(r) & \text{Shiftcut} \geqslant r \\ U_{function}(r) \cdot \dfrac{(\text{Hicut} - r)}{(\text{Hicut} - \text{Shiftcut})} & \text{Shiftcut} < r < \text{Hicut} \\ 0 & r \geqslant \text{Hicut} \end{cases} \quad (42)$$

Previously, the high cut-off for this Cu-$\pi$ interaction was set at 5 Å with the shift cut-off set at 4 Å.[18] We have investigated the cut-off scheme in more depth, and although the previous scheme greatly improved upon the issue of unfeasible binding energies at large distances, it did not fully solve the problem. When the final configurations of the GCMC simulations were analysed, it could be observed that more than one ethylene molecule fell within the interaction sphere of each single copper site. This meant that the CUS was occasionally interacting with more than one adsorbate, which is unphysical, albeit much more weakly for further away molecules. It was therefore decided that the cut-off scheme must be optimised to remove the possibility of multiple CUS interactions per copper site, while not hampering single adsorbate CUS adsorption. This was tested by carrying out GCMC simulations on HKUST-1 pre-loaded with one fixed ethylene molecule adsorbed at each unsaturated Cu site, both with and without the CUS-specific interaction term. As the copper sites are pre-loaded, the CUS interaction should have no effect on adsorption, and thus the two isotherms should be identical. The resulting GCMC simulations including and excluding the CUS interaction were compared, using several cut-off schemes. In Figure 14, it can be seen that a shift cut-off of 4 Å and high cut-off of 5 Å is unsuitable, leading to slightly higher adsorption than the simulation excluding CUS specific interactions. This difference can thus be ascribed to an artificial enhancement of the CUS interaction energy away from the metal site.

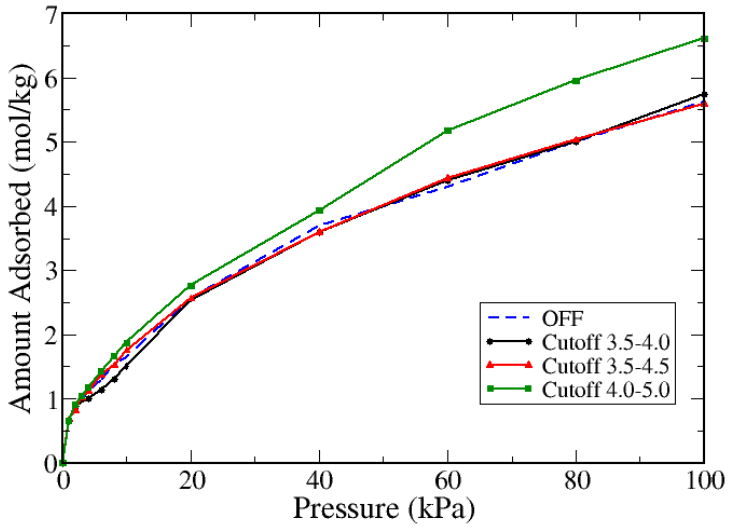


Figure 14: Simulated adsorption isotherms in pre-loaded HKUST-1 for ethylene. The solid lines show results of the periodic DFT model for various cut-off schemes identified in graph key, noted in the key by their shift cut-off and then their high cut-off (cutoff shift-high)OFF refers to a simulation without CUS interactions (dashed line).

This was later confirmed using visual software to test the number of adsorbate molecules less than 5 Å away from the copper. This was done by removing all but the copper and CUS sites from the GCMC configuration file and setting the bond length (i.e interaction distance) between the sites to 5 Å , shown in Figure 15.

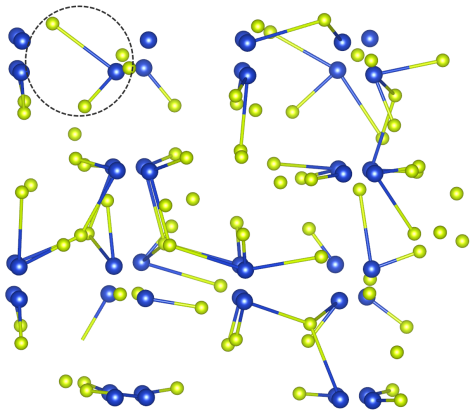

Figure 15: Snapshot of interaction distance between copper (blue) and CUS site (yellow) within a GCMC simulation. An example of a Cu atom binding to two ethylene molecules is highlighted.

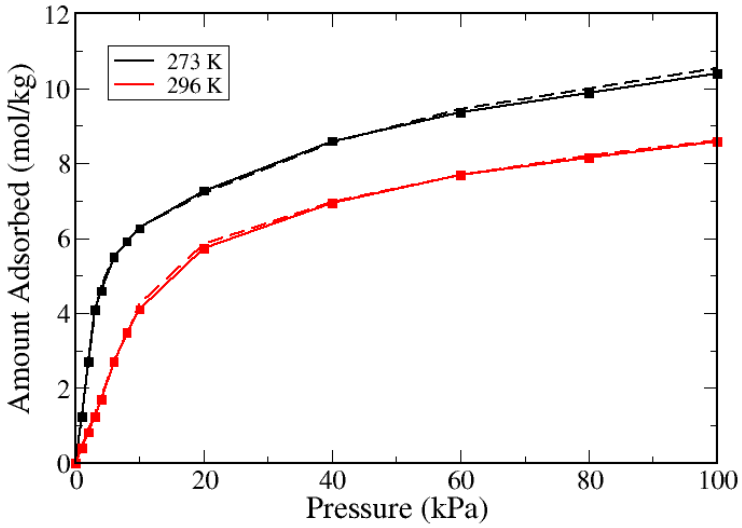


Figure 16: Simulated (lines) adsorption isotherms in HKUST-1 for ethylene. The solid line shows results of the periodic DFT model (Cut-off 3.5-4 Å) and the dashed line is for the periodic DFT model (Cut-off 3.5-4.5 Å). The solid line with square points shows the periodic DFT model (Cut-off 3.5-4 Å) with no low cut-off.

The remaining two cut-off schemes investigated would both be acceptable to meet the criteria above. However, two other factors must be considered when choosing the most suitable cut-off scheme. Firstly, smaller cages than those present in HKUST-1 may be located in other MOFs and therefore a smaller high cut-off would be preferable to avoid artifacts in future applications of the model. However, it must be ensured that the CUS interaction is not shortened too far as to impede adsorption in viable CUS adsorption sites. To test this, the smaller cut-off scheme with 3.5 Å shift cut-off and 4 Å high cut-off was compared against the higher cut-off scheme with 3.5 Å shift cut-off and 4.5 Å high cut-off. As shown in Figure 16, the difference in adsorption between the two cut-off schemes is negligible, indicating that the cut-off scheme with 3.5 Å shift cut-off and 4 Å high cut-off is sufficient to capture the CUS interaction without artificially strengthening sites away from the CUS, as such it will be used for all future GCMC simulations.

Due to this improved cut-off scheme, the parameter fitting procedure was only carried out between binding distances of 2 and 4 Å. Finally, a low cut-off for the

CUS interaction was also introduced to avoid mathematical artifacts in close vicinity to the open metal site. For example, in the case of HKUST-1 it was observed that a small number of configurations at binding distances between 1-1.4 Å occurred in which the negative CUS term was higher in magnitude than the positive repulsive energy from the LJ potential, which created an unrealistic adsorption site very close to the copper atom. This artifact was eliminated by shifting the CUS interaction energy to zero below a low-cut value of 1.8 Å. Although these changes to the cut-off scheme had a very small effect on the ethylene adsorption isotherms in HKUST-1 (Figure 16), there is no guarantee that the effect will not be important in other MOFs or with other adsorbates. As such, the low-cut has been implemented in the new cut-off scheme for these calculations and all future work, as although the effect of the low cut-off on the isotherm may be minor its description of the binding mechanism will be more physically reasonable.

It is worth mentioning at this stage that this parameter fitting procedure is quite different from the one proposed recently by Kulkarni and Sholl[104]. Those authors chose to fit their DFT energies to a pairwise Morse potential between the Cu atom and each of the $CH_2$ sites of ethylene, whereas in this work there is a new CUS-specific interaction site at the center of the double bond. Their original scheme led to artificially high interaction energies for configurations in which the olefin was highly tilted with respect to the Cu-Cu vector, which prompted the authors to introduce a three-body orientationally dependent term to their potential. Furthermore, because their CUS interactions are truncated only at 13 Å, it is possible that their model is artificially enhancing adsorption away from the Cu atom, (this point is returned to later in the chapter). On the contrary, the present fitting scheme ensures that the short-range and directional nature of the Cu-$\pi$ interaction is correctly captured.

### 3.2.3 *GCMC simulations*

All adsorption isotherms were obtained through GCMC simulations using the open source code Music.[120] The code was adapted to include the modified Morse potential function enabling CUS interactions to be introduced; the main addition to the Music code can be seen in Appendix A.1. An introduction into the basic concepts behind GCMC simulations can be found in Chapter 2. Before running full GCMC adsorption simulations, potential maps (PMAPs) that tabulate the interaction energy between a given adsorbate site and the MOF on a fine grid were produced (see Section 2.1.4.2). The grid spacing selected for these maps was 0.15 Å. For simulations of methane and ethane, cavity bias[52] based on the LJ potential maps was used for insertion and deletion trials (see Section 2.1.4.2). In the case of ethylene, however, insertion and deletion were done randomly (i.e. without bias). This is because two map types were present (CUS and LJ), and using a bias based on only one map type could possibly negatively deviate the simulations away from sites that would become favourable when accounting for both intermolecular forces. In the future, it would be desirable to further modify the simulation code to allow for biased insertions and deletions using a combination of PMAPs, which is not currently allowed within Music. In addition to insertion and deletion trials, molecules were allowed to rotate and translate (or only translate, in the case of methane), using optimized maximum displacements. All MC trials were equally weighted and occurred once per simulation step. A minimum of 100 000 000 steps were used, but this was increased to 500 000 000 for methane simulations to reduce statistical error due to the smaller amounts adsorbed. The first 50% of steps were ignored to ensure equilibration, and the remaining steps were split into 20 equal blocks for error analysis. Error bars were always smaller than the symbols used in the results section, and are therefore not shown. Pressure values were converted to fugacities for input into the simulation code using the Peng-Robinson equation of state[121].

#### 3.2.3.1 *LJ Forcefields*

The DREIDING forcefield[56] was used to describe most framework atoms as it has previously been successful in describing adsorption in MOFs.[122] The exception is the copper atom which is not present in DREIDING; as such the Universal forcefield (UFF)[55] was selected to describe repulsion and dispersion interactions with the metal. A recent MOF simulation study has shown that using either of these forcefields leads to little qualitative differences in adsorbed amounts, although slight quantitative differences can be found depending on the system being studied.[123] For the adsorbates, a united atom approach was used for each $CH_x$ group, with parameters taken from the TraPPE forcefield.[53, 54] Both the framework and the adsorbates were kept fully rigid during simulations. All cross-species LJ parameters were determined using the standard Lorentz-Berthelot combining rules, and an interaction cut-off distance of 13 Å was applied.

#### 3.2.3.2 *CUS Functional*

The values of the cut-off distances are provided in Table 3 for completeness, while Table 4 reports the CUS parameters found through fitting the DFT energy profiles obtained on three different MOFs to equation 41, as well as the corresponding parameters obtained in previous work[18].

Table 3: CUS interaction cut-off scheme

| | |
|---|---|
| Low Cut-off | 1.8 Å |
| Shift Cut-off | 3.5 Å |
| High Cut-off | 4.0 Å |

Table 4: CUS parameters obtained from DFT fitting to Equation 41

| MOF | Complex | Produced | $R_o$ (Å) | $D_o$ (kJ/mol) | $\alpha$ | A | B |
|---|---|---|---|---|---|---|---|
| HKUST-1 | Dimer | Jorge[18] | 3.1870 | 9.9600 | 7.9200 | 3.867 | 9.2400 |
| HKUST-1 | Dimer | This Work | 3.1030 | 10.6324 | 8.0945 | 3.825 | 9.2812 |
| MOF-505 | Dimer | This Work | 3.3484 | 9.8712 | 6.8640 | 4.007 | 8.5900 |
| UMCM-150 | Trimer | This Work | 4.3090 | 8.0858 | 5.9320 | 4.337 | 8.7583 |

### 3.2.4 *Structural analysis*

As various MOFs will be used to check the transferability of this CUS model, it is important to understand the cage structures within the MOF. The open source software Poreblazer[76] was therefore used as a structure analysis tool for all MOF structures studied in this work; a description of the sofware can be found in Section 2.3. Importantly, it provides an estimate of the pore limiting diameter for each MOF, which is the narrowest constriction found in any path that permits a guest molecule to diffuse through the MOF structure[76]. It thus provides some important insight into the pore network topology and may help identify existing diffusion limitations. However, the pore limiting diameter does not always correspond to the smallest window size in a given MOF - in cases where pores are isolated from the rest of the network by small windows, they will not be part of the diffusive path of the adsorbates. Analysis of the entire pore network connectivity is used to identify possible regions of the pore space that are inaccessible for adsorption. A full breakdown of the Poreblazer analysis on all of the studied MOFs is given in Table 5.

Table 5: Poreblazer[76] analysis for each MOF. ρ- density $V_p$- helium pore volume, S.A- accessible surface area, P.L.D- pore limiting diameter, Percolation- dimensions for percolation through the MOF system.

| MOF | ρ ($g/cm^3$) | $V_p$ ($cm^3/g$) | S.A ($m^2/g$) | P.L.D (Å) | Percolation |
|---|---|---|---|---|---|
| HKUST-1 | 0.879 | 0.853 | 1911 | 6.37 | 3D |
| PCN-16 | 0.722 | 1.092 | 2826 | 6.32 | 3D |
| NOTT-101 | 0.683 | 1.222 | 3087 | 5.60 | 3D |
| MOF-505 | 0.926 | 0.806 | 1923 | 4.53 | 3D |
| UMCM-150 | 0.635 | 1.259 | 3057 | 8.81 | 1D |
| UTSA-20 | 0.909 | 0.770 | 1589 | 8.80 | 1D |

### 3.2.5 *Experimental Isotherm Scaling*

It should be noted that all experimental isotherms were scaled up using the ratio between the theoretical pore volume($V_p$) of an ideal crystal and the experimental pore volume reported by He et al.[37], both determined from analysis of saturated nitrogen adsorption at 77 K. The scaling method is shown in Equation 43. This procedure takes into account, in an approximate way, for the observed reduced adsorption capacity in real MOF samples, due to potential imperfections such as collapsed pores, non-porous by-products, and solvent molecules trapped inside the pores of the MOF during synthesis[18]. This also enables experimental isotherms obtained from different quality samples to all be used in comparison with simulation, provided they are consistent with each other. This technique will be used for all experimental isotherms within this thesis, unless otherwise stated.

$$\eta_{\text{Scaled Experiment}} = \eta_{\text{Experiment}} \cdot \frac{V_{p(\text{Simulation})}}{V_{p(\text{Experiment})}} \tag{43}$$

## 3.3 RESULTS AND DISCUSSION

In this section, the results of transferring the CUS parameters obtained on HKUST-1 to various other Cu-based MOFs will be presented. In previous work, it has been demonstrated that this CUS approach is able to correctly describe the adsorption mechanism of olefins on HKUST-1[1], and that the parameters are transferable between different adsorbate molecules of the same type (e.g., ethylene to propylene) on that same MOF material[18]. Nevertheless, first a comparison will be carried out between simulated ethylene adsorption in HKUST-1 and the experimental data set of He et al.[37], which was not considered in previous work, and to validate the changes introduced in the DFT calculations (periodic instead of cluster) and fitting procedure (improved cut-off scheme). For that purpose, this section will compare isotherms obtained using the new approach to those using the original parameters of Jorge et al.[18] Subsequently, adsorption isotherms using parameters obtained from periodic DFT calculations on HKUST-1 will be calculated for the remaining MOFs — PCN-16, NOTT-101, MOF-505 (NOTT-100), UMCM-150 and UTSA-20 — and compared against experimental data[37].

### 3.3.1 *HKUST-1*

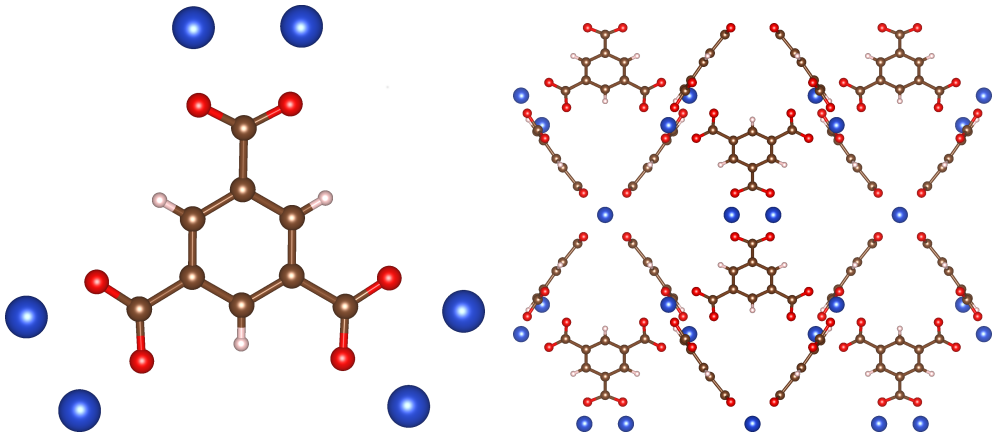

(a) Linker (b) Topology

Figure 17: Diagram showing the linker (a) and the unit cell topology (b) of HKUST-1. Color code for atoms is: blue-copper, red-oxygen, brown-carbon and white-hydrogen.

HKUST-1[10] is one of the most widely studied MOFs[124]. It has the composition $Cu_3(BTC)_2$ and is made up of two copper ions in a paddle wheel structure with BTC linkers, benzene-1,3,5-tricarboxylate [125]. In Figure 17, the overall structure is shown to be cubic with a *pto* topology[105], which arises from the tritopic linker. The Secondary Building Unit (SBU) is made up of the two copper atoms bridged by four carboxylate functionalities from the BTC linker [125]. $Cu_3(BTC)_2$ has three pore types, all roughly spherical, one small tetrahedral pore $\approx$ 5 Å and two larger octahedral pores of $\approx$ 11 Å and 12 Å. [126, 127] The CUS sites within HKUST-1 face the interior of the largest pore. Poreblazer[76] identified a pore limiting diameter of 6.4 Å (see Table 5). This can be compared to the dimensions of the adsorbates, shown in Table 6 (only data for methane and ethane was found[128], but the dimensions of ethylene are expected to be quite similar to those of ethane). It can be seen that the kinetic diameters of all three adsorbates are significantly smaller than the pore limiting diameter and thus no significant diffusion limitations are expected.

Table 6: Dimensions of adsorbates

| Molecule | x | y | z |
|---|---|---|---|
| Methane[128] | 3.829 Å | 4.101 Å | 3.942 Å |
| Ethane[128] | 3.809 Å | 4.079 Å | 4.871 Å |

The ethylene adsorption on HKUST-1 is used to validate the new parameters for the Cu-$\pi$ interaction obtained in this work, as well as the changes implemented in the parameter fitting procedure. As illustrated in Figure 18, the CUS parameters derived from periodic DFT calculations lead to predicted isotherms that are practically indistinguishable from those obtained with parameters derived from the previous cluster calculations[18]. Furthermore, both sets of predicted isotherms agree very well with the experimental data of He et al.[37] at both reported temperatures. This is in marked contrast to the results obtained with the standard DREIDING potential (i.e., without including the specific Cu-$\pi$ interaction), which dramatically underestimate adsorption. It should be noted that the experimental pressure range for this data set is much lower than for the data used in previous work, which went up to 7 bar[18]. This makes the validation even more stringent,

as it focuses on the region in which solid-fluid interactions are dominant, and therefore where the effect of the CUS interaction will be most important.

The good agreement obtained with both DFT-based approaches confirms that the MOF cluster employed previously[1] was large enough to accurately capture the local interactions in the vicinity of the CUS, and that the small changes introduced to the fitting procedure do not have a significant impact on adsorption predictions for this particular system. Nevertheless, the decision was made from this point forward to use periodic DFT calculations where possible, because as previously mentioned this will improve consistency of the fitting process and eliminate potential inaccuracies due to the limited size of cluster models. In particular, it will likely improve the accuracy of modelling adsorbates where electrostatics play an important role, as these interactions are typically long-ranged in nature (see Chapter 5). Furthermore, using periodic calculations obviates the need for constructing different cluster models for MOFs that contain more than one inorganic SBU, such as UMCM-150 (see below).

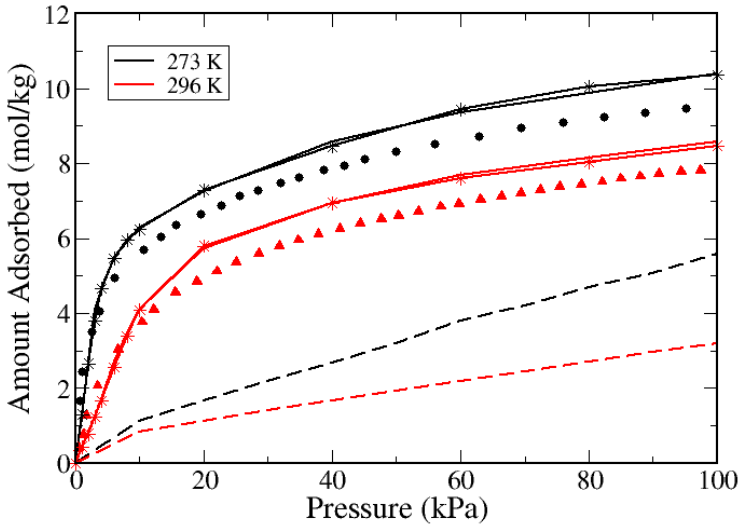


Figure 18: Comparison between simulated (lines) and experimental[37] (symbols) ethylene adsorption in HKUST-1: solid line - periodic DFT model; starred line - cluster DFT model; dotted line - standard LJ model (without CUS interaction)

### 3.3.2 *PCN-16*

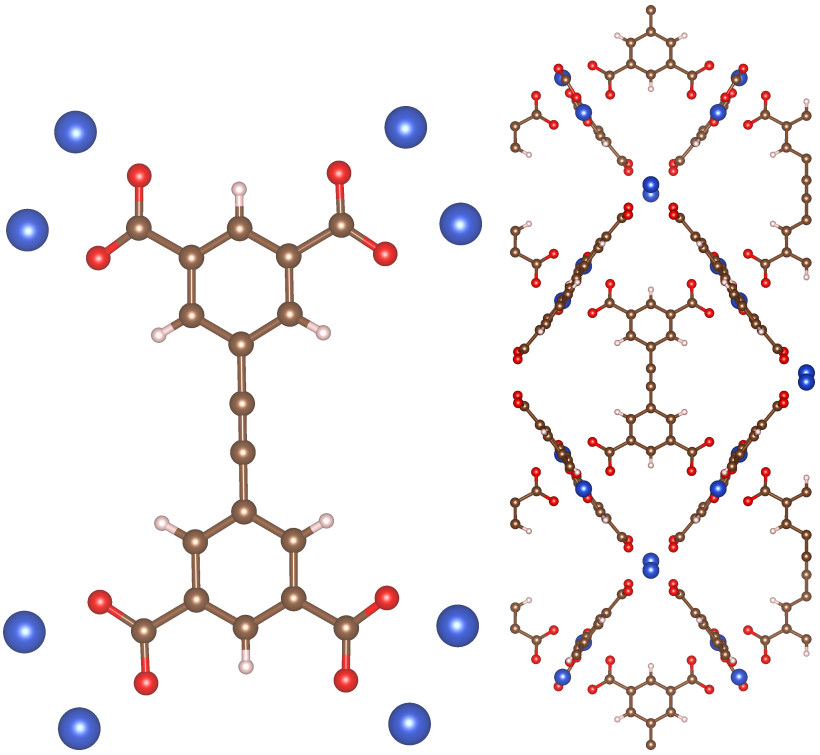

(a) Linker (b) Topology

Figure 19: Diagram showing the linker (a) and the unit cell topology (b) of PCN-16. Color code for atoms is: blue-copper, red-oxygen, brown-carbon and white-hydrogen.

PCN-16[129] has the composition $Cu_2$(ethynediyl-bis (benzenedicarboxylate)). Similar to HKUST-1, it also contains a copper paddle wheel complex, and the SBU is again made up of the two copper atoms bridged by four carboxylate functionalities. However, the organic linker connects to four copper paddle wheels (Figure 19.a), leading to a trigonal structure. The topology of PCN-16 is often described as being of the *nbo* type[130], however, as discussed in more detail by Li et al.[131], a description using the *fof* net gives a more complete representation of the topological features. The same applies to the isoreticular systems MOF-505 and NOTT-101. Additionally, the much longer organic linker than in the case of HKUST-1 leads to a unit cell which is elongated in one direction (Figure 19.b). This creates two cage types, one octahedral cage which is roughly spherical and has a diameter of $\approx 7$ Å, and a larger elliptical cage.[132] These cages are interconnected by two types of

windows that lead to a channel-like pore structure with a pore limiting diameter of 6.32 Å as identified by Poreblazer (see Table 5). This indicates that the pore network is fully accessible to all three gases. The CUS sites present in this MOF face into the smaller octahedral cage.

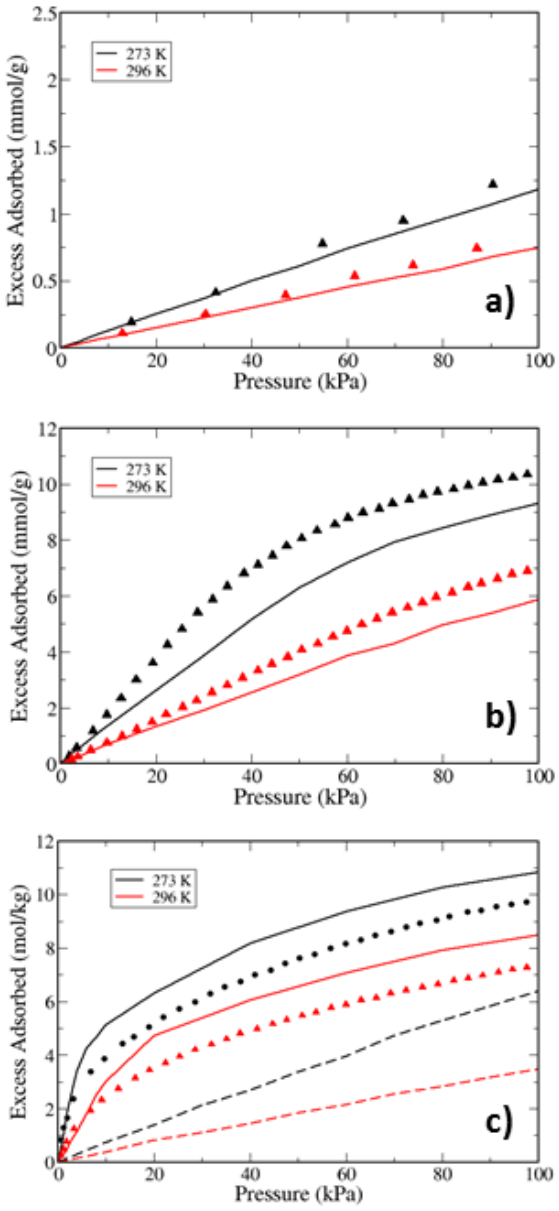


Figure 20: Simulated (lines) and experimental[37] (points) adsorption isotherms in PCN-16 for: a) methane, b) ethane, c) ethylene. For ethylene, the solid line shows results of the periodic DFT model and the dashed line is for the standard LJ model (without CUS interaction).

As illustrated in Figure 20, experimental isotherms of both methane and ethane are captured relatively well by the standard LJ model across the full pressure range and at two different temperatures, although there is a slight underestimation present in ethane simulations. These simulations did not account for any electrostatics or CUS-specific interaction, confirming that the adsorption mechanism is mainly dominated by van der Waals forces for those two adsorbates. However, the standard LJ model fails completely at describing ethylene adsorption, especially at the low pressure region (Figure 20.c). This failure in the Henry's law region suggests that the solid-fluid interaction is being greatly underestimated, as already highlighted in previous work[35]. In contrast to the linear behaviour of the simulations with the LJ model, the experimental isotherm has a steep initial uptake due to the strength of the CUS, and as these sites begin to fill, the isotherm levels off. The new model captures this behaviour of the ethylene isotherm very well, especially in the low pressure region.

The good agreement between experiment and simulation for ethylene in PCN-16 using the CUS parameters determined from DFT calculations on HKUST-1 suggests that these parameters are indeed transferable to different CUS-containing MOFs with the same type of SBU. Nevertheless, a slight overestimation across the entire simulated isotherm is observed. To better quantify the degree of agreement, the root-mean-squared deviation (RMSD) was computed between simulated and experimental isotherms, calculated at the experimental pressure points. The adsorption pressure points of the simulated isotherm had to match up with the recorded experimental points for a fair comparison of adsorption difference; this was achieved through cubic spline interpolation of the simulated isotherm. The RSMD was then calculated from Equation 44, using the difference between experiment and simulation for each pressure point along the isotherm. The RSMD for each MOF was then averaged over the two isotherm temperatures (273 K and 296 K).

$$\mathrm{RSMD} = \sqrt{\frac{\sum_0^n (\mathrm{Ads}_{\mathrm{Sim}} - \mathrm{Ads}_{\mathrm{Exp}})^2}{N}} \tag{44}$$

This is shown in Table 7 for all adsorbates and all MOFs studied in this work. The systematic overestimation observed for ethylene in Figure 20.c is indeed reflected in a somewhat larger RMSD for that adsorbate, compared to methane and ethane. However, given that matching the adsorption isotherms at relatively low pressures and temperatures is a rather stringent test of the new model, the agreement is satisfactory.

Table 7: RMSD between simulated and experimental adsorption isotherms.

| MOF | Methane (mmol/g) | Ethane (mmol/g) | Ethylene (mmol/g) |
|---|---|---|---|
| PCN-16 | 0.093 | 0.844 | 1.083 |
| NOTT-101 | 0.029 | 0.418 | 1.170 |
| MOF-505 | 0.054 | 1.398 | 2.254 |
| MOF-505 (Scaled) (a) | 0.054 | 0.160 | 0.908 |
| UMCM-150 ($Cu_2$) (b) | 0.062 | 0.504 | 1.325 |
| UMCM-150 ($Cu_2/Cu_3$) (c) | 0.062 | 0.504 | 0.997 |
| UTSA-20 | 0.598 | 1.372 | 1.670 |
| UTSA-20 (Blocked) (d) | 0.070 | 0.562 | 0.433 |

(a) simulated isotherm scaled by 0.8 to account for incomplete equilibration of experiment (b) all CUS assumed to behave equivalently, (c) separate CUS parameters used for trimer SBU, (d) small cages blocked.

### 3.3.3 *NOTT-101*

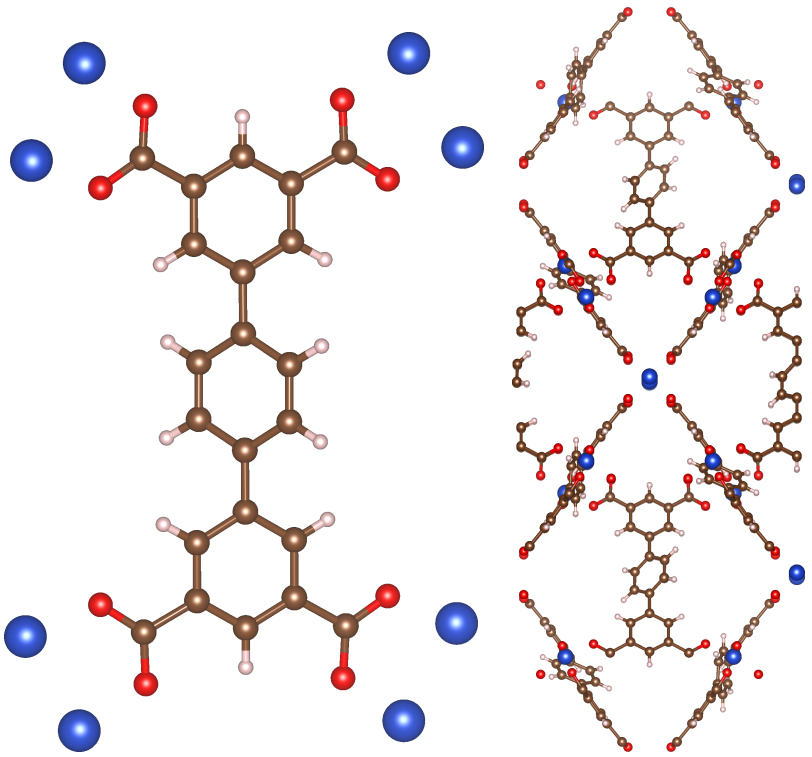

(a) Linker (b) Topology

Figure 21: Diagram showing the linker (a) and the unit cell topology (b) of NOTT-101. Color code for atoms is: blue-copper, red-oxygen, brown-carbon and white-hydrogen.

NOTT-101[133], shown in Figure 21.b, is very similar to PCN-16, retaining the *fof*[131] topology with two pore types interconnected by two triangular windows on one axis[133]. However, the linker is slightly longer due to the central ethynyl group, found in the PCN-16 linker, being replaced with an aromatic ring connecting the benzene carboxylate moieties, as shown in Figure 21.a. In the case of the NOTT family, the connecting windows have been observed to increase in size with increasing linker length[133]. Poreblazer identified a pore limiting diameter of 5.6 Å, which due to the channel nature of the MOF can be attributed to one of these triangular windows. Comparing this value to the dimensions of the adsorbates (Table 6) again suggests the absence of diffusional limitations for the three gases in this MOF.

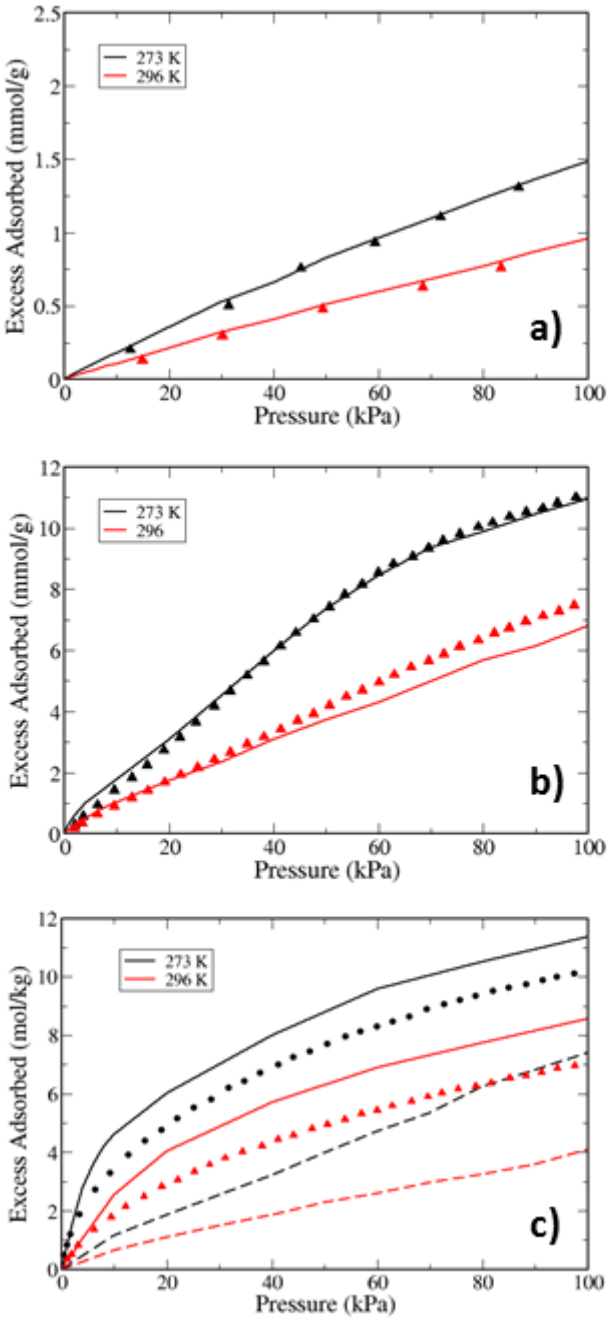


Figure 22: Simulated (lines) and experimental[37] (points) adsorption isotherms in NOTT-101 for: a) methane, b) ethane, c) ethylene. For ethylene, the solid line shows results of the periodic DFT model and the dashed line is for the standard LJ model (without CUS interaction).

In the case of NOTT-101, simulations using the DREIDING/TraPPE models predict adsorption of methane and ethane exceptionally well (Figures 22.a/b), further confirming the suitability of this model for saturated hydrocarbons. A similar trend to that of PCN-16 can also be observed for ethylene adsorption (Figure 22.c). The standard model again fails to identify the CUS as the preferential site and strongly underpredicts adsorption across the whole isotherm. The new transferable model greatly improves predictions and captures the correct shape of the isotherm. Again a slight overestimation is observed, of similar magnitude to that of PCN-16 (see Table 7), suggesting that this may be a systematic issue. However, this was also observed in HKUST-1, albeit to a lesser extent (see Figure 18), implying that this is not a problem caused by transferring the CUS parameters from one MOF to another. This will be elaborated upon later in this chapter.

### 3.3.4 *MOF-505*

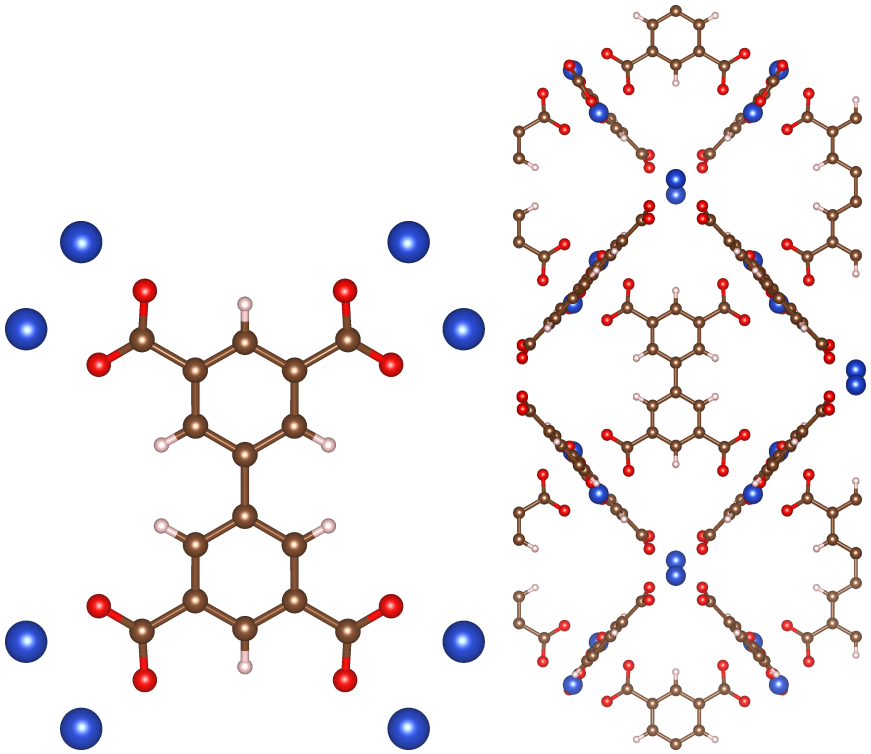

(a) Linker (b) Topology

Figure 23: Diagram showing the linker (a) and the unit cell topology (b) of MOF-505. Color code for atoms is: blue-copper, red-oxygen, brown-carbon and white-hydrogen.

MOF-505[134], also called NOTT-100, is from the same family as NOTT-101 and therefore retains the same *fof*[131] topology and general pore structure, which can be observed through comparison of MOF-505 in Figure 23 and NOTT-101 in Figure 21. The main difference to the two previous MOFs is the shorter organic linker, as shown in Figure 23.b. As mentioned, the linker length has been shown to affect the window size of this MOF type, in this case creating smaller windows[133]. This was confirmed using Poreblazer, which reported a smaller limiting diameter of 4.53 Å for MOF-505, compared to 5.60 Å for NOTT-101. This is now smaller than some of the adsorbate dimensions for ethane and ethylene (see Table 6), which may anticipate some diffusion limitations.

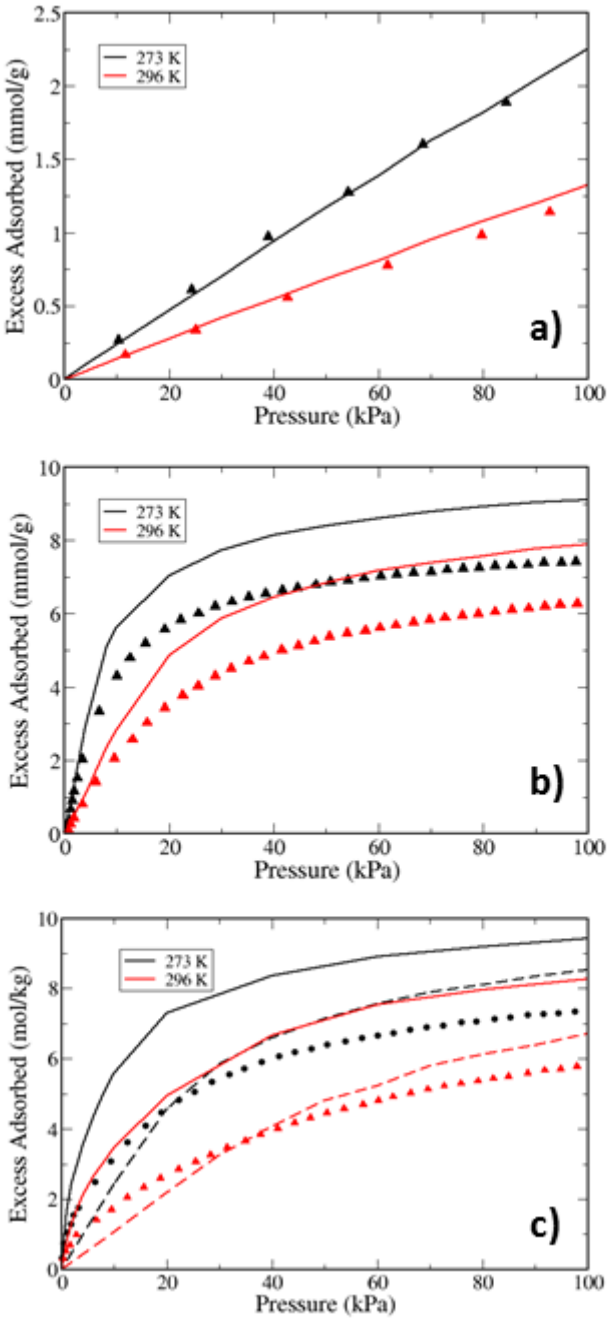


Figure 24: Simulated (lines) and experimental[37] (points) adsorption isotherms in MOF-505 for: a) methane, b) ethane, c) ethylene. For ethylene, the solid line shows results of the periodic DFT model and the dashed line is for the standard LJ model (without CUS interaction).

It can be seen in Figure 24.a that the simulations again accurately capture experimental methane adsorption (the RMSD is similar to that in the previously studied MOFs, see Table 7). In contrast, simulated ethane adsorption is now systematically overestimated in comparison with experiment (Figure 24.b). This is somewhat surprising as both methane and ethane should be attracted to similar adsorption sites, both being fully saturated small hydrocarbons. Figure 24.c shows a similar overestimation of ethylene adsorption from simulations using the new CUS model. This overestimation is much greater than observed for the two previous MOFs, with an RMSD that is about twice that of PCN-16 and NOTT-101 (Table 7). It is also worth noting that the seemingly good quantitative agreement between ethylene simulations using DREIDING (i.e without the CUS parameters) and experiment for this MOF results from fortuitous error cancellation, and belies the intrinsic shortcomings of the standard LJ model. Indeed, closer examination of Figure 24.c shows that the predicted shape of the isotherm (dashed lines) is qualitatively different from experiment, with low pressure adsorption being underestimated, followed by overestimation at higher pressures. Once more, this is due to the inability of the standard approach to describe adsorption at the CUS.

One possible explanation for the systematic overestimation observed in the case of ethylene adsorption with the new model is that the CUS interaction parameters transferred from HKUST-1 lead to stronger adsorption energies than observed in MOF-505. This was tested by fitting new CUS parameters from periodic DFT calculations on MOF-505 (Table 4). As the interaction strength at the minimum of the DFT profile was found to be -22.6 kJ/mol, in comparison to -23.3 kJ/mol for HKUST-1, this is unlikely to be the cause of the observed overestimation. This was confirmed by running GCMC simulations using the new MOF-505 parameters, shown in Figure 25. These parameters lead to almost identical isotherms compared with those obtained with the original HKUST-1 CUS parameters, confirming that the CUS interaction for the copper paddlewheels is generally consistent across different MOFs. This also confirms that the overestimation, which is also observed for ethane, is not a consequence of the assumption of parameter transferability.

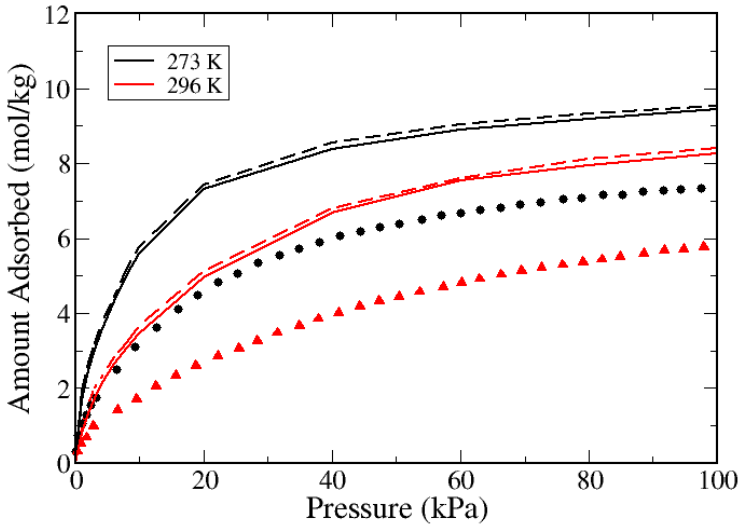


Figure 25: Comparison between simulated (lines) and experimental[37] (points) ethylene adsorption isotherms in MOF-505. The solid line shows results from the original HKUST-1 parameters, while the dashed line shows results using new parameters obtained from DFT calculations on MOF-505.

Another possible explanation is that the smaller cages of MOF-505 are inaccessible to the larger adsorbates, ethane and ethylene. This could explain why adsorption of those two gases is overestimated, while that of methane is not. However, this is unlikely because due to the channel-like nature of the pore topology, blocking the small cages would prevent access of the adsorbate molecules to the remainder of the pore space. Nevertheless, this hypothesis was tested by conducting a GCMC simulation of ethane for MOF-505 in which the different cages were blocked with pseudo-atoms which filled the blocked cages but did not interact outside the cage.

In the case of MOF-505 there are two cage types which are both roughly spherical. Therefore, to block the cage in GCMC simulations an atom is inserted into the centre of the given cage. The atom's $\sigma$ value controls the excluded volume, while $\epsilon$ is set at 1000.0 K to give a sharp transition between the repulsive and attractive regions. The high cut-off value for this interaction is made equal to $\sigma$ to ensure that the blocking atom does not affect adsorption outside the blocked cage.

Additionally, the correct blocking diameter for the cage must be determined. This is achieved by running GCMC simulations at the full capacity of a given adsorbate, in this case methane, with a range of blocking diameters for each cage type. When the drop in the capacity is no longer linear with respect to the increase in blocked volume, then the blocked atom must have begun overlapping with framework atoms and the cage is effectively fully blocked. In Figure 26 this effect can be observed for the small cage at a blocking volume of 275 $Å^3$, which corresponds to a blocking diameter of 6.5 Å. In Table 8 the two blocking diameters for each cage type can be seen.

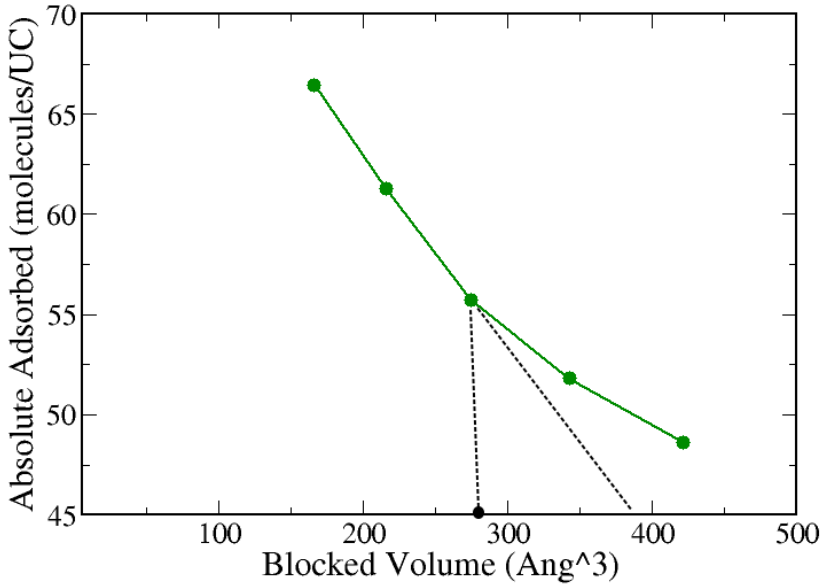


Figure 26: Methane adsorption in MOF-505; solid line: simulation with varying blocked volume

Table 8: Selected blocking diameter for each cage of MOF-505

| Cage Type | Blocking Diameter |
|---|---|
| Small Cage | 6.5 Å |
| Large Cage | 8.5 Å |

As can be seen in Figure 27, this led to poor agreement between simulation and experiment. The removal of the small cages leads to a much lower initial uptake of

ethane, as the strong van der Waals sites in the small cage are no longer available, and to a large underestimation of the adsorbent capacity.

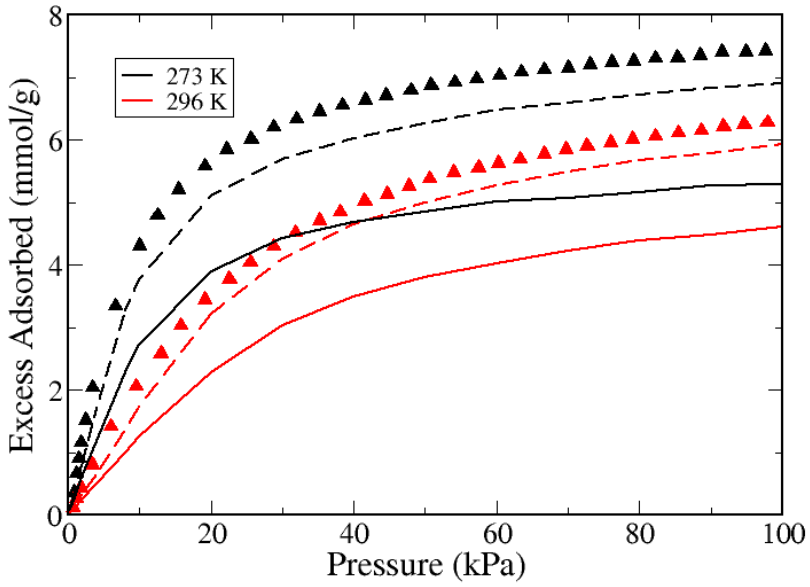


Figure 27: Comparison between simulated (lines) and experimental[37] (points) ethane adsorption isotherms in MOF-505. The solid line shows results from simulations with all small cages blocked, while the dashed line shows results from simulations with one large and one small cage blocked.

The final hypothesis that was considered was incomplete equilibration of the experimental isotherms for both ethane and ethylene. This consideration was prompted by the rather small estimated pore limiting diameter of 4.53 Å in MOF-505. As can be seen in Table 6, methane will likely be unaffected by the smaller window size, as all dimensions of the adsorbate are smaller than the pore limiting diameter. However, in the case of ethane, and therefore also ethylene, the adsorbate has one dimension that is longer than the pore limiting diameter. This means that those molecules need to find the correct orientation to diffuse through this constriction. As such, although both those gases will ultimately have full access to the entire pore volume of the MOF at equilibrium, it is likely that diffusion of ethane and ethylene will be much slower than that of methane, which raises questions as to whether the experimental measurements have truly reached equilibrium.

This hypothesis was again tested by partially blocking the pore space of the MOF in GCMC simulations, but in this case one small and one large cage of the unit cell were blocked to represent incomplete diffusion through the MOF in a simplified way. As illustrated in Figure 27 this led to much better agreement in ethane isotherms. Interestingly, the simulated isotherms with blocked pores could be replicated by simply scaling the original (unblocked) isotherms by a constant factor. This reflects the fact that the simulations are simply restricting access to a portion of the pore volume, without specifically blocking one type of cage. Optimal agreement with experiments for ethane at both temperatures is obtained by scaling the original simulated isotherms by 0.8, as shown in Figure 28.a. The same scaling factor was then applied to ethylene, with results shown in Figure 28.b. Although a systematic overestimation is still observed, this is now of the same magnitude as observed in the other MOFs of this family (compare the RMSDs in Table 7), reinforcing the argument that the discrepancies originally observed for ethane and ethylene have the same origin.

Although this analysis presents a compelling case for incomplete experimental equilibration as the cause of the observed discrepancies for MOF-505, it cannot be confirmed without performing additional experiments. Nevertheless, further support for the hypothesis comes from recent adsorption experiments by Jiao et al.[135] on NOTT-101 and a related material, ZJNU-80. Those authors have observed experimental isotherms with unusual curvature and strong hysteresis for several butene isomers, whereas such effects were absent in isotherms of small gases like $CO_2$, $N_2$ and $CH_4$ and were practically negligible for other C4 hydrocarbon isomers. Such marked difference between chemically similar isomers is unlikely to arise from different adsorption energies, and is much more likely to be due to diffusional limitations experienced by some of the butene isomers. This is consistent with this work's interpretation of the MOF-505 results for ethane and ethylene, as the length of the butene isomer molecules is larger than the window size in NOTT-101, potentially leading to such diffusional limitations. Clearly, further work, both experimental and theoretical, is required to unequivocally clarify this issue.

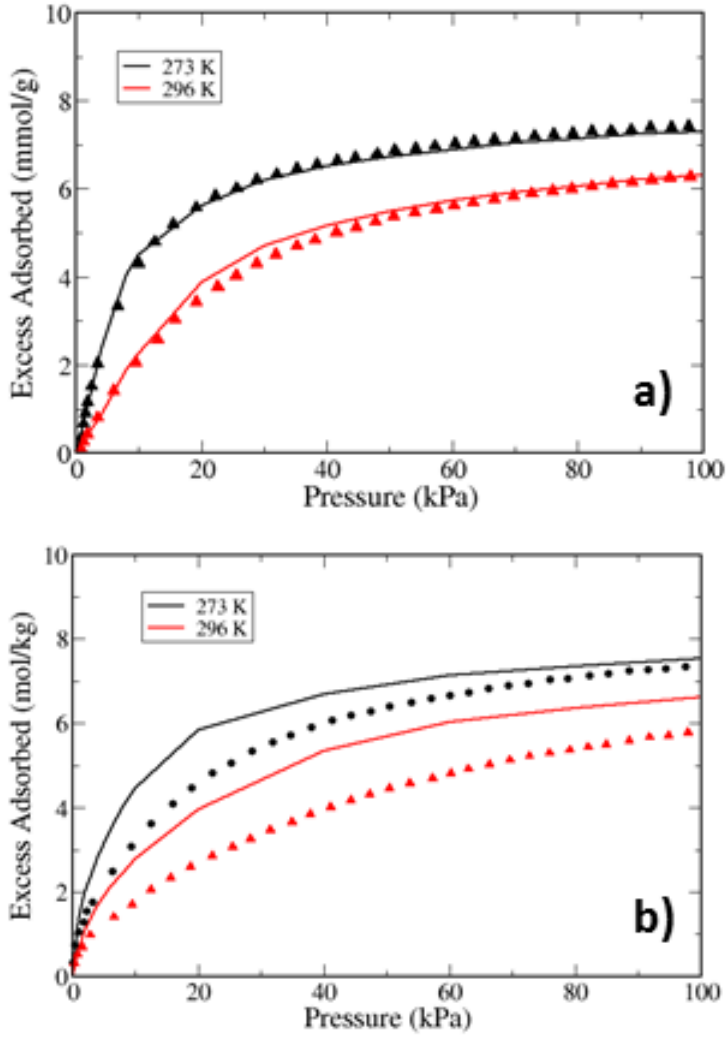


Figure 28: Simulated (lines) and experimental[37] (points) adsorption isotherms in MOF-505 for: a) ethane, b) ethylene. Simulations are scaled by a factor of 0.8 to represent incomplete equilibration of the experiments.

### 3.3.5 *UMCM-150*

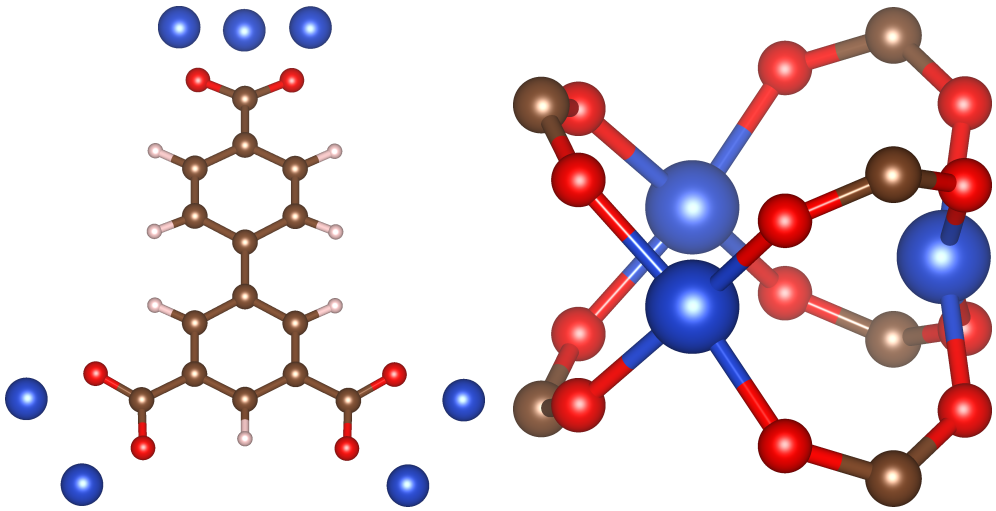

(a) Linker (b) Trimer

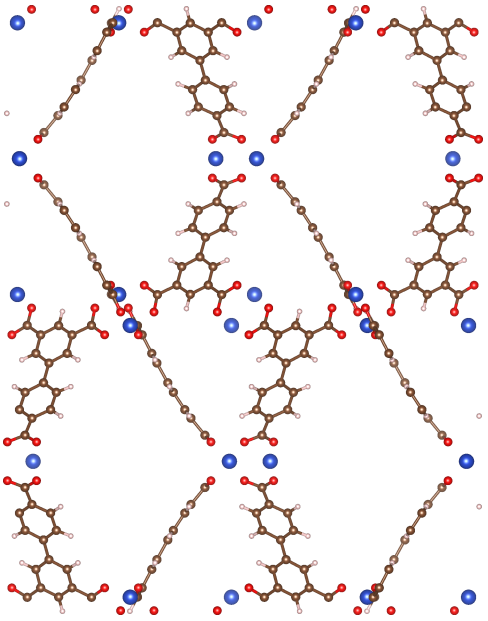

(c) Topology

Figure 29: Diagram showing the linker (a) and the unit cell topology (c) of UMCM-150, as well as a detailed view of the Cu-trimer metal center (b). Color code for atoms is: blue-copper, red-oxygen, brown-carbon and white-hydrogen.

UMCM-150[136] is a much more complex MOF than those previously studied in this work and has the composition $Cu_3(bhtc)_2$, where (bhtc) is biphenyl-3,4′,5-tricarboxylate[126]. This MOF is made up of two different types of inorganic build-

ing units. The first is the standard copper dimer paddlewheel MOF, however there is also a copper trimer unit[126, 136], as shown in Figure 29.b, which also exhibits CUS. The two types of metal building units are joined using an asymmetrically substituted linker molecule, as shown in Figure 29.a/c, leading to three cage types[136]: one large trigonal bipyramidal cage with dimensions 10.2 x 13.7 Å, one smaller hexagonal bipyramidal cage with dimensions 5.2 x 5.8 Å, and finally a small cylindrical cage with a diameter of 4.2 Å.[126] The CUS interaction sites are facing into the two larger cages but not accessible from the smallest cage.

Poreblazer identified the pore limiting diameter as 8.8 Å but only found one dimension for percolation in what should be a 3D pore system (See Table 5). This indicates that the percolation path does not fully explore all the cages but flows through the largest cages only. Therefore this large pore limiting diameter does not guarantee that the adsorbates have full access to the smaller cages, as unlike in the previously investigated MOFs, diffusion through the large pores does not require access to the smaller cages.

The isotherms in Figure 30.a/b show that simulations accurately capture both methane and ethane adsorption, suggesting that the entire pore volume of UMCM-150 is indeed accessible to both adsorbates (and hence also to ethylene). In the initial attempt to describe adsorption of ethylene on the CUS of this material, it was assumed that all metal sites (both in the dimer paddlewheel and in the trimer SBU) behaved equivalently. This assumption amounts to using the parameters obtained in the HKUST-1 paddlewheel for both types of CUS. In Figure 30.c it can be seen that the new model simulation overestimates adsorption by a greater degree than observed in NOTT-101 and PCN-16 (the RMSD for ethylene on this MOF, shown in Table 7, is significantly higher than for the other MOFs), although it is worth noting that it still greatly improves agreement in comparison to the standard LJ model. The reason for the additional discrepancies could lie in the identical treatment of both copper building units using parameters fitted for only copper dimers. Initial DFT calculations indeed indicated that this is likely the cause, as the optimized DFT interaction energy between ethylene and an unsaturated Cu atom in the trimer was found to be $\approx$ -11 kJ/mol at a binding distance of 3.1 Å. This is

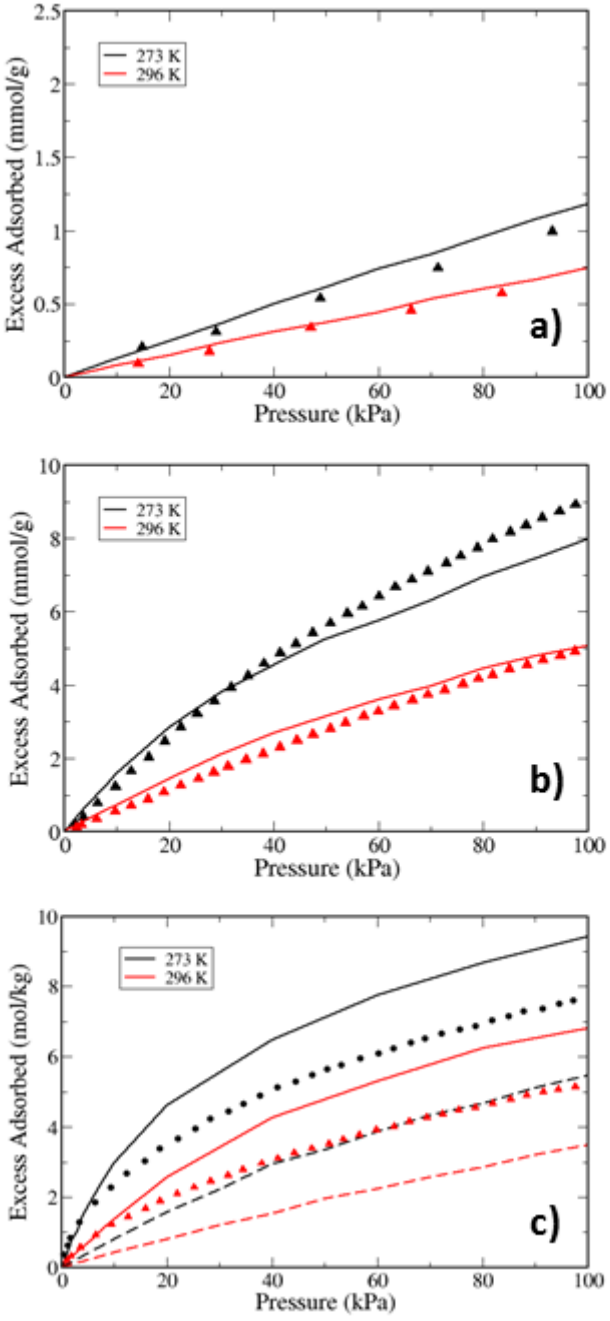


Figure 30: Simulated (lines) and experimental[37] (points) adsorption isotherms in UMCM-150 for: a) methane, b) ethane, c) ethylene. For ethylene, the solid line shows results of the periodic DFT model and the dashed line is for the standard LJ model (without CUS interaction).

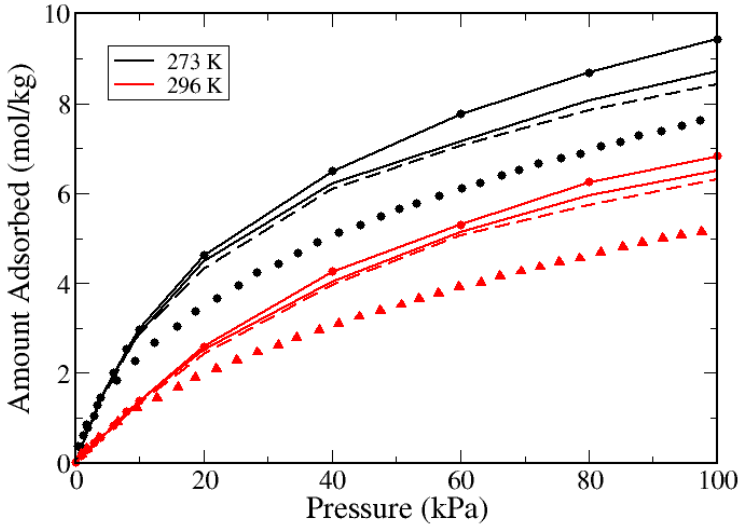


Figure 31: Comparison between simulated (lines) and experimental[37] (points) ethylene adsorption isotherms in UMCM-150. The solid line shows results using separate CUS parameters for Cu dimers and trimers, while the solid line with circles line shows results obtained considering all Cu atoms to behave equivalently, the dashed line shows results using CUS parameters for Cu dimers and no CUS interaction for trimers.

much less attractive than previously recorded for the paddlewheel dimer in both HKUST-1 and MOF-505, for which the DFT interaction energy is ≈ -23 kJ/mol and the binding distance is 2.6 Å. As such, a full DFT profile and new CUS parameters were obtained for the copper trimer of UMCM-150 using the procedure outlined in the Methodology section.

As can be seen in Figure 31, treating the metal building units independently leads to better agreement between simulation and experiment. Although a systematic overestimation is still observed, this is now of the same order as in all the previously studied MOFs (see Table 7). Additionally, it was found that turning off the CUS interaction completely for the copper trimer leads to very similar simulation results as obtained by treating the trimer independently. This therefore indicates that the role of the copper trimer CUS interaction in ethylene adsorption is relatively small at the considered temperatures, and therefore can potentially be ignored. However, ignoring this interaction on the basis of a comparison to ex-

perimental isotherms may lead to an incorrect distribution of adsorbed molecules, which may have a measurable impact on pure-component or mixture adsorption at different thermodynamic conditions.

### 3.3.6 *UTSA-20*

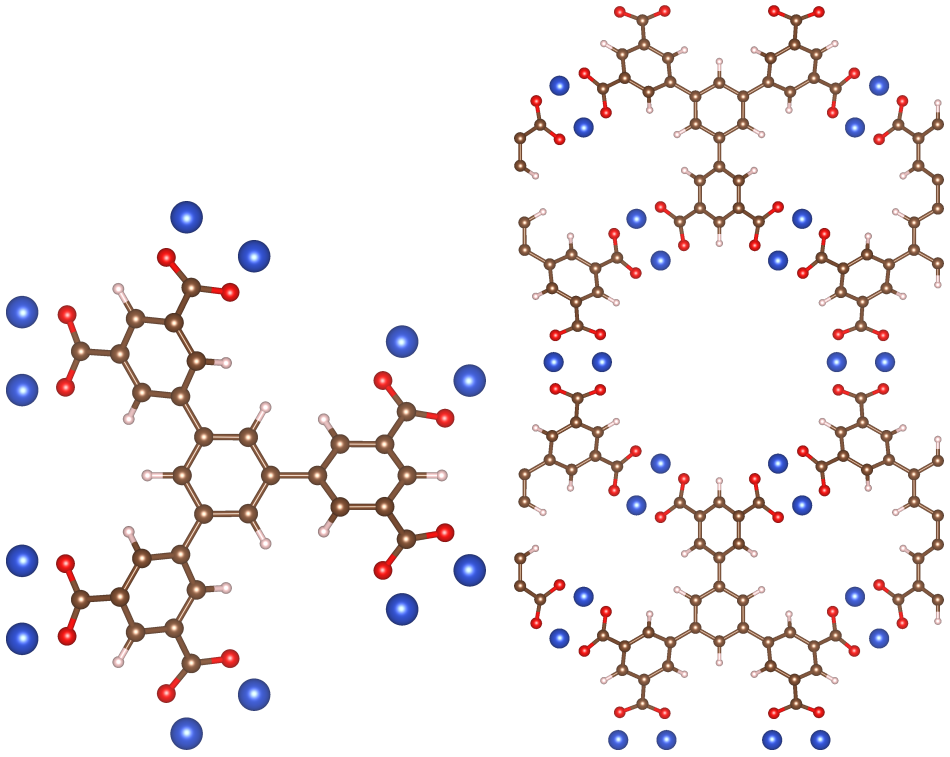

(a) Linker (b) Topology

Figure 32: Diagram showing the linker (a) and the unit cell topology (b) of UTSA-20. Color code for atoms is: blue-copper, red-oxygen, brown-carbon and white-hydrogen.

UTSA-20[137] has the composition $Cu_3$(BHB) and an overall topology of type *zyg*[137]. The MOF is made up through self-assembly of a very large organic hexacarboxylate linker BHB (BHB = 3,3′,3″,5,5′,5″-benzene-1,3,5-triylhexabenzoate), shown in Figure 32.a, and copper paddlewheel as the inorganic building block[137]. The complex linker group leads to two pore types, a rectangular pore with dimensions 3.4 x 4.8 Å and a cylindrical pore with a diameter of 8.5 Å.[137] As can be seen in Figure 32.b this MOF has a very high density of CUS, which makes it an interesting candidate to further test the new CUS model. The CUS sites point to-

wards, and therefore will be accessible from, both cage types. The presence of a smaller pore again raises questions about adsorbate accessibility to the full MOF structure. Similarly to UMCM-150, this complex structure also does not require diffusion through the small cages to access the larger cages, therefore the pore limiting diameter found by poreblazer was 8.8 Å and percolation was in 1 dimension.

In Figure 33, it can be seen that simulations fail to describe experimental adsorption for all three adsorbates. In fact, this is the only MOF studied where methane simulations are not correctly predicted. The fact that adsorption of all hydrocarbons, both saturated and unsaturated, is overestimated suggests that this is not related to the CUS model. Also, as methane is roughly spherical it would be expected to diffuse relatively quickly through the framework, therefore insufficient experimental equilibration is not a likely explanation for the observed discrepancies. Instead, the consistent overestimation may indicate that parts of the MOF (most likely the small rectangular cages) are not fully accessible to the three adsorbates. Furthermore, as Poreblazer identified percolation in only 1 dimension, with a large pore limiting diameter, this suggests molecules are able to diffuse through the MOF system using only the large pores, therefore inaccessible small pores would not prevent or hinder diffusion in experiments.

Simulations with inaccessible cages were again conducted using the pore blocking technique outlined for MOF-505 (a blocking diameter of 3.8Å was found reasonable). The small cages and windows to these cages were blocked, and GCMC simulations were performed on the new structure. In Figure 34, it can be seen that making the small cages inaccessible in the GCMC simulations greatly improves agreement with experiment for all adsorbates. Nevertheless, agreement is not perfect, especially for ethylene for which there is a slight underestimation in the low pressure region. Our blocking approach is simply based on excluded volume, whereas in reality the cages will most likely be blocked by occluded solvent or reactant molecules. It has been shown that these occluded molecules can actually act as extra adsorption sites, and thus slightly enhance adsorption at low pressures [32, 138], which could potentially explain the differences observed in Figure 34.c. More detailed studies are needed to fully clarify this issue, but this is

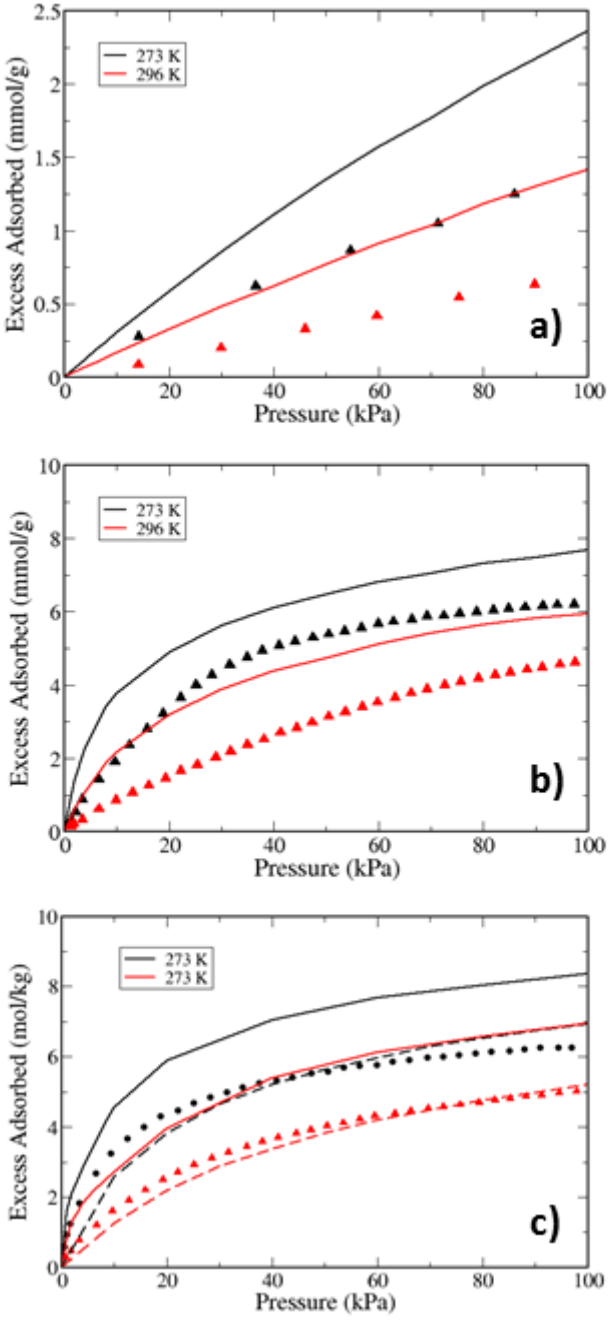


Figure 33: Simulated (lines) and experimental[37] (points) adsorption isotherms in UTSA-20 for: a) methane, b) ethane, c) ethylene. For ethylene, the solid line shows results of the periodic DFT model and the dashed line is for the standard LJ model (without CUS interaction).

outside the scope of this work. The main point to be drawn from this, however, is that whatever the root cause of the differences between simulation and experiment for UTSA-20, they are very unlikely to be due to the assumption of transferable parameters from the HKUST-1 paddlewheel.

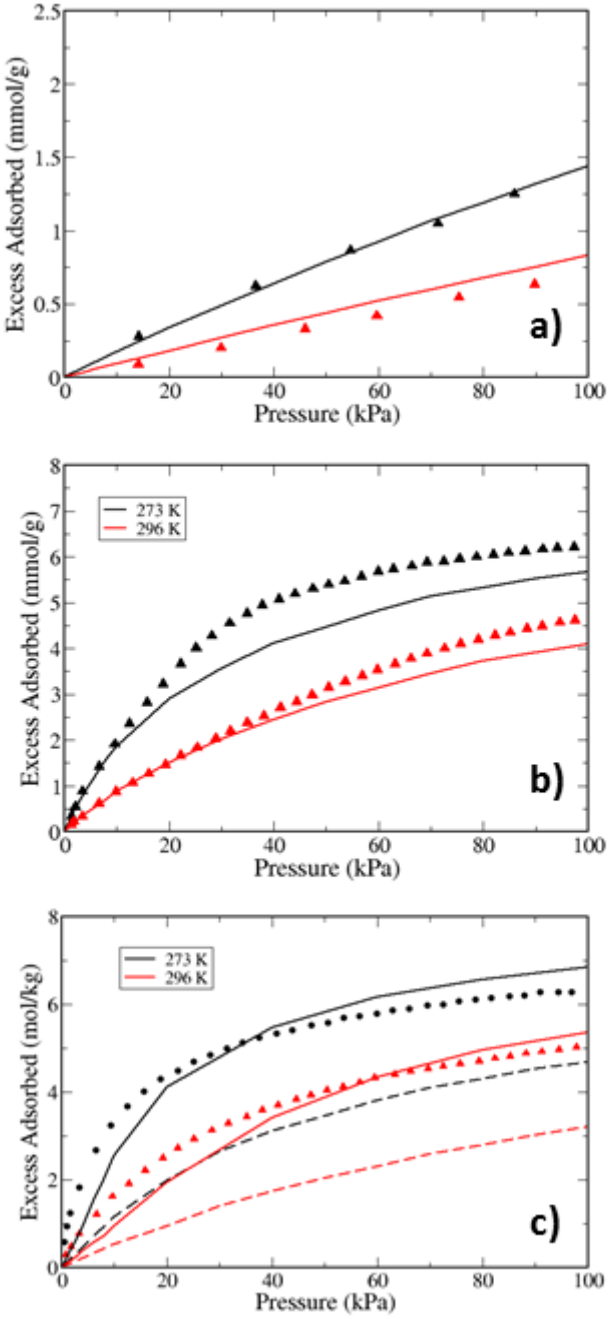


Figure 34: Simulated (lines) and experimental[37] (points) adsorption isotherms in UTSA-20 with all small cages blocked for: a) methane, b) ethane, c) ethylene. For ethylene, the solid line shows results of the periodic DFT model and the dashed line is for the standard LJ model (without CUS interaction).

## 3.4 CONCLUSION

This work builds upon a computational approach for describing the complex orbital interactions present for some adsorbates in MOFs containing unsaturated metal sites. Using DFT-derived parameters for ethylene adsorption on a single MOF material (HKUST-1) very good agreement with experimental isotherms on PCN-16 and NOTT-101 was obtained. Adsorption of both ethylene and ethane on MOF-505 was overestimated, but a possible explanation for this is insufficient equilibration of the experimental measurements. When this was accounted for in an approximate way, the same level of agreement as in the other MOFs was retrieved. In the case of UMCM-150, two different types of CUS sites were identified. It was shown that the CUS parameters were not transferable from a Cu paddlewheel unit to a Cu trimer unit, and that the latter required potential parameters to be separately determined. Using a correct description of the adsorption energy at this new site, good agreement with experiment was once again observed. Finally, adsorption of methane, ethane and ethylene on UTSA-20 was consistently overestimated by roughly the same amount. A reasonable explanation for this observation has been proposed, based on inaccessible regions of the pore network, but additional work is needed to fully clarify this issue.

The new CUS model was already shown to be transferable across different hydrocarbon adsorbates (e.g., ethylene to propylene)[18] but in this work it has been clearly demonstrated that it is in fact also transferable between different adsorbents of the same class. This is a key step in the development of a model capable of accurately predicting adsorption in CUS-containing MOFs for practical applications, including large-scale computational screening. The key for the success of this model lies in the decomposition of the DFT energy profiles to isolate the contribution of the Cu-$\pi$ interaction and in a careful consideration of the local nature of this interaction. This was achieved through the addition of a new interaction site at the center of the olefin double bond, together with a cut-off scheme that prevents the metal site from interacting with more than one adsorbate molecule at the same time. In a recent paper, Kulkarni and Sholl[104] presented an alternative approach that required the addition of a three-body term to avoid unreasonable adsorbate

configurations. Their predictions of pure-component adsorption isotherms in the same series of MOFs studied here (see Figure S15 of their paper) were not as accurate. Although more detailed analysis of their simulations is required, it can be speculated that the reason for the observed significant overestimation of ethylene adsorption in their paper may be due to the longer range of their CUS potential function, which may be allowing for the metal site to interact with more than one adsorbate molecule.

The success of the CUS modelling approach proposed here opens up the opportunity to develop new CUS parameters for different adsorbates and for accurately simulating competitive binary adsorption across a variety of systems, which is difficult to measure experimentally, and will be explored further in Chapter 4. This thesis will also outline how to expand the CUS model to additionally complex systems in which there is a significant electrostatic contribution to the adsorption energy. This enables it to be applied to polar adsorbates like CO (see Chapter 5), $CO_2$ and $H_2O$. This work aims to highlight that by treating the CUS interaction independently from all other intermolecular forces, it places this CUS model in a prime position to respond quickly to any improvements in the description of these intermolecular forces.

# 4

# SIMULATED PREDICTION OF EXPERIMENTAL BINARY ETHANE/ETHYLENE ADSORPTION

## 4.1 INTRODUCTION

In Chapter 3, a Coordinatively Unsaturated Sites (CUS) model was developed to enable a transferable approach to be used in simulating adsorption in various CUS-containing MOFs. However, only single component adsorption was predicted and, although this has important implications for ground-breaking applications such as gas storage, i.e. for carbon capture and hydrogen storage, far more often in the real world it is multicomponent systems that will be investigated. One such example, which has been a major focus of this thesis, is the application of gas separation, therefore, a key step in this model's development is validation within a context of competitive binary adsorption.

Binary adsorption measurements are notoriously difficult and time consuming to carry out experimentally.[139] Researchers often rely on expensive mass flow controllers and mass-spectroscopic equipment to ensure accurate determination of input and output flow gas compositions, respectively. Furthermore, gases are commonly pre-mixed in a supply vessel, which is not ideal for varying gas compositions, and relies on the assumption that the output composition is continuously the same as that created in the initial cylinder mix. Despite the methods employed for competitive studies, many systems often have a high error associated with the resulting experiments and it can be advantageous to use alternative routes to predict competitive adsorption behaviour. As such, Ideal Adsorbed Solution Theory (IAST)[140] is often used in place of competitive adsorption experiments, either to predict binary behaviour or, at the very least, to validate against binary component experimental data.

IAST uses the single component adsorption isotherms for each adsorbate to predict how the gases will behave in a multicomponent environment, and has been shown to provide relatively good predictions of binary behaviour for various systems.[141] Issues arise when the adsorption of one of the chosen components is very low as, in this case, the error associated with the isothermal data would be relatively high, and this will carry over into the binary system predictions. This is problematic as it is these high/low contrasting systems that are likely to be desirable to study, due to their potentially high gas selectivity and, therefore, potential application in gas separations.

The work by Heinen et al.[101] also shows that, for CUS-containing MOFs, IAST theory begins to break down when considering certain adsorbates. This is due to the fact that IAST theory assumes that the adsorbed phase mixture behaves ideally at constant spreading pressure and temperature. The comparison of simulated binary models for ethylene/ethane adsorption in the presence of CUS interactions with ethylene, in which electron transfer occurs, introduces non-ideality into the system. Therefore, computational modelling could fulfill a pivotal role in the validation of experimental binary adsorption in the case of these complex adsorbents.

The question then becomes how to accurately simulate these binary mixtures. A recent study by Luna-Triguero et al.[93] investigated re-parameterising existing Lennard Jones (LJ) forcefields to obtain better agreement with experiment for single component adsorption in CUS-containing MOFs (a technique discussed in Chapter 3), for various olefin and paraffin gases. The new LJ parameters were then used to predict binary behaviour of these gases. A potential issue with this technique is that the CUS interaction can have a very deep attraction energy while being relatively short range, therefore it is difficult to fully capture this attraction without affecting surrounding nearby binding sites due to the slow decay in the LJ potential. As this is such a different method to this work's proposed quantum based approach, it will be studied in conjunction with the explicit CUS model to assess which approach can best capture the competition of two gases at the binding sites of the MOF.

Heinen et al.[101], as well as Kulkarni et al.[104], have also used coupling quantum mechanical and GCMC approaches to predict binary adsorption behaviour of olefin and paraffin species in CUS containing MOFs. In Chapter 3, the advantages and disadvantages of these approaches were discussed, relative to the CUS model proposed in this thesis. It was shown that while all could potentially improve CUS description, the model proposed in this thesis offered the best balance between modelling accuracy and transferability. Therefore, this chapter will focus on predicting the binary adsorption behaviour of ethylene and ethane mixtures, before comparing this with experimentally determined data as validation. Such a comparison has not been undertaken in any of the aforementioned works, likely due to the scarcity of available data.

Overall, this chapter will demonstrate that the proposed CUS model is capable of describing competitive binary adsorption and provides good agreement with both experimental single and binary data. This represents a positive step towards accurately simulating these binary gas mixtures with the complex CUS systems on a much larger scale, e.g in computational screening of MOFs for gas separation.

## 4.2 METHODOLOGY

A comprehensive description of the concept behind each of the stages of CUS parameter development was provided within the Methodology of Chapter 3. This section will therefore focus on changes to the procedure, and assumes prior reading of Chapter 3.

### 4.2.1 *GCMC simulations*

All adsorption isotherms were obtained through GCMC simulations using the open source code Music.[120] The PMAP grid spacing selected was 0.15 Å(see Chapter 2 for description of PMAPs). For all GCMC simulations that did not include CUS interactions, cavity bias[52] based on the LJ potential maps was used for insertion and deletion trials. As in Chapter 3, all simulations which explicitly included CUS interactions had their insertion and deletion moves randomly chosen without bias. In addition to insertion and deletion trials, molecules were allowed to rotate and translate, using optimized maximum displacements. 500 000 000 steps were used for all singe component non-CUS models GCMC simulations and 100 000 000 were used for all singe component CUS model GCMC simulations. The CUS model simulations used fewer steps due to the higher adsorbed amount which lowered the percentage error, furthermore the additional adsorbates within CUS simulations increased simulation time for each step. The step number was increased to 1 000 000 000 for all binary simulations. The first 50 % of steps were ignored to ensure equilibration, and the remaining steps were split into 20 equal blocks for error analysis. Pressure values were converted to fugacities for input into the simulation code using the Peng-Robinson equation of state[121]. The final absolute adsorbed amounts from the simulations were converted to excess, for comparison with experiment, using the Myers and Monson method.[61]

#### 4.2.1.1 *Standard non-CUS LJ Forcefields*

In the HKUST-1 frameworks, the DREIDING forcefield[56] was used to describe the LJ interactions of all framework atoms apart from copper. The copper atoms are not present in DREIDING and therefore the Universal forcefield (UFF) was used.[55]

For the gas-gas interaction, it has come to this author's attention that an adapted TraPPE united atom forcefield is available for both ethylene[142] and ethane[143]. TraPPE was designed to be applied with long range corrections in bulk fluid simulations, however in adsorption simulations this correction is rarely used.[144] Furthermore, it is also not currently implemented in Music, to the author's knowledge. As such, these modified TraPPE forcefields attempted to implicitly capture this correction within the LJ potential, while continuing to match the experimental vapour-liquid equilibrium data. However, the ethylene forcefield, like TraPPE, was not designed to account for orbital interactions and therefore will be ignored; ethane will still be investigated using this approach as the CUS interaction does not play a major role.

Table 9 shows the two sets of fluid-fluid parameters considered here. The TraPPE forcefield (already applied in Chapter 3) uses a LJ cut-off of 13 Å.[53, 54] For the modified TraPPE, which has been tailored for use in nanoporous structures, ethane parameters were taken from Dubbledam el al.[143] while ethylene parameters are from Liu et al.[142] This forcefield used a LJ cut-off of 12 Å and a shifted potential.

Table 9: LJ parameters for ethane and ethylene, Trappe[53, 54] and modified TraPPE.[142, 143]

| | group | TraPPE | | Modified TraPPE | |
|---|---|---|---|---|---|
| Adsorbate | Group | σ (Å) | ϵ (K) | σ (Å) | ϵ (K) |
| Ethylene | $CH_2$ | 3.675 | 85 | 3.685 | 93 |
| Ethane | $CH_3$ | 3.750 | 98 | 3.760 | 108 |

There will be three variations of solid-fluid forcefields used within the ethane/ethylene simulations in all cases. In the first two models, the solid-fluid interactions

were obtained using the Lorentz-Berthelot combining rules based on the fluid-fluid parameters in Table 9 and the DREIDING/UFF model for the framework sites. These will simply be called the 'TraPPE' and 'Modified TraPPE' models. Finally, there is the Luna-Triguero forcefield (L-T)[93] which was adapted from the modified TraPPE forcefield. For the gas-gas interaction, the exact same values were used as in the modified TraPPE, shown in Table 9. Therefore the exact same cut-off scheme had to be used, LJ cut-off of 12 Å with a shifted potential. It is the mixed solid-fluid LJ parameters which were adapted. The initial LJ parameters for the framework atoms were again taken from the DREIDING forcefield[56] for all framework atoms apart from copper, which was taken from the Universal forcefield (UFF).[55] These values were then mixed with the pure adsorbate parameters using the Lorentz-Berthelot combining rules to obtain an initial guess, but the solid-fluid values were then optimised to better replicate the adsorption isotherm of the given adsorbate. The optimised mixed values can be seen in Table 10. Additionally, in Table 10, the starting point corresponding to the modified TraPPE forcefield can be seen. It is interesting to note that the $\epsilon$ values are relatively untouched while the $\sigma$ values generally increase. The impact of increasing $\sigma$ rather than $\epsilon$ has interesting implication; rather than altering the strength of attraction at the existing binding sites through $\epsilon$, the changes to $\sigma$ likely changes the entire binding landscape. In the case of ethane, the increases in $\sigma$ are not too severe, suggesting that the original values performed relatively well. However, in the case of ethylene the $\sigma$ values are substantially increased, likely in an attempt to match higher adsorption obtained in experiment, arising from the CUS sites. These issues will be further discussed in the Results section.

Table 10: LJ parameters for ethane and ethylene from the Luna-Triguero forcefield[93] and modified TraPPE.[142, 143]

| | Triguero | | | | Modified TraPPE | | | |
|---|---|---|---|---|---|---|---|---|
| | $CH_3$_sp3 | | $CH_2$_sp2 | | $CH_3$_sp3 | | $CH_2$_sp2 | |
| MOF Atom | $\sigma$ (Å) | $\epsilon$ (K) | $\sigma$ (Å) | $\epsilon$ (K) | $\sigma$ (Å) | $\epsilon$ (K) | $\sigma$ (Å) | $\epsilon$ (K) |
| Copper | 3.51 | 16.49 | 3.91 | 15.30 | 3.44 | 16.48 | 3.40 | 15.29 |
| Oxygen | 3.46 | 72.14 | 3.86 | 66.95 | 3.40 | 72.12 | 3.36 | 66.92 |
| Carbon | 3.69 | 71.89 | 4.12 | 66.72 | 3.62 | 71.90 | 3.58 | 66.72 |
| Hydrogen | 3.37 | 28.74 | 3.76 | 26.67 | 3.30 | 28.74 | 3.27 | 26.67 |

#### 4.2.1.2 *CUS Parameters*

The CUS parameters derived for ethylene using the TraPPE forcefield can be seen in Table 11 (the same as those used within Chapter 3).

Table 11: CUS parameters obtained from DFT fitting to Equation 45

| MOF | Adsorbate | LJ | $R_o$ (Å) | $D_o$ (kJ/mol) | $\alpha$ | A | B |
|---|---|---|---|---|---|---|---|
| HKUST-1 | Ethylene | TraPPE | 3.1030 | 10.6324 | 8.0945 | 3.825 | 9.2812 |

The functional form for the parameters shown in Table 11, can be seen in Equation 45.

$$U_{function}(r) = D_o \cdot \left[ exp\left(\alpha\left(1 - \frac{r}{R_o}\right)\right) - 2 \cdot exp\left(\frac{\alpha}{2}\left(1 - \frac{r}{R_0}\right)\right)\right] - \left(\frac{A}{r}\right)^B \quad (45)$$

Equation 46 shows the cut-off scheme applied for the CUS interaction, the same cut-off scheme used in Chapter 3.

$$U_{Cu-\pi}(r) = \begin{cases} 0 & 1.8\ \text{Å} < r \\ U_{function}(r) & 3.5\ \text{Å} \geqslant r \\ U_{function}(r) \cdot \dfrac{(Hicut - r)}{(Hicut - Shiftcut)} & 3.5\ \text{Å} < r < 4\ \text{Å} \\ 0 & r \geqslant 4\ \text{Å} \end{cases} \quad (46)$$

It should be noted that the ethylene Liu et al.[142] parameters (Table 9) could also likely be used in combination with this work's CUS model. This would require fitting new CUS parameters based on this ethylene forcefield's LJ potential (but would not require a new DFT profile to be computed). However, it would also require further coding of shifted potentials into the Monte Carlo LJ software used to isolate the CUS potential from the DFT potential, which is planned future work.

## 4.3 RESULTS AND DISCUSSION

The primary purpose of this chapter is validation of the CUS model against ethylene/ethane binary experimental data. The only available dataset found within literature is the Martins et al.[145] HKUST-1 data. This dataset uses a pelleted HKUST-1 (rather than powder) and therefore will suffer from reduced pore volume[145], furthermore it only contains two binary data points. Therefore the focus of this chapter will be on simulating and validating only HKUST-1, rather than a variety of copper paddlewheel MOFs (Chapter 3). As a number of models will be tested for how they perform in the binary case, there is also a need to understand pure component performance. As such, all the models will first be tested for pure component adsorption on powder HKUST-1; this will enable their performance to be measured on more reliable experimental datasets first, and at a wider temperature and pressure range than was done previously. Additionally, a comparison of powder and pelleted (Martins et al.[145]) HKUST-1 single component data will be conducted, to better understand the effect that pelletisation will have on the experimental binary data.

### 4.3.1 *Ethane Single Component*

In Figure 35 it can be seen that the low temperature/pressure data of Wang et al.[146] and He et al.[37] are in relatively good agreement with each other. However, the temperatures are slightly different at 295-296K possibly suggesting slight under-adsorption for the He et al.[37] data. There is no direct comparison of the Jorge et al.[18] data with the two other datasets, but comparison with the simulations suggest that the adsorption amounts are somewhat higher than those of the Wang et al.[146] and He et al.[37] datasets, even after all datasets are scaled for pore volume effects (see Section 3.2.5)

In Figure 35, the comparison of simulation and experiment shows that the optimised Luna-Triguero forcefield clearly performs the best. For all the temperature and pressure ranges it most closely agrees with all experimental isotherms. As the CUS interaction is not dominant for ethane, this optimisation procedure appears

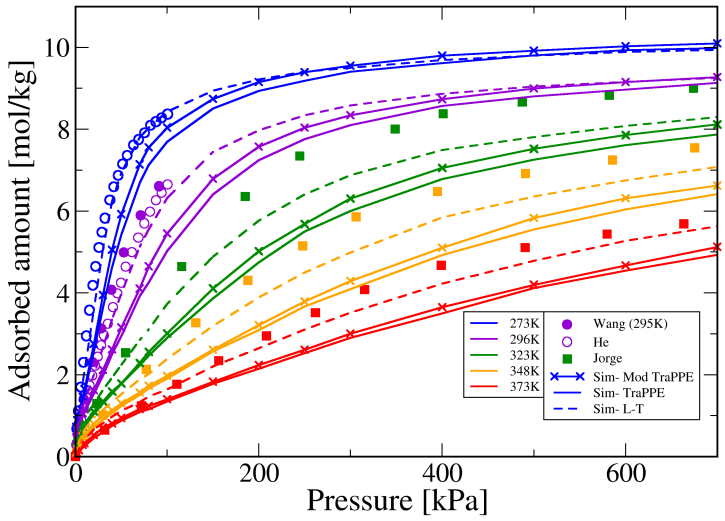


Figure 35: Ethane adsorption in HKUST-1. Experimental (symbols); Filled Squares- Jorge et al.[18], Filled Circles- Wang et al.[146] and Empty Circles- He et al.[37]. Simulations (Lines).

to be a sensible improvement. It should be noted however that the agreement is not perfect and performance drops at the higher temperature ranges. This is likely due to it being optimised for the He et al.[37] 296K data. The TraPPE and modified TraPPE forcefields both underestimate adsorption across the low pressure region of the isotherms, but converge with Triguero at high pressure. This suggests that the issue with these forcefields lies with the solid-fluid interaction rather than the packing at high coverage, which is dominated by fluid-fluid interactions. However, it should be noted that at no point is the underestimation of experiment as severe as seen in Chapter 3 for ethylene, when ignoring the CUS interaction in simulations.

This work also disagrees with the work of Jorge et al.[18] which showed the modified TraPPE simulations agreeing closely with the Jorge et al. experimental data, used in Figure 35. This is likely because those authors incorrectly used a 13 Å LJ cut-off, rather than the shifted 12 Å cut-off it was originally parameterised with. By not applying the shift cut, the whole energy profile will be deeper than expected. Furthermore, double-counting will occur in the interaction sphere be-

tween distances of 12-13 Å, which will not only by captured by the implicit long range correction used within the forcefield parameterisation, but now also explicitly captured with the larger cut-off. Both these issues likely lead to the higher adsorption, and therefore fortuitous better agreement, seen in the work of Jorge et al.[18] When the correct cut-off schemes are used, it is observed that the predictions of the TraPPE and modified TraPPE models are very similar.

Overall this illustrates the Luna-Triguero et al. forcefield as an improved model for ethane adsorption, at least in the case of HKUST-1. Further tests on other Cu-based MOFs should be performed in the future.

### 4.3.2 *Ethylene Single Component*

In Figure 36, it can be observed that both forcefields provide good agreement with experiment in the low pressure region for all temperature ranges. At the higher pressure regions of these isotherms this work's CUS model also shows good agreement. This could be expected from results in Chapter 4, although it is worth noting that this comparison now includes experimental isotherms at both higher temperatures and higher pressure ranges. This suggests that the CUS model proposed is capturing the binding mechanisms correctly at the CUS sites and therefore obtains the right packing of adsorbates within the MOF, highlighting the robust nature of this approach. The Luna-Triguero forcefield however shows very poor agreement with experiment at high pressure and has a lower saturation capacity for each temperature. This is likely due to the use of adjusted $\sigma$ LJ parameters, rather than explicitly accounting for the CUS interaction.

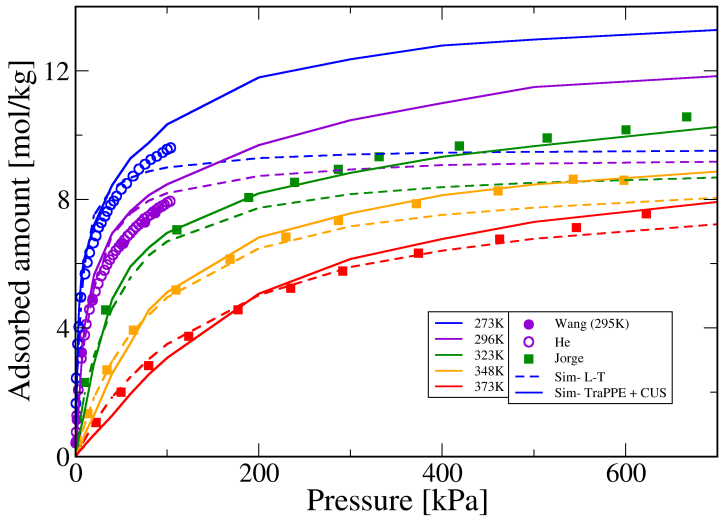


Figure 36: Ethylene adsorption in HKUST-1. Experimental (symbols); Filled Squares- Jorge et al.[18], Filled Circles- Wang et al.[146] and Empty Circles- He et al.[37]. Simulations (Lines).

As mentioned within the introduction, the highly attractive short range nature of the CUS interaction is hard to fully capture within the LJ potential without artificially increasing the interaction strength of nearby sites. In Figure 37, it can clearly be seen that the Luna-Triguero model's choice of increasing σ (shown in Table 10), relative to the starting point of the modified TraPPE, creates very strong adsorption sites away from the Cu-Cu dimers. The cost of this is, firstly, that a significant portion of the pore space near the Cu-Cu dimers is now repulsive, and also the CUS binding mechanism is not correctly captured. This leads to incorrect packing inside the MOF, which clearly becomes a issue when nearing capacity. It should be noted that the potential shown in Figure 37 is un-shifted potential, so a very slightly lower energy would be expected for 'Modified TraPPE' and 'Luna-Triguero' (which are shifted); this is unlikely to affect the above hypothesis however.

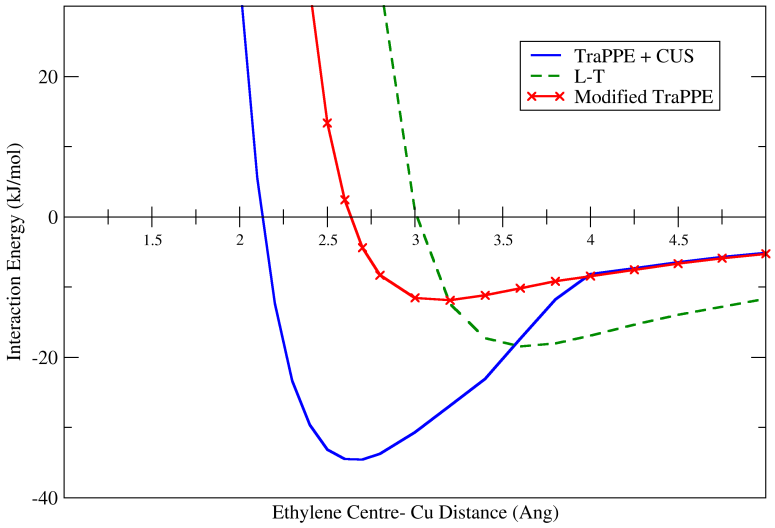


Figure 37: Monte Carlo simulated interaction energy (orientation minimum) for each model along the Cu-Cu vector of HKUST-1. The distance relates to the centre of the ethylene molecule to the nearest Cu atom.

This incorrect mechanism is confirmed through the orientation snapshot in Figure 38.a, which shows that there is little preference for the highly favourable CUS sites within the Luna-Triguero simulations, where the nearest $CH_2$ atom is 4.2 Å away from the copper. Contrastingly, the TraPPE simulations with this work's CUS model shows a clear preference for this site in Figure 38.b, the closest binding distance between the $\pi$ centre of the ethylene molecule and the copper is 2.6 Å, which is very close to the DFT minimum found in Chapter 3 of 2.61-2.63 Å and the orientation minimum identified in the Monte Carlo code, shown in Figure 37.

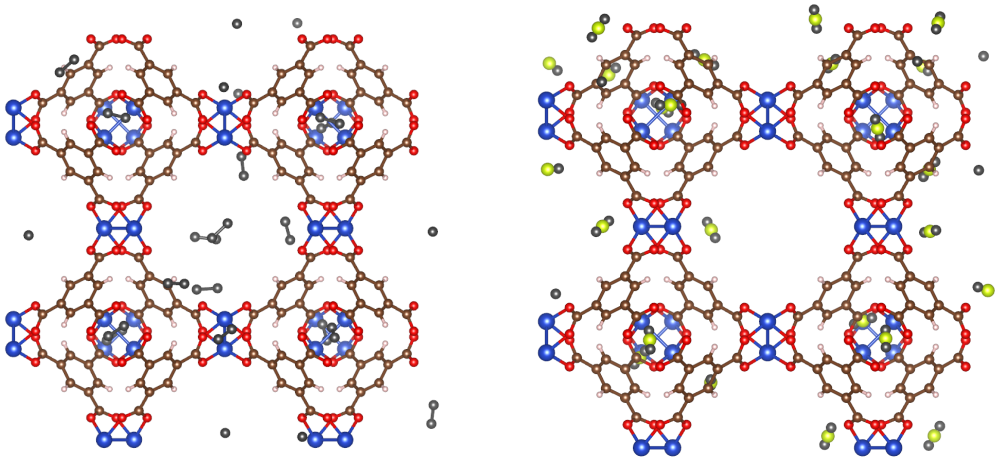

(a) Luna-Triguero (b) TraPPE

Figure 38: Diagram showing orientation snapshots of Ethylene simulations at 273K and 1kPa. Color code for atoms is: blue-copper, red-oxygen, brown-carbon, white-hydrogen, grey-$CH_2$ group and yellow- adsorbent CUS Site.

### 4.3.3 *Experimental- Powdered vs Pelleted HKUST-1*

The experimental binary data used later in this chapter was obtained from the work of Martins et al.[145], who also reported single-component isotherms on the same pelletised form of HKUST-1. In Figure 39, a comparison of Martins et al. single component experimental isotherms with those of Jorge et al.[18], for ethane and ethylene adsorption, can be seen. The higher temperature/pressure data of Jorge et al[18] and Martins et al.[145] disagree significantly, with Martins et al. showing a much lower uptake nearing saturation. It should be noted however that the Martins data has was only scaled up very slightly (see section 3.2.5) as the nitrogen pore volume in the powder form (0.836 $cm^3/g$)[145] was higher than that of the theoretically measured pore volume of HKUST-1 ($N_2$ GCMC simulation-0.8164$cm^3/g$) and the pore volume loss during pelleting was reported to be minimal (0.807$cm^3/g$).[145]

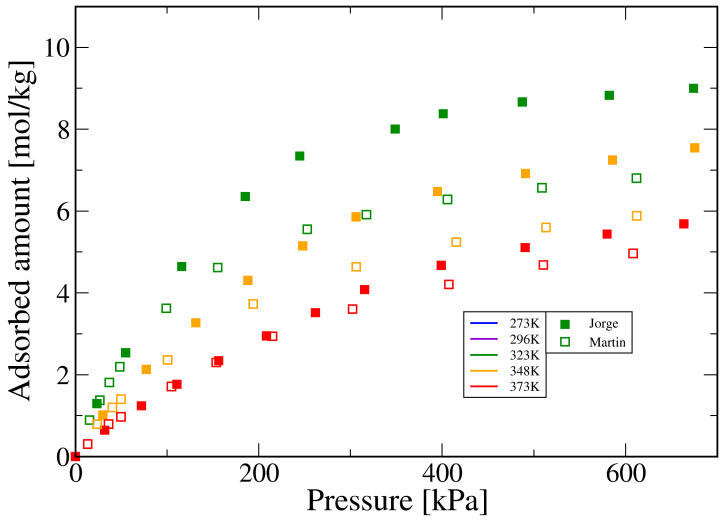


(a) Ethane

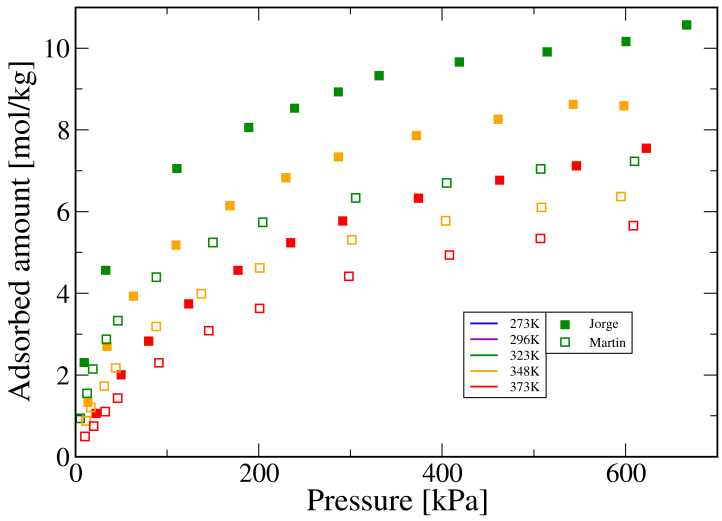


(b) Ethylene

Figure 39: Single component Ethane/Ethylene adsorption in HKUST-1. Experimental (symbols); Filled Squares- Jorge et al.[18], Empty Squares- Martins et al.[145]

One possible reason for the much lower adsorption seen for the Martins et al. data is a reduced pore volume from pelletisation. However, as shown above the nitrogen pore volume loss due to pelletisation can unlikely account for such a dra-

matic drop in adsorption, compared with the Jorge et al. dataset. Furthermore, the issue of reduced capacity could normally be accounted for by applying a consistent scaling factor across the isotherms (see Section 3.3.4). However, as shown in Figure 40 a consistent scaling factor could not be found to improve agreement with the Jorge et al. data across the different isotherms of ethane, where a scaling factor of 1.35 leads to relatively good agreement for 323K, but overestimation for 373K. This would become even more challenging when also trying to apply it to ethylene isotherms.

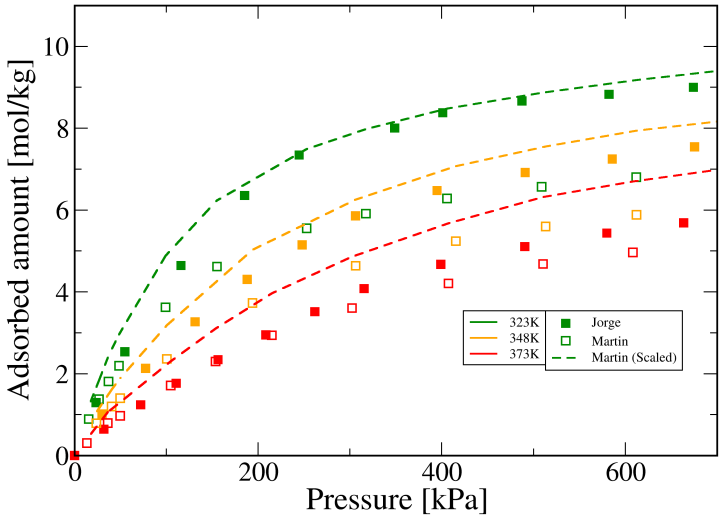


Figure 40: Single component Ethane adsorption in HKUST-1. Experimental (symbols); Filled Squares- Jorge et al.[18], Empty Squares- Martins et al.[145], dotted line- Martins et al.[145] scaled by factor of 1.35

Therefore the issue of adsorption reduction cannot solely be linked to pore volume loss. The fact that the nitrogen assessed pore volume is relatively unaffected by pelletisation while ethane/ethylene show significantly reduced adsorption hint towards a number of possible causes, such as MOF defects or kinetic effects. Nevertheless, it therefore does not make sense to compare simulation with experiment using total adsorbed amounts in the binary case. As such, the binary isotherms will be analysed using relative adsorbed amounts, which should limit the effect of the under-adsorption observed for pelletised HKUST-1 in the single component

isotherms. The effect of this can be tested on the pure component data, by comparing selectivity of Martins et al. and Jorge et al at 100kPa for each gas component (assumed equimolar) using Equation 47.

$$\textbf{Selectivity} = \frac{\eta_A/x_A}{\eta_B/x_b} = \frac{\eta_A/0.5}{\eta_B/0.5} = \frac{\eta_A}{\eta_B} \tag{47}$$

where

- $\eta$ Adsorbed amount
- $x$ Mol Fraction

Table 12: Selectivity based on single component adsorption of ethylene/ethane. Single component pressures are 100kPa.

| | Selectivity | |
|---|---|---|
| Temperature | Jorge et al.[18] | Martins et al.[145] |
| 323 K | 1.263 | 1.653 |
| 348 K | 1.443 | 1.889 |
| 373 K | 1.483 | 2.023 |

It should be noted that this is not a perfect solution; as shown in Table 12 the selectivity of Jorge et al.[18] still disagrees slightly with that of the Martins data, but it will at least limit the effect of this adsorption drop seen in pelleted HKUST-1.

### 4.3.4 *Ethylene/Ethane Competitive Binary Adsorption*

As expected from the work in Chapter 3, Figure 41 shows that standard forcefields (TraPPE) failing in the absence of a model explicitly accounting for CUS interactions. Indeed, in direct contradiction with experiment, it shows ethane as the preferred binding adsorbate over ethylene (indicated by opposite isotherm curvature). The remaining simulation models, 'TraPPE + CUS' and Luna-Triguero, predict the correct qualitative trend for binary adsorption.

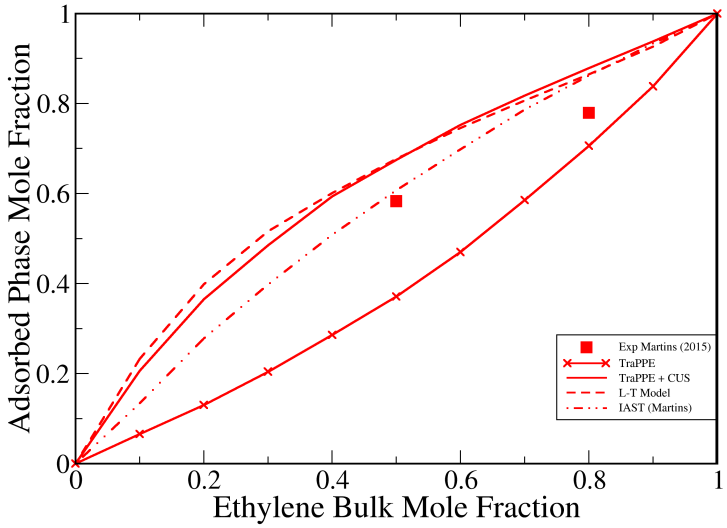


Figure 41: Adsorbed mole fraction of ethylene from binary ethane/ethylene mixtures in HKUST-1. Experimental (symbols)[145], Simulations (Lines) and Martins et al.[145] IAST (dashed-dotted Lines), conditions: 323K and 1.5bar.

For the Luna-Triguero forcefield, the performance appears equally as close as that of the combined 'TraPPE + CUS' model. This was initially surprising as they are very different approaches. However, when looking at the single component adsorption at 323K and 1.5 bar it can be seen that the models are actually showing relatively similar adsorbed amounts (see Figures 35 & 36). As such, the binary performance of the two models are the same. However, the performance of the Luna-Triguero forcefield at different conditions could likely be much worse. Firstly, it was shown that at higher pressures the inaccurate capturing of the CUS site for ethylene leads to poor saturation capacity agreement with experiment. As such, for ethylene/ethane binary adsorption the performance of the Luna-Triguero forcefield would likely become worse as the pressure, and therefore saturation level, increases. Additionally, the ethylene single component results show that the Luna-Triguero model has little preference for what should be the strongly attractive CUS sites. This can again be seen in Figure 42.a, where the Luna-Triguero model shows preferred adsorption away from the copper site, at a distance of above 3.5 Å, for ethylene. Conversely, Figure 42.b shows close CUS binding by the ethylene molecule in the case of the 'TraPPE + CUS model'. This could likely be-

come a much bigger issue when investigating binary adsorption of two gases that are both able to form coordination bonds with the CUS site. As the Luna-Triguero model does not capture ethylene strong binding to the CUS site it is unlikely that the competition for this binding site would be accurately captured, future work is required to confirm this hypothesis.

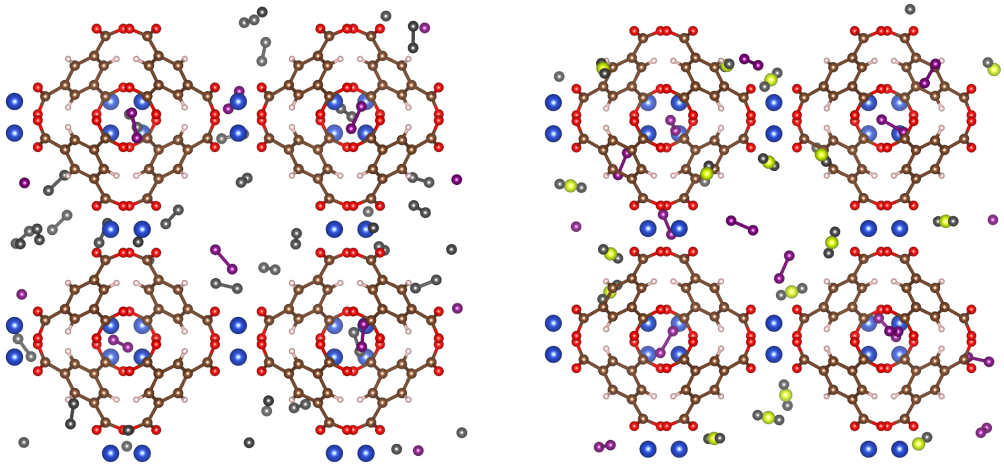

(a) Triguero (b) TraPPE

Figure 42: Diagram showing orientation snapshots of Ethylene/Ethane simulations at 373K and 1.5 bar. Color code for atoms is: blue-copper, red-oxygen, brown-carbon, white-hydrogen, purple-$CH_3$ group, grey-$CH_2$ group and yellow- adsorbent CUS Site.

Contrastingly, the 'TraPPE + CUS' model is likely slightly overestimating ethylene adsorbed amounts in the mixture, because it underestimates ethane single component adsorption (Figure 35). If the ethane forcefield were to be improved then this would likely lower the ethylene adsorbed fraction bringing it closer to experiment. The ethane Luna-Triguero forcefield, which performed better for ethane single component adsorption, could be used to achieve this, however this would require the LJ forcefield used for the ethylene to also be changed to match the shifted LJ cut-off scheme utilised by Luna-Triguero et al.[93] (see Methodology Section 4.2.1.2). A suitable future candidate for the ethylene LJ forcefield could be the Liu et al.[142] model, which Luna-Triguero et al. originally adapted for their binary predictions. This will first require a shifted potential to be implemented in

the software used for CUS isolation from the DFT energy profile.

In comparison with experiment, Figure 41 shows that simulations show a generally higher fraction of adsorbed ethylene than experiment, although agreement is improved versus the standard forcefield. However, the IAST predictions (taken from Martins et al.[145]) provide surprisingly good agreement with experiment for 0.5/0.5 ethylene/ethane composition, although agreement drops at 0.8/0.2 ethylene/ethane composition. As IAST makes assumptions regarding ideality, it would be expected to perform worse than the more accurate simulated models. For instance, Heinen et al.[101] suggests IAST could suffer from the strong binding effect of CUS sites on ideality assumptions, in which IAST has been shown to perform poorly when one adsorbate adsorbs much more strongly than the other component.[147] Additionally, one general issue that IAST is likely to suffer from is that it also assumes both components have equal access to the MOF pore space, when in fact for CUS-containing MOFs the vicinity of the CUS site is likely only accessible to ethylene. Therefore, IAST performance could be expected to worsen at lower temperatures and higher pressures, in which these assumptions would be more stringently tested.

The issues regarding the experimental data have already been discussed in terms of the pure component isotherms. It is still clearly evident in the binary data, as in Figure 41 the curvature suggested by the experimental data points does not appear to tend towards 1 adsorbed mole fraction when ethylene bulk mole fraction is at 1. This suggests inconsistency between the two data points. Furthermore, the conditions of the experiments are far from optimal for a comparison with simulations. Higher pressure and lower temperatures would give a much more stringent test of the believed IAST weaknesses, as well as probe the conditions in which the Luna-Triguero model performs the worst with respect to pure component experimental data (powder HKUST-1). Unfortunately, no experimental data at such conditions was found.

Overall, although the Triguero, 'TraPPE + CUS' and IAST methods all provide relatively similar performance, the pressure and temperature range of the experiment is insufficient to enable a proper comparison of these methods. This experimental data was able to give reasonable confirmation of the validity of the new CUS approach proposed in this work, but more complete and lower temperature adsorption isotherms are likely required to fully test all the available methods.

## 4.4 CONCLUSION

This chapter further expands upon the validation of the CUS ethylene model, seen in Chapter 3, to adsorption conditions of higher pressure and temperatures for HKUST-1. This study showed the CUS model performing well across all the experimental conditions. Furthermore, ethane simulations were performed and highlighted issues in previous simulations conducted in the work of Jorge et al.[18]. This finding suggests that improvements in the ethane pure component model is required, which will likely have an effect on binary behaviour. While not directly related to the CUS model, improvements in ethane forcefields may indirectly require new CUS parameters to be developed for ethylene in the future, to enable a consistent LJ cut-off scheme to be implemented.

For the first time, the CUS model was also tested and validated for binary adsorption of ethane/ethylene in HKUST-1 against experimental data. The agreement with the limited available experiment data was relatively good, although more experimental data is required for sufficient validation. This is, however, a key first step in the expansion of this model from investigating just single component applications to multi-component systems, such as competitive gas separation.

Furthermore, recent work by Luna-Triguero et al.[93] was investigated. The group proposed using single component adsorption isotherm optimised LJ parameters to predict the binary behaviour of ethane/ethylene in HKUST-1, without explicitly accounting for the CUS interaction. Although this approach appeared to perform equally as well as the proposed CUS model in the binary ethane/ethylene simulations, there are inherent risks within this approach, as the model began to break down at higher pressures in the case of pure component ethylene adsorption. This work highlighted the importance of correctly capturing the binding mechanisms behind adsorption isotherms. Although good agreement with experiment can be obtained for localised parts of an isotherm without them, the forcefield is unlikely to perform well outside the condition of parameterisation and furthermore may provide inaccurate results in complex simulations, such as for different binary adsorption mixtures.

# 5

# CARBON MONOXIDE AND NITROGEN ADSORPTION IN MOFS CONTAINING CUS

## 5.1 INTRODUCTION

Carbon monoxide is a gas present in a variety of industrial processes. It is commonly formed as an unwanted byproduct in incomplete combustion reactions for various oil and gas mixtures.[148] Therefore its removal from these streams is an important step in reducing pollution. Furthermore, there are various health concerns from exposure to the gas, including causing blood poisoning if inhaled at high enough concentrations and chronic effects from prolonged exposure, e.g neurological damage.[149] As such, proper disposal of the gas is of the utmost importance within industry.

Carbon monoxide can, however, also be a valuable feedstock. It is often produced from either coal gasification or steam reforming, in the form of synthesis gas mixtures (mainly made up of $H_2$:CO).[150] This is because for many industrial uses it is advantageous to have both gases present, such as in the industrial production of methanol, aliphatic alcohols and aldehydes; also synthesis gas is an important reducing agent within metal refining.[150][151] However, the correct ratio of $H_2$:CO must first be obtained for many of these applications. Jurgen et al.[150] describes a number of effective separation techniques used for $CO/H_2$, which is still an important area of ongoing research.[151]

For many applications, the use of pure carbon monoxide is required or industrially preferable; importantly, as a primary component within the production of acetic acids.[150] The separation of pure carbon monoxide from a gas mixture, such as synthesis gas, becomes much more demanding when attempting to remove any nitrogen components. This is because of the similar boiling points of car-

bon monoxide (≈191.5°C)[152] and nitrogen (≈-196°C)[152] making distillation separation costly and difficult. It should be noted that this is also an important separation for flue gases in which incomplete combustion has occurred, especially for plants within urban areas due to the safety concerns already discussed.

It will be this challenging gas separation, $CO/N_2$, which is the focus of this chapter. The difficulty of traditional distillation techniques for separation highlight it as a good candidate for Pressure Swing Adsorption (PSA) (see Chapter 1 for description), as was the case of ethane/ethylene separation discussed in Chapters 3 and 4.

As mentioned within Chapter 1, for PSA separation to be a viable alternative it requires a suitable adsorbent with sufficient selectivity for one of the gases. This chapter will aim again to investigate simulating adsorption in the presence of Coordinatively Unsaturated Sites (CUS) within Metal-Organic Frameworks (MOF) to exploit the binding strength that can be found within these unique sites. Unlike in Chapter 3, both CO and $N_2$ components will have orbitals with electron donating capabilities and therefore may require CUS parameters. Bordiga et al.[153] found experimentally for carbon monoxide that electrostatics alone was unable to account for the interaction with the copper sites in HKUST-1, and that a $\pi$-metal interaction was indeed often occurring. The same group also identified a similar case for nitrogen, however the interaction was very weak and required very low temperatures to study this binding.[153] Therefore, although both adsorbates may have a $\pi$ interaction with the copper site, the chemical differences in the adsorbates will expectedly lead to sufficiently different binding mechanism, and therefore binding strength, to enable a high MOF selectivity between the gases. It should be noted, however, that the exact electron donation sequence for certain gases, e.g. carbon monoxide, is still not completely agreed upon within the scientific community, and remains a controversial topic.[154] Within this work, DFT energies and orientations are used to tailor the Grand Canonical Monte Carlo (GCMC) simulations and, therefore, it is not necessary to know specific details about the electron donation mechanism for these simulations.

In literature, there is surprisingly little in terms of adsorption simulations of $CO/N_2$ mixtures in MOFs, especially on MOFs containing CUS.[155–159] Previous work by Karra et al.[156][159] using GCMC simulations to predict $CO/N_2$ separations in HKUST-1 without explicitly accounting for any CUS interaction appeared to obtain good agreement with experiment. However, more recent work by Martín-Calvo et al.[157] illustrated that using the same carbon monoxide model leads to underestimation by simulation in the low pressure region, in which solid-fluid interactions dominate. Martín-Calvo et al.[157], subsequently, developed a new model for CO which was fit to pure component vapour-liquid equilibrium. This new model, as well as a number of others, will first be investigated within this chapter's results section to better understand the performance of currently available carbon monoxide models.

The CUS model proposed in this thesis will then be expanded to carbon monoxide for the case of HKUST-1, to test if improvement against the currently available models can be found by explicitly accounting for the CUS interaction. As mentioned, as nitrogen is only weakly adsorbing to the CUS (at very low temperatures), it will also be individually assessed to evaluate if it will require CUS parameters to be derived for use in GCMC simulations. Apart from the immediate interest in $CO/N_2$ separations, carrying out this study should enable various other gas mixtures involving these gases to be potentially studied through GCMC simulations, which is especially advantageous due to how commonly they are found within industry.

An additional challenge for simulating these gases is that the effect of electrostatics can no longer be ignored (as was done for Ethane/Ethylene in Chapter 3). This is because the dipole of the carbon monoxide and the quadrupole of the nitrogen play an important role in interacting with the MOF.[156] This introduces complexity in the isolation of the CUS interaction, which will be elaborated upon within the Methodology section of this chapter. Finally, there will also be further refinement of existing steps within the CUS procedure, most notably the inclusion of dispersion within DFT calculations, which is an important step in reducing the number of approximations required for this approach (this step will also be vali-

dated against ethylene adsorption, to ensure consistency with results presented in chapter 3).

Overall, this section will outline a new procedure in the proposed CUS model to account for polar adsorbates that have a CUS interaction with a MOF's metal site. This step of extending the model to electrostatically relevant adsorbates is an important step in fully testing the transferability of this approach. This chapter will show that the model can indeed provide good quantitative agreement with experiment and can furthermore potentially be used as an important tool for predicting MOF selectivity for $CO/N_2$ gas mixtures.

## 5.2 METHODOLOGY

This section will outline the procedure to model the interaction of carbon monoxide and nitrogen with the HKUST-1 CUS. As in Chapter 3, the procedure comprises 5 key stages:

1. Quantum-mechanical (QM) calculations to obtain the interaction profile between the adsorbate and the CUS.
2. Isolation of the CUS contribution in the DFT profile.
3. Fitting the resulting profile to a modified Morse functional.
4. Including the new CUS interaction site in GCMC simulation.
5. Validating GCMC adsorption isotherms against experiment.

A comprehensive description of the concept behind each of these stages was provided within the Methodology of Chapter 3, this section will therefore focus on changes to the procedure, and assumes prior reading of Chapter 3.

### 5.2.1 *DFT calculations*

In Chapter 3, the PBE exchange-correlation functional was used and assumed to account for no dispersive interactions. However, as will be shown later, this approach does not work in the case of carbon monoxide and therefore an investigation was conducted into improving the exchange-correlation functional used and removing the assumption relating to dispersion. There are two commonly used approaches to account for dispersion interactions within DFT calculations, using an explicit correction term or implicitly accounting for it within the exchange correlation functional. The former approach can be successfully applied with functionals assumed to have little to no dispersive interaction and indeed combined with dispersion-including functionals, if they are thought not to fully capture the long and short range of the dispersive interaction.[160] However, the success of this approach is very dependent on the system being studied and can also involve partially scaling

the correction[160] when applied to exchange correlation functionals already partially capturing dispersion, which adds an empirical nature to the procedure. As such, the decision was made to focus on exchange-correlation functionals which implicitly account for dispersion. The VDW-DF2[161] was a good candidate as it has been successfully employed in forcefield development within MOFs[104], and also provided better agreement with MOF experimental isotherms than an approach utilising PBE-D2[162] corrected DFT calculations.[104] Additionally, the meta-GGA functional M06-L will be investigated as it has been shown to perform well in capturing the energies in the presence of transition metals[110, 163–165], making it ideally suited for CUS calculations. Alongside M06-L, the functional M06[166] will also be studied, as it is heavily based on the M06-L functional and recommended for use in organometallic chemistry.[166] As such, these exchange-correlation functionals were tested for carbon monoxide to see which provided the best agreement with experimental adsorption isotherms and then back-validated for ethylene, before the best functional was applied to nitrogen. Due to the limited number of exchange-correlation functionals available within CP2K software, several alternative procedures were considered:

- CP2K[106, 107] DFT software tested both the PBE and M06-L functionals.
- Quantum Espresso[167] DFT software tested the VDW-DF2 functional.
  (Carried out by collaborator José R. B. Gomes - University of Aveiro)
- Gaussian 09[168] DFT software tested the M06 functional.
  (Carried out by collaborator Jacek Osiński - University of Cambridge)

For the CP2K calculations the same DFT optimisation procedure was used as outlined in Chapter 3; however there were a number of technical improvements to the inputs used. In the DFT calculations for the PBE[108] and M06-L[169] exchange-correlation functionals the basis sets used for all but the Cu atoms were triple zeta plus polarization (TZVP) with PBE optimised Goedecker pseudopotentials.[107, 113, 114] These basis sets were unavailable for copper, and therefore the double zeta plus polarization (DZVP) sets were used. The more computationally expensive basis sets were used as it provided a more consistent Cu-Cu dimer distance

within M06-L optimization calculations. The energy cut-off selected for PBE was 600 Ry and M06-L was 800 Ry. As in Chapter 3, spin polarization was included. Furthermore, for all profile points a single point counterpoise correction[71] was used to account for basis set superposition error (BSSE), the origin of which is outlined in Chapter 2. The importance of BSSE for carbon monoxide calculations was much higher than that of the previous ethylene DFT calculations (see Chapter 3); for PBE optimization calculations at the minimum, the BSSE corrections for ethylene and carbon monoxide were $\approx$ 2 kJ/mol and $\approx$ 14 kJ/mol, respectively. The BSSE was estimated on a non-spin polarization system, however, due to technical difficulties with obtaining correct spin behavior in the BSSE calculations. This was because during BSSE calculations spin states would remain at zero for all atoms. Attempts to solve this included using both the 'multiplicity' keyword and directly controlling spin states through 'BS' keyword, but currently the issue remains unresolved. The author believes therefore that this correction will be slightly underestimated, but applying the correction will still be better than not accounting for BSSE at all.

For Quantum Espresso (QE)[167] the DFT calculations were performed with the periodic PWSCF v.5.3.0 code, employing the non-local correlation vdw-DF2 functional.[161] Again, the same DFT optimisation procedure was used as outlined in Chapter 3. Plane-wave basis sets were used to describe the valence electrons together with norm-conservative pseudopotentials within the Troullier-Martins approach for the core electrons.[170] It should be noted that as plane-wave basis sets are being used there will be no BSSE error present. The Kohn-Sham orbitals were expanded with 50 Ry cut-off for the kinetic energy and 200 Ry cut-off for the charge density. The first Brillouin zone integrations were performed with the Marzari-Vanderbilt smearing method at the gamma point. The convergence criteria where as follows: convergence threshold for self-consistency was $1x10^{-6}$ Ry (using a local-density-dependent Thomas-Fermi screening mixing mode with a factor of 0.7 for self consistency) and convergence on forces was $1x10^{-3}$ Ry/au.

For the Gaussian 09 DFT cluster calculations, the exchange-correlation functional used was the meta-GGA functional M06.[166] The basis sets used were 6-311++G** and a LanL2DZ pseudopotential for the Cu atoms. The BSSE corrections were ac-

counted for using the counterpoise method.[71] The energy convergence criteria was set at $10^{-6}$ Ha. As these DFT calculations were performed on a cluster, a very different optimisation procedure was used. Firstly, a relatively small cluster size was used for the CUS site of the HKUST-1 framework, $Cu_2(HCOO)_4$, shown in Figure 43. Fischer et al.[1] showed that for DFT cluster calculations of the HKUST-1 CUS site, the cluster size only has a small effect on binding energies within the system. Both the $Cu_2(HCOO)_4$ cluster and the adsorbate were optimised independently and then single point energy calculations were used to find the interaction energy at each position along the interaction profile (with the internal optimised positions remaining fixed).

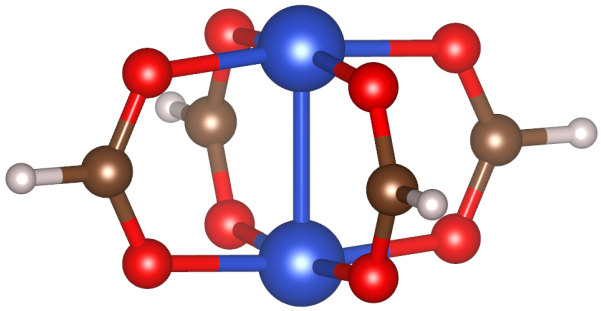

Figure 43: Illustration of DFT cluster used to represent the CUS Site in Gaussian calculations, Color code for atoms is: blue-copper, red-oxygen, brown-carbon and white-hydrogen.

The binding energies and distances at the energy minima are shown in Table 13 for each of the DFT calculations. The differences in binding energies with the CUS for carbon monoxide and nitrogen are promising indicators that the MOF will selectively adsorb carbon monoxide. It should be noted an increase in the DFT interaction energy from PBE in ethylene, -23.3 kJ/mol (see chapter 3), to the vdw-DF2 case, -36.4kJ/mol, confirming that dispersion is being accounted for in the latter case. Additionally, the binding energy of $\approx$ 29 kJ/mol for carbon monoxide in HKUST-1 found for Mo6 and VDW-DF2 is promising as it matches the experimental enthalpy of adsorption found by Rubeś et al. (29kJ/mol).[171] Mo6-L on the other hand is much more attractive than the experimental enthalpy of adsorption and the other dispersion-including functionals, indicating it may be overestimat-

ing the binding energy. The experimental enthalpy of adsorption is not an exact representation of the minimum DFT binding energy, as it is estimated at a finite temperature (whereas DFT is at absolute zero) and also averages over all sites at the specific adsorption coverage, but it still should give a reasonable estimation of the CUS interaction energy as long as the CUS is the dominant binding site at low adsorption coverage.

Table 13: DFT energy minima for each adsorbate using different DFT exchange-correlation functionals ($E_{xc}$).
(*B.D - binding distance relates to perceived binding point of the adsorbate with the Cu atoms. Carbon monoxide "C-Cu", ethylene "$\pi$ bond-Cu", nitrogen "nearest N-Cu")

| $E_{xc}$ | Adsorbate | Int. Energy (kJ/mol) | *B.D (Å) |
|---|---|---|---|
| PBE | Carbon Monoxide | -23.0 | 2.24 |
| vdw-DF2 | Carbon Monoxide | -28.8 | 2.32 |
| M06-L | Carbon Monoxide | -39.2 | 2.30 |
| M06 | Carbon Monoxide | -28.7 | 2.40 |
| PBE | Ethylene | -23.3 | 2.61 |
| vdw-DF2 | Ethylene | -36.4 | 2.65 |
| vdw-DF2 | Nitrogen | -16.3 | 2.65 |

In Figure 44, the full DFT binding energy profiles can be seen for each of the functionals, in the case of carbon monoxide. It is important to note that the M06-L profile is not only much deeper, but also is much less smooth than the rest of the profiles, leading to a very sharp minimum well. This may cause difficulties in the fitting procedure, as replicating such a sharp and disjointed well in the CUS model will be challenging.

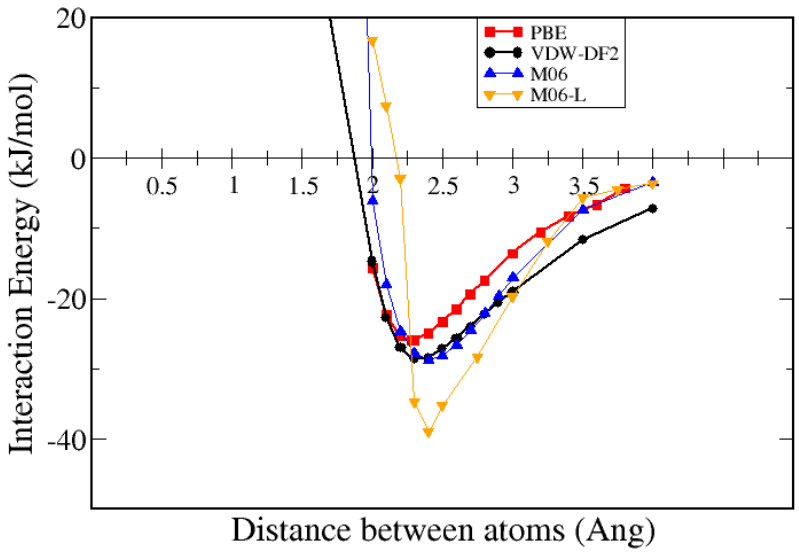


Figure 44: Diagram showing the DFT profiles of all exchange correlation functions, carbon monoxide adsorbing to the CUS site of HKUST-1. The binding point of the CO is the carbon

The binding orientations for the vdw-DF2 energy minima can be seen in Figure 45. The orientations shown for carbon monoxide and ethylene at the minimum energy are the same for all relevant exchange correlation functions. The binding orientations found for carbon monoxide (Figure 45.b) and nitrogen (Figure 45.c) agree closely with a relatively recent DFT study conducted by Supronowicz et al.[172] The aforementioned weaker binding of the nitrogen atom to the CUS can be better visualised in Figure 46. Whereas carbon monoxide and ethylene have the deep energy well indicative of the CUS interaction, the nitrogen binding energy profile is relatively flat in comparison, suggest the role of CUS sites for this adsorbate is minimal.

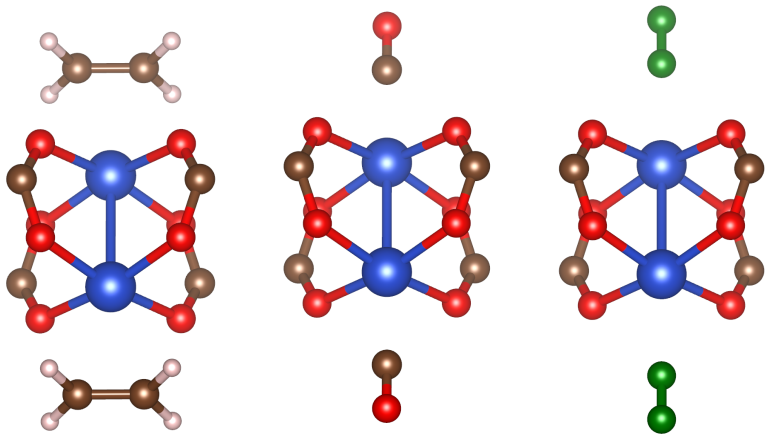

(a) Ethylene (b) Carbon Monoxide (c) Nitrogen

Figure 45: Diagram showing the binding orientations with respect to the adsorbates and the CUS at the DFT energy minimum. Color code for atoms is: blue-copper, red-oxygen, brown-carbon, white-hydrogen and green-nitrogen.

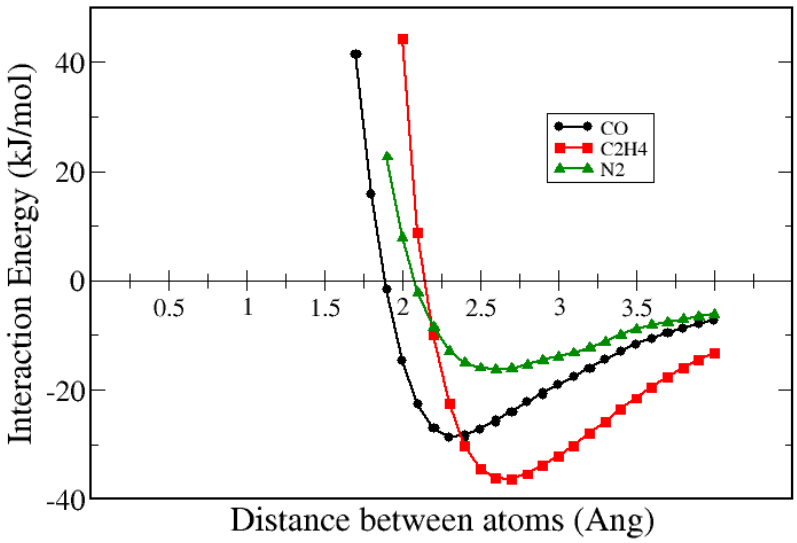


Figure 46: Diagram showing the VDW-DF2 DFT binding energies for each adsorbate at the CUS, with respect to the distance from the Cu atom. The binding point of the ethylene is the centre of the $\pi$ bond. The binding point of the CO and $N_2$ is the nearest binding atom (see Figure 45).

### 5.2.2 *Parameter fitting*

Once each interaction energy profile for the adsorbate with respect to the CUS has been determined, the CUS contribution must be isolated. The exact method for this isolation depends on the adsorbate and exchange correlation being used. Firstly, in the case of ethylene it is assumed that electrostatics do not play a significant role in adsorption in MOF frameworks (see Chapter 3).[18] This assumption is likely not valid for nitrogen and carbon monoxide, as discussed, and therefore the electrostatics must also be removed from the DFT profile. Furthermore, the PBE functional is assumed to not account for dispersion interactions and therefore only the repulsive contribution from van der Waals energy must be removed from the DFT profile. This is found by applying the Weeks-Chandler-Andersen (WCA) approximation[118, 119] on the LJ potential (shown in Section 3.2.2). In all other exchange correlation functionals investigated, the dispersion term should also be removed from the DFT profile. Therefore the dispersion and repulsion contribution can simply be removed together through the standard LJ potential, eliminating the need for the WCA approximation. The variations in the isolation forms for each of the systems can be seen in Equations 48 - 51.

**PBE: Ethylene**

$$U_{Cu-\pi}(r) = U_{DFT}(r) - \underbrace{U_{Rep}(r)}_{\text{WCA}} - \underbrace{U_{Disp}(r) - U_{Electro}(r)}_{\text{Zero}} \tag{48}$$

**PBE: Carbon Monoxide**

$$U_{Cu-\pi}(r) = U_{DFT}(r) - \underbrace{U_{Rep}(r)}_{\text{WCA}} - \underbrace{U_{Disp}(r)}_{\text{Zero}} - U_{Electro}(r) \tag{49}$$

**vdw-DF2: Ethylene**

$$U_{Cu-\pi}(r) = U_{DFT}(r) - \underbrace{U_{Rep}(r) - U_{Disp}(r)}_{\text{LJ Potential}} - \underbrace{U_{Electro}(r)}_{\text{Zero}} \tag{50}$$

**vdw-DF2/M06-l/M06: Carbon Monoxide & Nitrogen**

$$U_{Cu-\pi}(r) = U_{DFT}(r) - \underbrace{U_{Rep}(r) - U_{Disp}(r)}_{\text{LJ Potential}} - U_{Electro}(r) \tag{51}$$

For the isolation of the Cu-π interaction, all the other interaction terms must be known. This was achieved using the same in-house software as utilised within chapter 3, which calculated the Lennard-Jones potential profile along the Cu-Cu vector in a fully periodic structure, based on the classical models that will be used later in GCMC simulations. However, the code was adapted to also include electrostatics calculated using Ewald summations, also based on the point charges used later in GCMC simulations. When required, the Weeks-Chandler-Andersen (WCA) approximation[118, 119] was utilised to isolate the repulsive contribution in the LJ potential, as explained within Chapter 3.

The now isolated Cu-π energy profile represents the CUS specific attraction between each adsorbate and the CUS site of the MOF. However, the interaction site used within GCMC must be decided upon. In the case of ethylene, as explained in Chapter 3, an additional interaction site on the center of the ethylene double bond will be used, as it is the nearest interaction point with the copper site, see Figure 45.a. For carbon monoxide, the carbon atom is the nearest binding site to the copper, see Figure 45.b, and therefore will be the CUS interaction used within simulation. Finally, nitrogen is a slightly more complex case as it adsorbed directly onto the copper-copper vector, as shown in Figure 45.c. This means that one of the nitrogen atoms will be directly forming this CUS interaction. However, either of the nitrogen atoms could be the potential binding partner with the CUS. As such, both nitrogen atoms will be CUS interactions sites, but therefore an effective CUS interaction must be determined to account for the potential double-counting of the CUS interaction within the GCMC simulations. This effective interaction was achieved by assuming vertical adsorption and removing the non-binding nitrogen atom's interaction contribution from the binding nitrogen across the interaction profile; this is shown for one binding distance in Figure 48. The interaction sites can be better visualised in Figure 47.

The CUS interaction profile is then fitted to the same modified Morse potential as used in chapter 3, shown in equation 52.

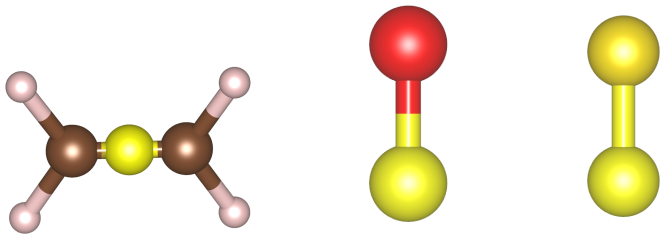

(a) Ethylene (b) Carbon Monoxide (c) Nitrogen

Figure 47: OMS site located on adsorbate molecules, color code for atoms is: red-oxygen, brown-carbon, white-hydrogen and yellow-CUS site.

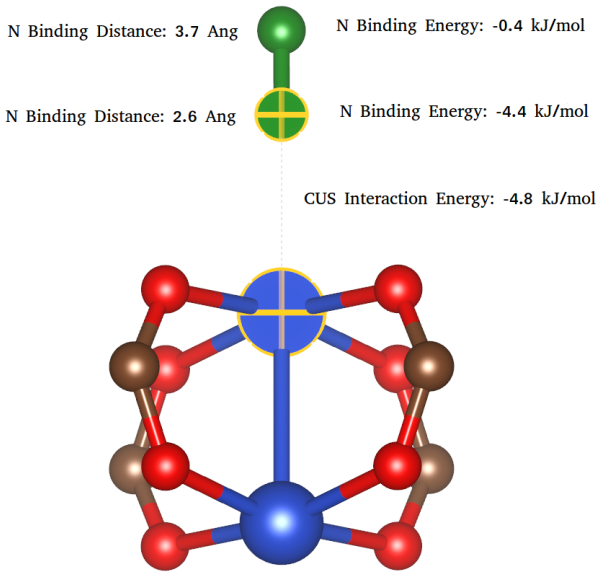


Figure 48: Illustration of nitrogen CUS fitting procedure for one binding distance. Color code for atoms is: blue-copper, red-oxygen, brown-carbon and Green-Nitrogen.

$$U_{function}(r) = D_o \cdot \left[ exp\left(\alpha\left(1 - \frac{r}{R_o}\right)\right) - 2 \cdot exp\left(\frac{\alpha}{2}\left(1 - \frac{r}{R_0}\right)\right)\right] - \left(\frac{A}{r}\right)^B \quad (52)$$

where

| | |
|---|---|
| $R_o$ | Distance of the minimum in the Morse potential (Å) |
| $D_o$ | Depth of this minimum (kJ/mol) |
| $\alpha$ | Flexibility of the fitting curve |
| $A$ / $B$ | Empirical fitting terms |

The CUS functional has the exact same cut-off scheme as that of Chapter 3.

$$U_{Cu-\pi}(r) = \begin{cases} 0 & r \leqslant \text{Lowcut} \\ U_{function}(r) & \text{Lowcut} < r \leqslant \text{Shiftcut} \\ U_{function}(r) \cdot \dfrac{(\text{Hicut} - r)}{(\text{Hicut} - \text{Shiftcut})} & \text{Shiftcut} < r \leqslant \text{Hicut} \\ 0 & \text{Hicut} < r \end{cases} \quad (53)$$

Table 14: CUS interaction cut-off scheme

| | |
|---|---|
| Lowcut | 1.8 Å |
| Shiftcut | 3.5 Å |
| Hicut | 4.0 Å |

### 5.2.3 *GCMC simulations*

All adsorption isotherms were obtained through GCMC simulations using the open source code Music.[120] The PMAP grid spacing selected was 0.15 Å, the same as in Chapter 3. For all GCMC simulations which did not include CUS interactions, cavity bias[52] based on the LJ potential maps was used for insertion and deletion trials. In the case of simulations explicitly including CUS interactions, insertion and deletion were done randomly. In addition to insertion and deletion trials, molecules were allowed to rotate and translate, using optimized maximum displacements. 600 000 000 steps were used for all non-CUS model GCMC simulations and 100 000 000 were used for all CUS model GCMC simulations. The first 50 % of steps were ignored to ensure equilibration, and the remaining steps were split into 20 equal blocks for error analysis. Pressure values were converted to fugacities for input into the simulation code using the Peng-Robinson equation of state[121]. The final absolute adsorbed amounts from the simulations were converted to excess, for comparison with experiment, using the Myers and Monson method.[61] Ewald summations[47] were applied in all solid-fluid interactions, while fluid-fluid interactions were described using the Wolf summation[49] (these techniques are described in Chapter 2).

Note: in the case of the Straub & Karplus model for CO (see Table 16) due to a memory allocation error within the Music version, bias insertion could not be used; to compensate for this, the number of steps was increased to 1 000 000 000.

#### 5.2.3.1 *LJ Forcefields/Electrostatics*

In MOF frameworks, the DREIDING forcefield[56] was used to describe the LJ interactions of all framework atoms apart from copper. The copper atoms are not present in DREIDING and therefore the Universal forcefield (UFF) was used.[55] The point charges used for the framework's electrostatic interaction were obtained from Castillo et al.[89], shown in Table 15/Figure 49, and have been used previously for carbon monoxide adsorption simulations in MOFs.[157] Additionally, point charges from the DDEC database[60, 173] will also be used for the HKUST-1 framework. This is to test the sensitivity of the CUS model towards point charge selection, in this case for carbon monoxide adsorption. As this will change the electrostatic interaction between the CUS and carbon monoxide, new DDEC-based CUS parameters will also be derived.

Table 15: Castillo[89] and DDEC[60, 173] point charges of framework atoms for HKUST-1, see Figure 49 for atom notation.

| Framework Atom | Castillo Point Charges (e) | DDEC Point Charges (e)Å |
|---|---|---|
| Copper | 1.248 | 0.928 |
| Oxygen | -0.624 | -0.564 |
| Carbon 1 | 0.494 | 0.679 |
| Carbon 2 | 0.130 | 0.030 |
| Carbon 3 | -0.156 | -0.163 |
| Hydrogen | 0.156 | 0.118 |

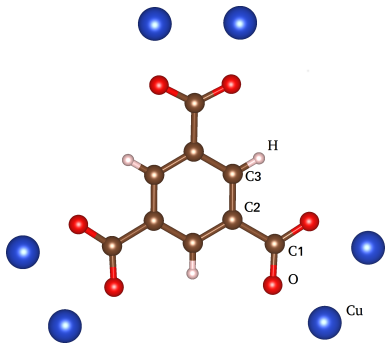


Figure 49: Illustration of naming system used for point charges of each framework atom in HKUST-1, see Table 15.

For ethylene, a united atom approach was used for each $CH_x$ group, with parameters taken from the TraPPE forcefield.[53, 54] The atomistic TraPPE forcefield was also used to describe nitrogen.[174] This forcefield was selected as it is fitted against vapour-liquid equilibrium helping to thus ensure that the gas-gas interactions are correctly captured, enabling the focus of this research to be solely on the gas-solid interaction (specifically CUS adsorption). Furthermore, this forcefield has been used previously within literature to describe adsorption in MOFs for both ethylene[86][18] and nitrogen.[175][156][159]

The TraPPE forcefield is not available for carbon monoxide. As such, several existing models will be tested for CO adsorption in MOFs to choose the most suitable model for further study. Martín-Calvo et al.[157] carried out a comprehensive comparison of CO models for their ability to predict vapor-liquid equilibrium, and we will use their study as a basis for our assessment. In particular, they examined four different models, UFF[55], Straub and Karplus[176] (S&K), Piper et al.[177], and their own model, which we will call M-C model[157]. Of these, the UFF and M-C models showed the best agreement with liquid-vapor equilibrium data.[157] The S&K model uses the same geometry as M-C, but the different parameters lead to a much poorer performance in vapor-liquid equilibrium. The Piper et al.[177] model was not investigated further here, as it uses a complex 4-site point charge geometry, making it challenging for later combination with our CUS model, and also performed poorly in liquid-vapor equilibrium simulations. The LJ parameters and point charges for all CO models can be found in Table 16 and a visual representation of the site layouts is shown in Figure 50.

Cross-species LJ interactions were estimated using the standard Lorentz-Berthelot combining rules, and this included all solid-fluid interactions. The exception is a model proposed by Martín-Calvo et al.[157] in which the LJ $\epsilon$ values for the CO-MOF interaction were increased by a factor of 1.2 and some of the mixed sigma values were very slightly altered in order to match CO adsorption in HKUST-1 at 298K. The CO-MOF parameters for this modified M-C model are shown in Table 17 together with parameters obtained with the standard combining rules to enable direct comparison. Here we will compare the performance of these models for pre-

dicting adsorption of CO in both HKUST-1 and MOF-5[178], or IRMOF-1, as an example of a widely studied MOF without CUS. In particular, we will assess the performance of the models against high pressure experimental adsorption data of CO in HKUST-1, which was not available at the time of the Martín-Calvo study.

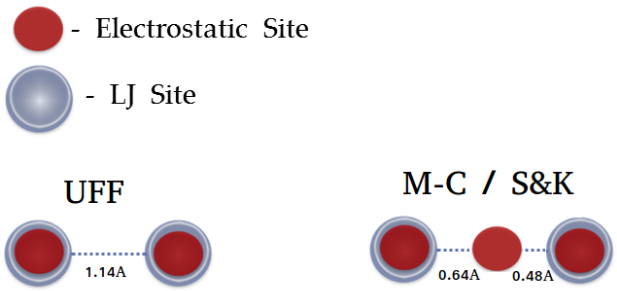


Figure 50: Illustration of LJ and electrostatic sites in each carbon monoxide model studied here.

Table 16: Carbon monoxide models

| Model | Atom | σ (Å) | $\epsilon/k_b$ (K) | charge (e) | Position (Å) |
|---|---|---|---|---|---|
| UFF[155] | C | 3.43 | 52.888 | 0.107 | 0 |
| | O | 3.12 | 30.219 | -0.107 | 1.140 |
| M-C[157] | C | 3.636 | 16.141 | -0.2424 | 0 |
| | O | 2.979 | 98.014 | -0.2744 | 1.128 |
| | Dummy | - | - | 0.5168 | 0.6443 |
| Straub & | C | 3.83 | 13.18 | -0.75 | 0 |
| Karplus | O | 3.12 | 80.06 | -0.85 | 1.128 |
| (S & K)[176] | Dummy | - | - | 1.6 | 0.6443 |

Table 17: Mixed LJ parameters for original and modified M-C carbon monoxide model.[157]

| | | M-C Original | | M-C Modified | |
|---|---|---|---|---|---|
| Adsorbate Atom | Framework Atom | $\sigma$ (Å) | $\epsilon/k_b$ (K) | $\sigma$ (Å) | $\epsilon$ (K) |
| Carbon | Copper | 3.3750 | 6.3700 | 3.386 | 7.6500 |
| | Oxygen | 3.3345 | 27.881 | 3.344 | 33.468 |
| | Carbon | 3.5560 | 27.794 | 3.564 | 33.353 |
| | Hydrogen | 3.2410 | 11.112 | 3.254 | 13.334 |
| Oxygen | Copper | 3.0465 | 15.697 | 3.0465 | 18.852 |
| | Oxygen | 3.0060 | 68.705 | 3.0045 | 82.471 |
| | Carbon | 3.2275 | 68.491 | 3.2245 | 82.189 |
| | Hydrogen | 2.9125 | 27.383 | 2.9145 | 32.859 |

#### 5.2.3.2 *CUS Functional*

The CUS parameters derived from the fitting procedure for each of the studied exchange correlation functionals are presented in Table 18.

Table 18: CUS parameters obtained from DFT fitting to Equations 48 - 51. All CUS parameters were found using Castillo et al.[89] framework point charges, unless stated as DDEC.[60, 173]

| $E_{xc}$ | Adsorbate | $R_o$ (Å) | $D_o$ (kJ/mol) | $\alpha$ | A | B |
|---|---|---|---|---|---|---|
| PBE | CO | 2.7712 | 10.34 | 9.0376 | 3.3025 | 10.1583 |
| M06-L | CO | 2.566 | 21.95 | 15.36 | 2.873 | 17.045 |
| M06 | CO | 2.6348 | 10.955 | 11.276 | 3.1155 | 11.6115 |
| vdw-DF2 | CO | 2.75 | 9.829 | 8.25 | 3.243 | 10.1068 |
| vdw-DF2 | CO (DDEC) | 2.6307 | 12.395 | 8.9123 | 3.157 | 10.772 |
| vdw-DF2 | $C_2H_4$ | 3.0374 | 11.2 | 8.489 | 3.8246 | 9.2875 |
| vdw-DF2 | $N_2$ | 2.832 | 2.6417 | 13.2 | 2.819 | 13.65 |

## 5.3 RESULTS AND DISCUSSION

This results section begins by testing the performance of existing models for predicting CO adsorption in HKUST-1 and IRMOF-1, Figure 51/54.

### 5.3.1 *Existing CO Models*

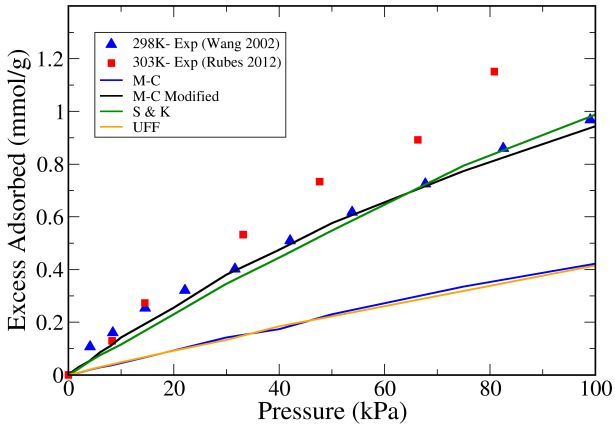


(a) Low Pressure

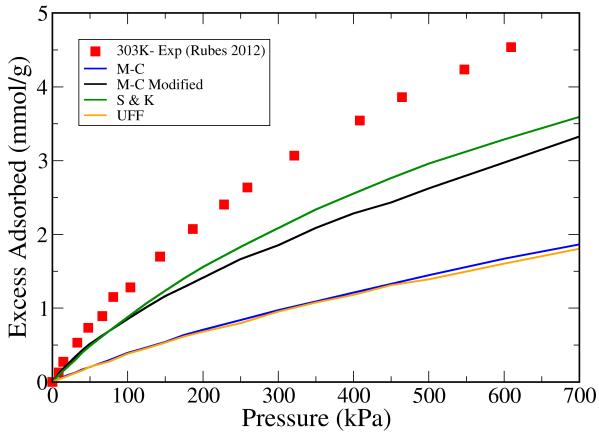


(b) High Pressure

Figure 51: Simulated (lines) and experimental (symbols), CO adsorption isotherms in HKUST-1. a) Simulations performed at 298K for comparison with Wang et al.[146]; b) Simulations performed at 303K for comparison with Rubes et al.[171]

In agreement with Martín-Calvo et al.[157], both the UFF and M-C models largely underestimate adsorption at all conditions when compared with both sets of HKUST-1 experimental data (Figure 51). As both models replicate vapor-liquid equilibrium very well[157], this is unlikely due to the gas-gas interactions and is caused instead by not accounting for specific interactions with the CUS of the MOF, which these forcefields were not designed to describe. Unsurprisingly, the modified M-C model performs well in comparison with experimental adsorption at 298K (Figure 51.a), since the scaling parameters for CO-MOF interactions were designed to fit this particular dataset. The S&K model also showed good agreement with experiment at 298K, but for entirely different reasons. The good performance of the M-C model can be explained by the much higher solid-fluid LJ parameters being used, which uniformly enhance interactions between CO and all the framework atoms. With the S&K model, instead, adsorption is mainly enhanced by the much higher values of the CO point charges (see Table 16), leading to stronger electrostatic interactions with the framework than observed with the UFF and original M-C models. Indeed, Figure 52 shows that along the Cu-Cu vector of the HKUST-1 CUS the electrostatic interaction energy is much more favourable than for the M-C models. The price of these enhanced electrostatics is a much poorer performance in vapor-liquid equilibrium simulations.[157] Therefore, error cancellation between gas-gas and gas-solid interactions is the most likely explanation for the rather fortuitous adsorption agreement at 298 K in the case of the S&K model.

Although the modified M-C model closely agrees with the Wang experimental data set[146], to which it was fitted, it is not able to match the isotherm of Rubes et al.[171] at 303 K (Figure 51.b). In fact, Figure 51.a clearly shows that the Wang et al. isotherm has a lower adsorbed amount than that of the more recent work of Rubes et al., despite the latter corresponding to a slightly higher temperature (303 K). This is true even after scaling for pore volume differences (see Section 3.2.5). This suggests that the Wang et al. data were likely obtained on a lower quality sample of HKUST-1, and highlights the pitfalls of fitting forcefield parameters to match a restricted set of experimental data without subsequent validation.[78] In this particular case, the modified M-C model is observed to fail when predicting

adsorption outside the fitting conditions of the model.

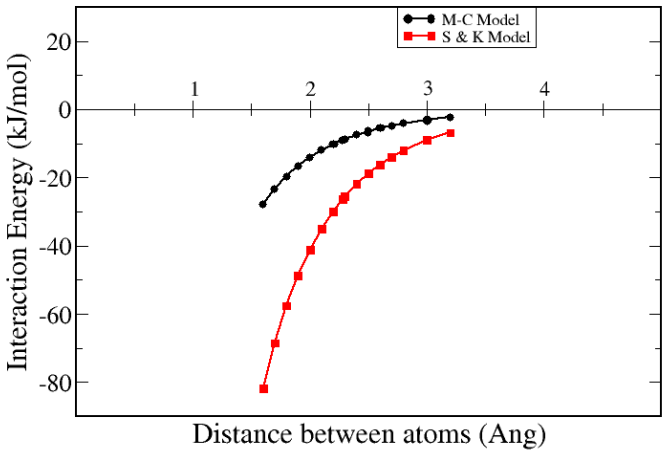


Figure 52: Electrostatic interaction energy at orientation binding minimum along the Cu-Cu vector of the CUS. Distance is from OC–Cu.

Figure 51.b shows that none of the available models is able to capture the correct high-pressure saturation behavior. This is likely because no model is able to describe the binding mechanism at the CUS correctly. Indeed, none of the investigated models showed a strong preference for binding at the CUS, which DFT calculations (Table 13) identified as a highly attractive site. Furthermore, even when interactions between CO and the CUS were observed, the opposite orientation was observed when compared with the DFT-optimized geometry. Figure 53 shows a simulation snapshot obtained at 298K and 7 bar using the modified M-C model, highlighting the area around the Cu paddlewheel unit. Compared to the DFT geometry from Figure 45, the binding distance is much larger ($\approx$ 4Å) and, more importantly, it is the oxygen atom that is more closely binding with the CUS, instead of the carbon atom as observed in DFT. As shown in Table 16 and 17, almost all models have oxygen with a higher $\epsilon$ value than that of carbon (the exception being UFF) and also a more negative point charge, making the oxygen's LJ potential and electrostatics both more attracted to the Cu atoms (which have been assigned a positive point charge). It should also be noted that the configuration shown in Figure 53 is actually quite rare in all simulations with the standard models. This

analysis confirms that the standard models are not capturing the correct adsorption mechanism of CO at the CUS, which hinders their ability to accurately predict adsorption isotherms over a wide range of pressures.

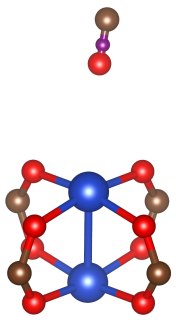

Figure 53: Cropped Snapshot at 700kPa and 303K for the modified M-C model simulations, carbon monoxide adsorbing to HKUST-1. Color code for atoms is: blue-copper, red-oxygen, brown-carbon and purple- dummy electrostatic site.

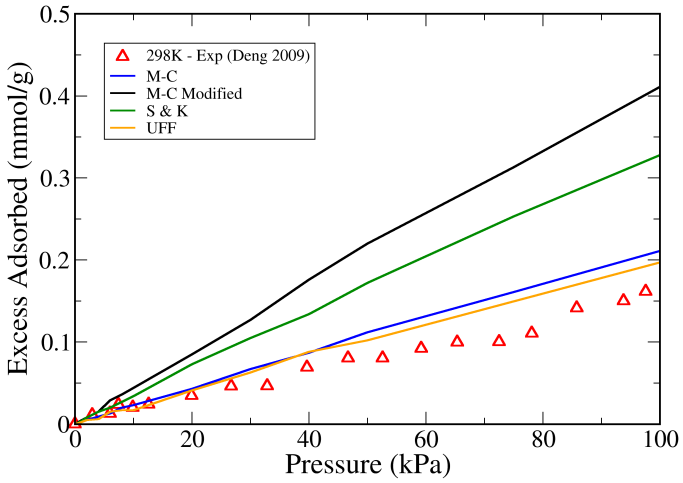


Figure 54: Simulated (lines) and experimental[179] (points open-Pv Unscaled) carbon monoxide adsorption isotherms in IRMOF-1.

As illustrated in Figure 54, in the case of IRMOF-1, in which no CUS are present, a very different picture can be seen. The UFF and M-C model now provide relatively good agreement with experiment across the full isotherm. This, in conjunction with the HKUST-1 results, further reinforces the idea that these models are capturing the gas-gas interaction correctly, as well as the standard van der Waals and electrostatic interactions with the solid. They fail when CUS are present in the MOFs, which is to be expected, and this makes both of them good candidates for combining with the CUS model proposed here. The failure of the modified M-C model shows that although strengthening the LJ parameters improves agreement in HKUST-1 at low pressure, the parameters cannot be transferred to IRMOF-1. This raises doubts about the possibility of generally transferring this model to other MOFs (both with and without CUS) without further parameter fitting. In the case of the S&K model, the large overestimation observed could be caused by the overestimation of the electrostatic interaction. In HKUST-1, this was not observed as the stronger electrostatics compensated for the unaccounted CUS interaction. In the case of IRMOF-1, though, there are no CUS present and therefore no error cancellation takes place.

Based on the above results, we are now in a position to select the most appropriate CO model to be combined with the QM-based CUS interaction. When looking at the performance of the UFF and M-C models, both replicate vapor-liquid equilibrium well[157] and also both appear to capture the van der Waals and electrostatic interaction with IRMOF-1 correctly. The M-C model was selected for our CUS approach as it better replicated the experimental dipole moment of the carbon monoxide molecule, with the M-C model exactly matching the dipole moment of 0.112 D, while UFF is significantly higher at 0.58 D.[157] Indeed in Appendix A.2, it is shown that the drastically different UFF fluid-fluid point charges causes issues in the CUS fitting procedure, leading to poorer adsorption isotherm performance.

### 5.3.2 *CUS Model- CO Adsorption*

Section 5.3.1 clearly shows that none of the existing CO models can fully describe the adsorption isotherm for HKUST-1, and that enhancing electrostatics or the LJ potentials fails to adequately correct for this. Furthermore, these techniques also lose backwards compatibility for non-CUS containing MOFs, in this case IRMOF-1. Therefore this section will investigate if isotherm agreement can be improved by explicitly accounting for the CUS interaction using the transferable CUS model proposed within this work.

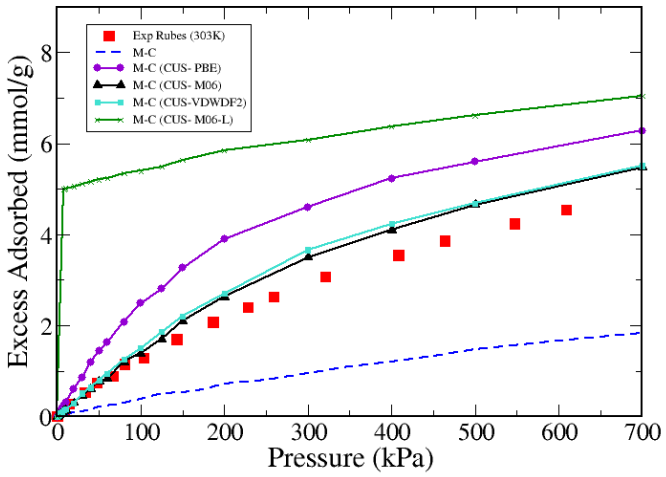


Figure 55: CUS model simulated (lines), non-CUS model simulated (dotted lines) and experimental[171] (points) carbon monoxide adsorption isotherms in HKUST-1

When the previous CUS model approach is used (Chapter 3), by applying the PBE exchange correlation functional and assuming dispersion in DFT calculations is zero, simulations significantly overestimate adsorption (Figure 55). This was initially surprising, as in Chapter 3 this procedure was successful in the case of ethylene adsorption within this same MOF. To gain a better understanding into why this method now fails it is important to look into the assumptions being used. There are two main assumptions to this approach, one is that the DFT calculation contains no dispersion contribution and secondly that the Weeks-Chandler-Andersen (WCA) approximation is adequate to isolate the repulsive contribution

from the LJ potential. If the issue lay with the first assumption it would mean both ethylene and carbon monoxide simulations should likely fail, which is not the case. One of the main differences between these two CUS adsorptions is their relative binding distance to the copper: ethylene $\approx$ 2.6 Å and carbon monoxide $\approx$ 2.24 Å. Therefore, the effect of the repulsive contribution at the binding minimum in the case of carbon monoxide is much greater than that of ethylene. It could be concluded therefore that the issue with this method more likely lies with using the WCA approximation to determine repulsion. Thankfully, both of these assumptions can be removed together by using more advanced exchange-correlation functionals which account for dispersion, thereby removing the assumption of no dispersion within DFT calculations and also no longer requiring to decouple repulsion from the LJ potential.

As discussed in the Methodology section (5.2) there are several ways to account for dispersion in DFT calculations. In this work, it has been decided to investigate exchange correlation functionals that implicitly account for dispersion, namely M06 (cluster), M06-L (periodic) and VDW-DF2 (periodic), and determine which provide the best isotherm agreement with experiment. However, it should be noted that there are a number of other variables within these DFT calculations that could affect binding, and therefore to solely attribute performance of each of the DFT derived CUS models based on the $E_{xc}$ functional used would be incorrect.

The M06-L functional can clearly be seen to lead to overestimated adsorption in Figure 55. A higher adsorption was expected due to the much higher binding CUS energy found for this exchange correlation functional compared to M06 and VDW-DF2; in Table 13 it is shown to have a higher binding energy by $\approx$ -10 kJ/mol at the minimum. However, this could not account for such unphysical behaviour, with almost immediate saturation at low pressure. The main issue arose in the fitting procedure; as shown in Figure 44, the M06-L functional led to a very unsmooth and sharp CUS binding energy profile. This in turn led to a poor CUS model fit and overestimation of the CUS interaction at the close binding distances (especially between 2-2.2 Å). The cause of the poor DFT profile is hard to immediately identify, it could be the functional itself but could also lie within the software or DFT

procedure (see Methodology section for BSSE correction issues). Identifying the exact cause, or causes, of the poor performance of M06-L will require extensive investigation but is currently outside the scope of this work. This does, however, demonstrate that the CUS model is sensitive to the quality of the full DFT energy profile, rather than just at the minimum.

As can be seen in Figure 55, the CUS models derived from M06 and VDW-DF2 dispersion-including $E_{xc}$ provided much better agreement with experiment throughout the entire pressure region. Furthermore, in Figure 56 it can be seen that the carbon (adsorbate) is now the preferred binding partner to the copper site. The illustration is for VDW-DF2 simulation, but similar binding orientation was seen for M06. Correctly capturing the binding mechanism now provides better agreement at the higher pressure region. This is very promising and suggests that either of these $E_{xc}$ could be used in this CUS method. As mentioned in Chapter 3, using periodic DFT calculations is more consistent with the CUS approach proposed, due to the periodic nature of the CUS isolation procedure. As such, the decision was made to proceed with only using VDW-DF2 calculations for dispersion-including energy profiles. Although M06 calculation could be rerun periodically this would be a duplication of effort when both functionals appear to work equally well. To further validate this new approach, it will also be applied to the previously studied ethylene adsorption in HKUST-1. These new ethylene parameters will also be transferred to a different copper paddlewheel MOF (PCN-16) to ensure the CUS model's transferability demonstrated in Chapter 3 is maintained.

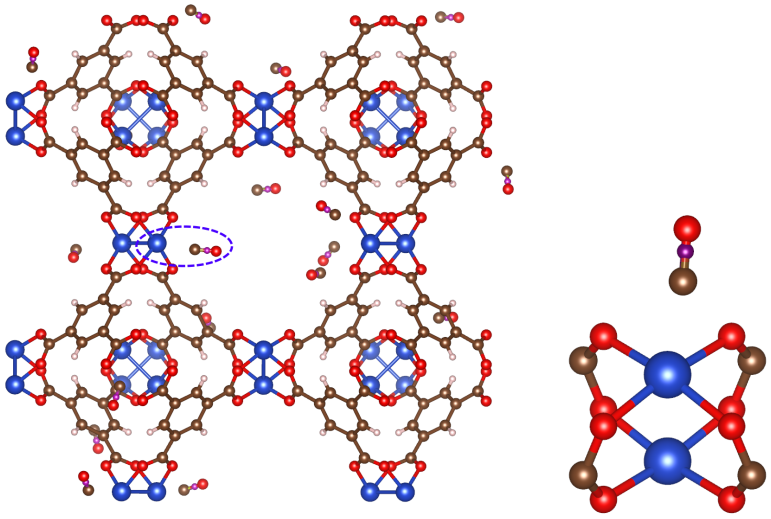

(a) Unit Cell (b) Cropped

Figure 56: Diagram showing orientation snapshota of VDW-DF2 CUS model carbon monoxide simulations at 303K and 100kPa. Color code for atoms is: blue-copper, red-oxygen, brown-carbon, white-hydrogen, purple- dummy electrostatic site

### 5.3.3 *CUS Model -Effect of Framework Point Charges*

In Figure 57, it can be seen that there is only a very small difference in simulated adsorption using DDEC framework point charges, compared with the Castillo et al.[89] point charges. This is very promising and shows that CUS model performance is not overly dependent on the point charges selected. Indeed, it can be seen in Figure 58, that the total interaction energy (CUS + LJ + Electrostatics) is almost identical for the two sets of point charges at the CUS site. This is in spite of a average 2kJ/mol electrostatic difference along the CUS profile between the two point charge sets, which is compensated by a slightly adjusted CUS interaction strength. This suggests that the difference in isotherms from the two simulations is caused by the point charges at the non-CUS binding sites.

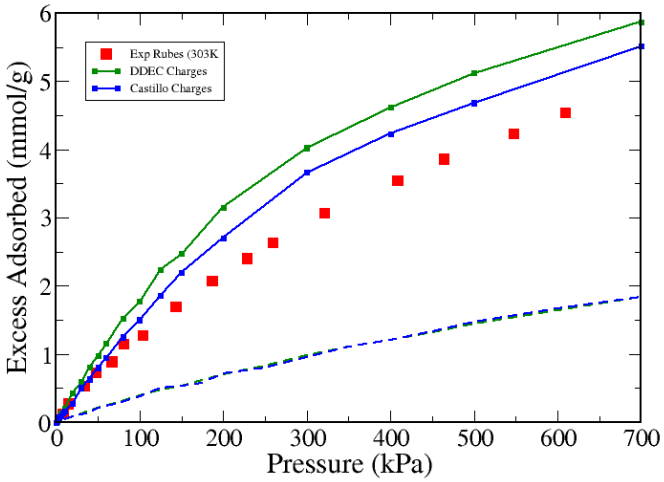


Figure 57: VDW-DF2 CUS model simulated (lines), non-CUS model simulated (dashed lines) and experimental[171] (points) carbon monoxide adsorption isotherms in HKUST-1

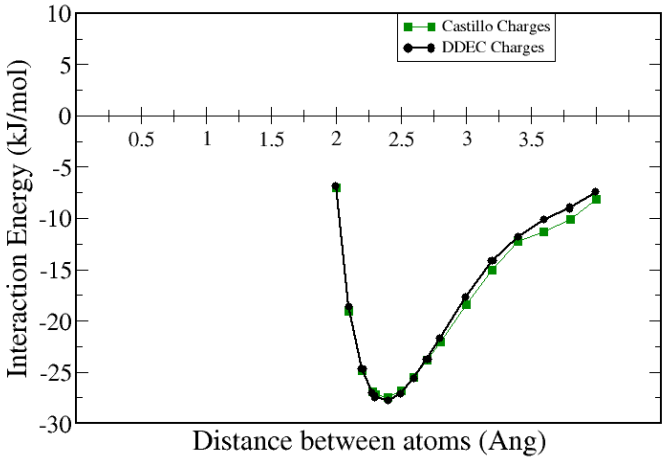


Figure 58: VDW-DF2 CUS model interaction energy (CUS + LJ + Electrostatics) along CUS profile for carbon monoxide in HKUST-1. Two sets of point charges used; Castillo et al.[89] and DDEC database[60, 173]

### 5.3.4 *CUS Model- Ethylene Adsorption*

As shown in Figure 59, the effect of the new procedure, utilising the VDW-DF2 $E_{xc}$, on ethylene adsorption is minimal. There is only a very slight difference in adsorption with respect to the old PBE-based approach (see Chapter 3) in the low pressure region, while at high coverage the two methods give identical adsorption, likely due to the similar binding minima found in DFT: PBE- 2.61Å and VDW-DF2- 2.65Å. This demonstrates a transferability of this new approach across different adsorbates, for both polar and non-polar adsorbates. It is therefore recommended that this chapter's dispersion-including methodology be used hence forth when applying this CUS model. This will also remove the additional complexity of decoupling repulsion from the LJ potential, as done within Chapter 3

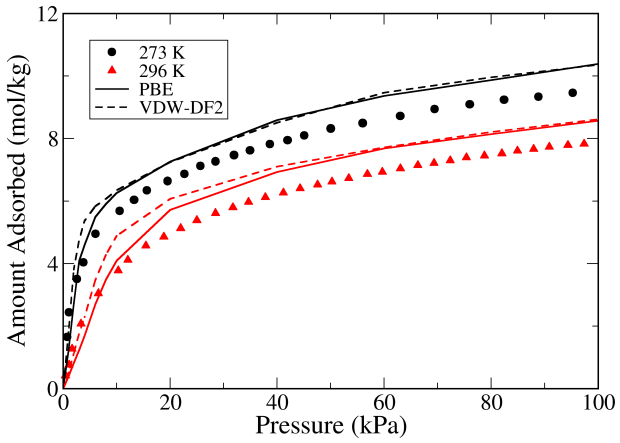


Figure 59: CUS model simulations (lines) and experimental[37] (symbols) ethylene adsorption in HKUST-1

Furthermore, using the exact same HKUST-1 parameters for the CUS in PCN-16 (Figure 60) again shows insignificant differences with the previous work in Chapter 3. This highlights that the new procedure retains the same transferability demonstrated for copper paddlewheel MOFs. This also indicates, at least for the TraPPE ethylene parameters, that the CUS isolation step is working well. If the CUS parameters were capturing not only the CUS interaction, but also correcting for some slight underestimation in dispersion from the standard forcefield, the parameters would likely not transfer so well to the PCN-16 MOF.

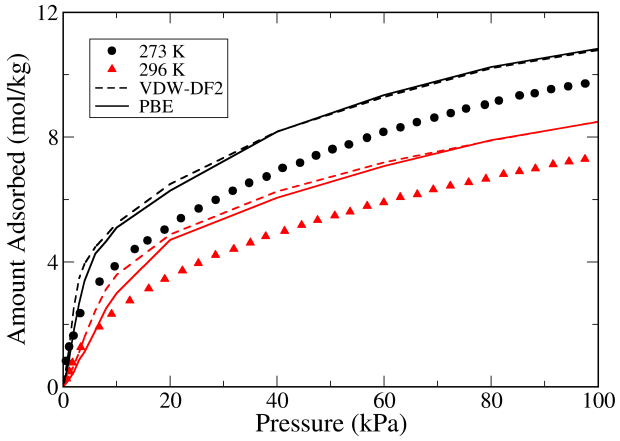


Figure 60: CUS model simulations (lines) and experimental[37] (symbols) ethylene adsorption in PCN-16

### 5.3.5 *CUS Model- Nitrogen Adsorption*

In Figure 61, it can be seen that the standard TraPPE forcefield agrees relatively well with the experimental isotherm for nitrogen. This could be because the role of CUS sites is small for adsorption at these conditions. In the work of Bordiga et al.[153] it was shown to be a very weak binding site. Conversely, the implementation of the CUS model worsens agreement with experiment, leading to higher overestimation by the simulation. This is surprising as the DFT calculation is meant to capture the correct CUS interaction energy; if the site is unfavorable at these conditions then the GCMC simulations should reflect this. The experimental data used is from the group of Rother et al.[180]; the pore volume reported was for C300 Basolite, 0.82 g/cm$^3$, which was higher than that of the theoretically calculated nitrogen pore volume of 0.8164g/cm$^3$. As such, the experimental adsorption points remain unscaled for defects and lost pore space from an imperfect crystal. Additional experimental isotherms are required for comparison before any firm conclusion can be drawn about the nitrogen CUS model.

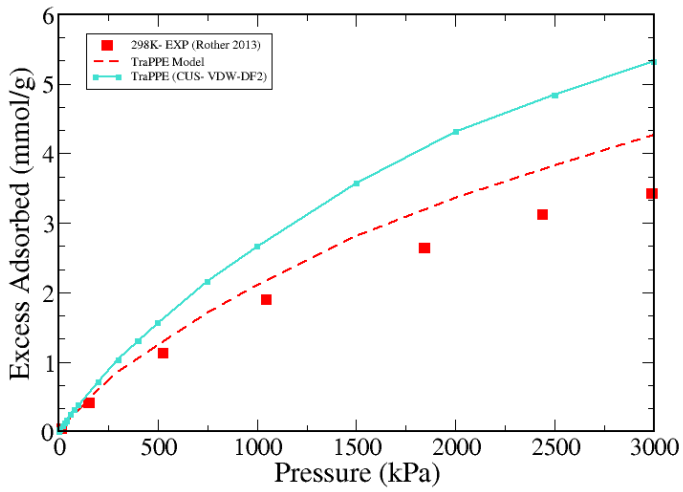


Figure 61: CUS model simulated (lines), non-CUS model simulated (dotted lines) and unscaled experimental[180] (points) Nitrogen adsorption isotherms in HKUST-1

### 5.3.6 *Conclusion*

In this paper we have shown that existing carbon monoxide models are unsuitable for capturing the orbital behaviour of CUS-containing MOFs, and subsequently agree poorly with experimental adsorption isotherms for HKUST-1. Furthermore, attempts to improve agreement through adjustment of LJ parameters fail to find agreement across the full isotherm, and also lose backward compatibility with non-CUS containing MOFs.

This work builds upon our group's CUS model, which has been shown to be transferable across adsorbates (ethylene to propylene)[18] and adsorbents (copper paddlewheel MOFs)[58]. It has now been successfully expanded to electrostatically relevant adsorbates (carbon monoxide), and through removal of dispersion-related assumptions, agrees closely with experiment across the full isotherm. Importantly, it also captures the correct binding mechanism at the CUS, which will likely be required for correct simulation of competitive binary adsorption. The updated procedure was also back-validated successfully against previous work[58], to ensure that transferability was indeed retained. Overall, this work highlights the robust nature of this CUS approach and its flexibility across different adsorbent and adsorbate types, making it an ideal candidate for use in large-scale computational screening of MOFs for gas separations.

Additionally, however, in the validation of the CUS approach for nitrogen adsorption, simulation was seen to overestimate adsorption in comparison with experiment. It was concluded that more experimental datasets were required for comparison before any conclusion relating to the CUS model performance could be drawn for the case of nitrogen.

# 6

# CHARACTERISING A NEW AND FLEXIBLE MOF FOR USE IN CARBON CAPTURE

## 6.1 INTRODUCTION

This short chapter will be based on an ongoing collaboration with McAnally and co-workers. The work is, as of yet, unfinished and therefore this chapter will discuss the current progress of the study.

McAnally[181] looked into synthesising a new material from an existing family of cubic based MOFs (which will be referred to as the SIFSIX family in this chapter).[182–186] The repeating units of these MOFs are generally made up of a single metal site (often copper), and two ligand types. The first ligand is organic and hydrocarbon based, with a nitrogen atom linking the metal site to the organic linker. The second ligand is inorganic, silicon centered surrounded by six fluorine atoms (hence the name SIFSIX). An example of a repeating unit for a MOF from this family ($Cu(bpy\text{-}2)_2SiF_6$) can be seen in Figure 62.a. Additionally in Figure 62.b, the general topology highlights the cubic nature of these MOFs.

There are various different forms of the SIFSIX family that can be obtained from altering the metal site or organic linker. For example $Zn(pyz)_2SiF_6$, which has zinc metal sites instead of copper, as well as a much shorter organic linker.[183] In some cases these MOF variations can take interpenetrated forms. $Cu(dpa)_2SiF_6$ has a similar form to $Cu(bpy\text{-}2)_2SiF_6$ but with a triple bond at the centre of the organic linker, see Figure 63.a. This MOF can take both interpenetrated and non-interpenetrated forms; the interpenetrated structure can be seen in Figure 63.b (See Chapter 2 for explanation on interpenetration).

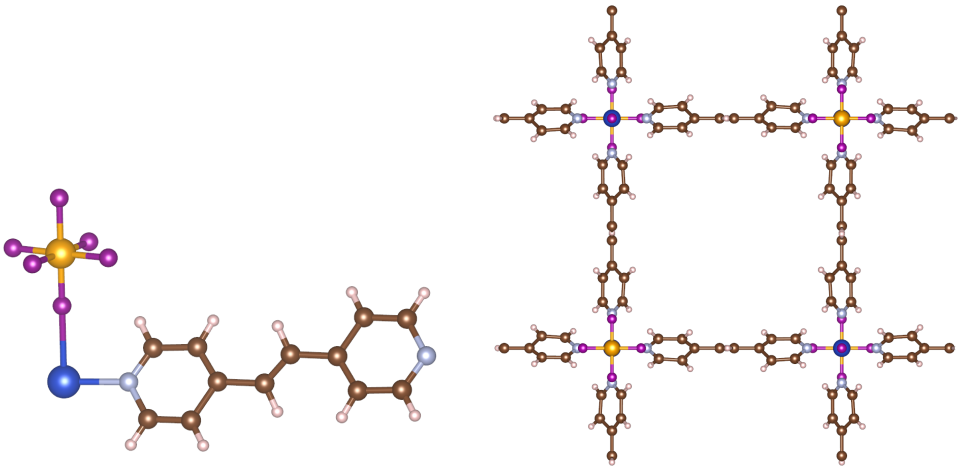

(a) Linker (b) Topology

Figure 62: Diagram showing the linker (a) and the unit cell topology (b) of Cu(bpy-2)$_2$(SiF$_6$)$_n$. Color code for atoms is: dark blue-copper, brown-carbon, white-hydrogen, light blue-nitrogen, purple-Fluorine and orange-Silicon.[182]

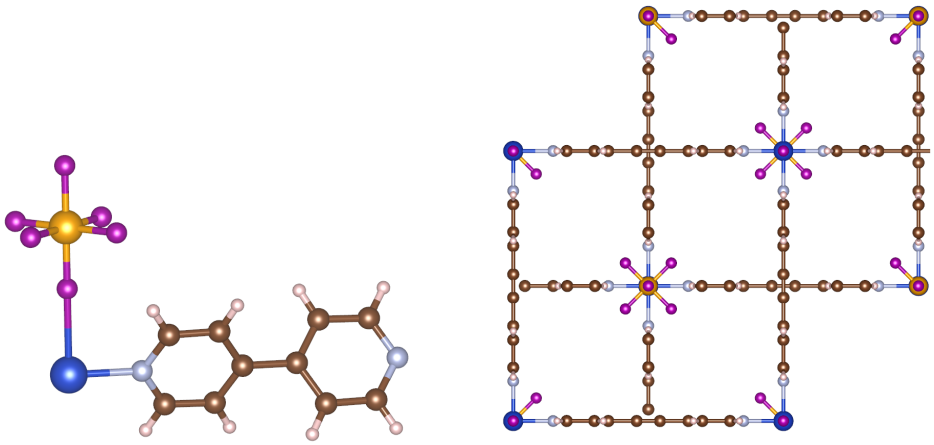

(a) Linker (b) Topology

Figure 63: Diagram showing the linker (a) and the unit cell topology (b) of Cu(dpa)$_2$SiF$_6$. Color code for atoms is: dark blue-copper, brown-carbon, white-hydrogen, light blue-nitrogen, purple-Fluorine and orange-Silicon.[182]

The SIFSIX family MOFs have been shown to have excellent binding sites for carbon dioxide capture.[182, 183] This is primarily derived from the fluorine binding sites, which have strong electrostatic properties and therefore favour binding to the polar carbon dioxide adsorbate.[183] As carbon capture was the focus of the work by McAnally et al.[181], the group looked into further enhancing the performance of the MOF by elongating the organic hydrocarbon linker. This was in the hope of increasing pore volume and therefore improving MOF capacity, as high capacity is a very desirable property for applications in gas capture/storage.

McAnally created the new MOF [Cu(bpetha)$_2$(SiF$_6$)$_n$][181] using an adapted method from the work of Noro et al.[185] for the synthesis of Cu(bpetha)$_2$(PF$_2$) (not of the SIFSIX family). The aim was to swap the phosphorus-based linker for the silicon-based linker shown in Figure 62. The silicon-based unit should be favoured as it will have more $F^{\delta-}$ atoms in the inorganic linker, creating more potential binding sites for the $C^{\delta+}$ of carbon dioxide, while also retaining the saturated hydrocarbon linker (bpetha). Essentially, this should create the same MOF as in Figure 62, but with a saturated $CH_2$-$CH_2$ hydrocarbon linker centre, rather than CH=CH. This saturated C-C bond will be longer than the C=C bond, thereby increasing the linker length. The new MOF's repeating unit can be seen in Figure 64.

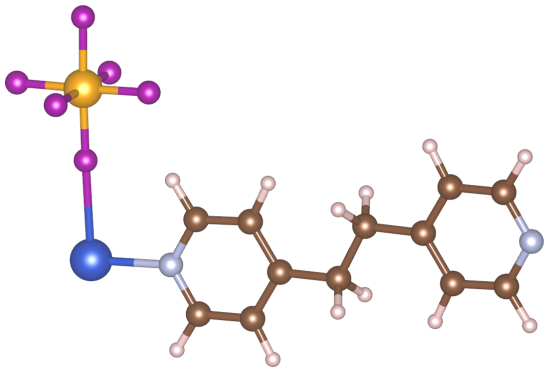

Figure 64: New MOF, Cu(bpetha)$_2$(SiF$_6$)$_n$. Color code for atoms is: dark blue-copper, brown-carbon, white-hydrogen, light blue-nitrogen, purple-fluorine and orange-silicon.[181]

The new MOF was synthesised, but displayed unusual adsorption properties in the case of nitrogen and carbon dioxide single component adsorption. Therefore modeling was used in an attempt to understand this unusual adsorption behaviour observed experimentally and provide insight into the MOF's structure. This will be achieved using a combination of DFT calculations and structural analysis through the software poreblazer[76] (used within Chapter 3) .

This is a novel application of modeling, as throughout this work experiment has mainly been used as a validation tool for simulations. However, this will be the first time in this thesis that simulations will be applied to a MOF structure not well understood experimentally. Overall this chapter will demonstrate the value of harnessing experimental and simulated investigations in unison, leading to a more fundamental understanding into the behaviour of these unique adsorbents.

## 6.2 METHODOLOGY

### 6.2.1 *DFT calculations*

In this work the DFT calculations were run using the open source software CP2K[106, 107]. This software uses periodic boundary conditions, enabling the full MOF structure to be accounted for. CP2K uses a combination of basis sets from Gaussian-type orbitals and a plane-wave basis; for an explanation of these basis set types see Section 2.2.5.[106, 107] The exchange-correlation functional used was PBE[108], as it has been found to give a reasonable prediction of MOF structure through geometry optimization DFT studies.[187, 188] The basis sets used for all atoms were double zeta plus polarization (DZVP) with PBE optimised Goedecker pseudopotentials[107, 113, 114]. The energy cut-off selected was 500 Ry, with convergence checked by using higher values for selected cases, and the calculations used Γ point sampling. Furthermore, spin polarization was accounted for in all DFT calculations.

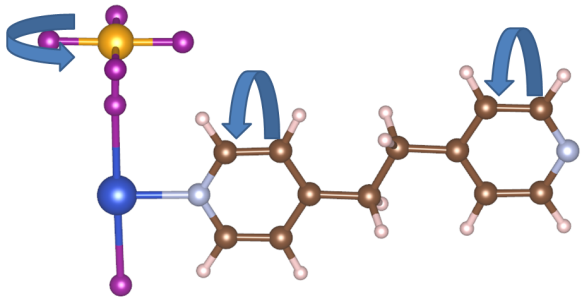

Figure 65: DFT Starting Configurations for $Cu(bpetha)_2(SiF_6)_n$. Color code for atoms is: dark blue-copper, brown-carbon, white-hydrogen, light blue-nitrogen, purple-fluorine and orange-silicon. Top fluorine atom moved below copper for image clarity. Arrows indicates groups that are able to rotate.[181]

The starting point for the new MOF structure $Cu(bpetha)_2(SiF_6)_n$ (Figure 64), was based on the $Cu(bpy\text{-}2)_2(SiF_6)_n$ structure (Figure 62).[182] Two hydrogen atoms were added to the carbons at the centre of the organic-ligand, to covert

them from unsaturated $sp^2$ carbons to saturated $sp^3$ carbons. During geometry optimisation DFT calculations, cell optimisation was also enabled to account for any change in cell size that adding the hydrogen atoms would cause.

As in previous studies[184], the effect of the rotation of the hydrocarbon rings and of the fluorine groups on DFT optimisation was investigated (see Figure 65). Two initial fluorine arrangements were tested, with fluorine atoms in alignment and out of alignment with the organic linkers(see Figure 66). Three main aromatic ring positions were investigated, firstly in vertical position (Figure 67.a), slanted parallel (Figure 67.b) and slanted opposite (Figure 67.c). This made a total of 6 starting configurations which were tested.

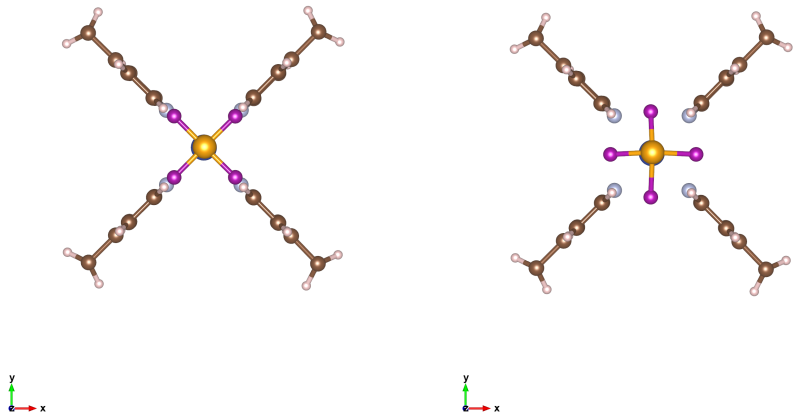

(a) Aligned (b) Unaligned

Figure 66: View from above of DFT Starting Configurations for Fluorine atoms in $Cu(bpetha)_2(SiF_6)_n$. Color code for atoms is: dark blue-copper, brown-carbon, white-hydrogen,, light blue-nitrogen, purple-fluorine and orange-silicon. Cu-N bonds were excluded for image clarity

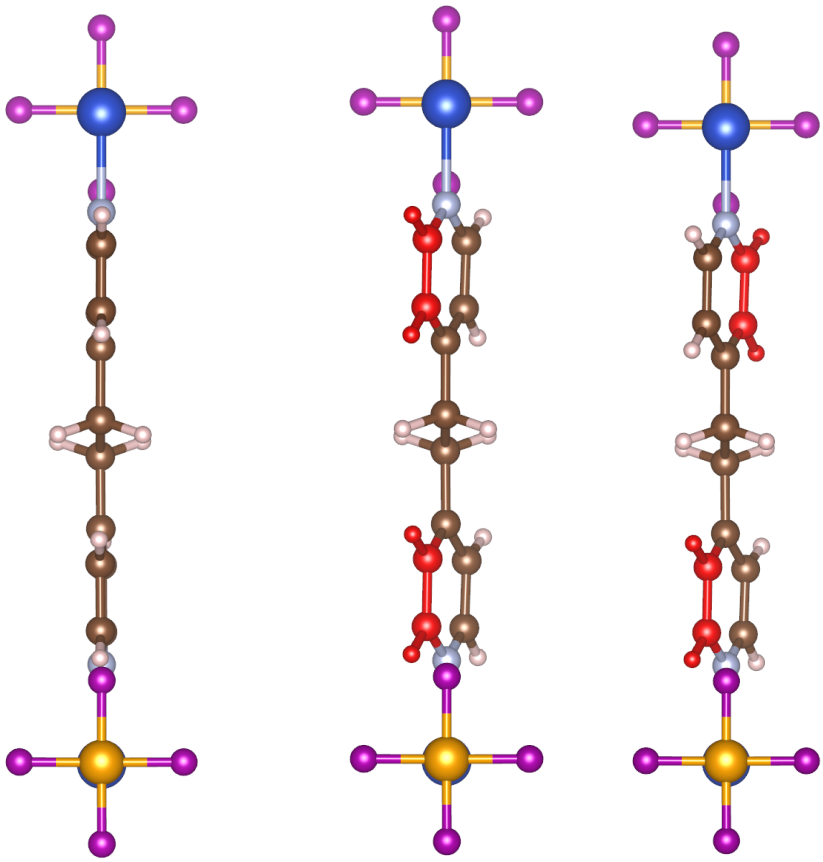

(a) Vertical (b) Slanted Parallel (c) Slanted Opposite

Figure 67: DFT Starting Configurations for Hydrocarbon rings in $Cu(bpetha)_2(SiF_6)_n$. Color code for atoms is: dark blue-copper, brown-carbon, white-hydrogen, light blue-nitrogen, purple-fluorine, orange-silicon and red- atoms on same vertical plane .

### 6.2.2 *Structural Analysis*

The open source software poreblazer[76] was used in assessing the structural properties of the optimised MOF cells; a description of the software can be found in Section 2.3. The main property being investigated was the accessible surface area.

## 6.3 RESULTS

### 6.3.1 *Flexibility*

In the work of McAnally et al.[181], a step was observed in the adsorption of carbon dioxide in the new MOF, $Cu(bpetha)_2SiF_6$, at 298K (Figure 68). This step was also observed at other conditions for carbon dioxide, confirming it was not an experimental anomaly. This points towards a flexibility phenomenon occurring within the MOF during adsorption, as the structure may be opening slightly to enable further adsorption.[15] Interestingly, at the same temperature (298K) the $Cu(bpy\text{-}2)_2(SiF_6)_n$ MOF (with a c=c bond in the linker) showed no adsorption step within the isotherm. This suggests that it is the introduction of the saturated hydrocarbon linker that is causing this flexibility.

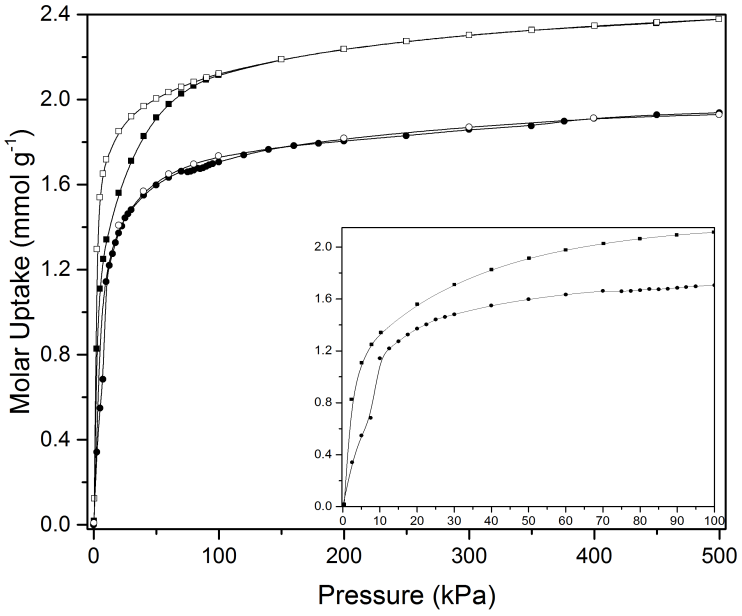


Figure 68: Experimental Adsorption[181] of $CO_2$ in $[Cu(bpetha)_2(SiF_6)_n]$. Squares-273K circles-298K. Black-adsorption, white-desorption. Inset shows detail at low pressure.

The cell/geometry DFT calculations for the 6 initial starting configurations (see Section 6.2.1) found two main geometries, shown in figure 69 (the exact energies can be seen in Table 19). Figure 69.a shows the slightly more favourable of the two configurations, which holds a similar orientation to that of the starting point MOF, $Cu(bpy\text{-}2)_2(SiF_6)_n$, albeit with a slightly elongated unit cell (organic linker plane increasing by $\approx 0.3$Å in both axis). This was the desired result of the experiment, using the increased saturated carbon bond length to increase the repeated unit length and thereby the pore space. However, a second minimum was found, shown in Figure 69.b, in which the centre C-C bond can be observed to twist, leading to a more condensed unit cell than that of the un-collapsed configuration. As there was a new configuration found, the exact same 6 ring configurations were also tested for the collapsed structure (starting point being the most favourable collapsed structure identified).

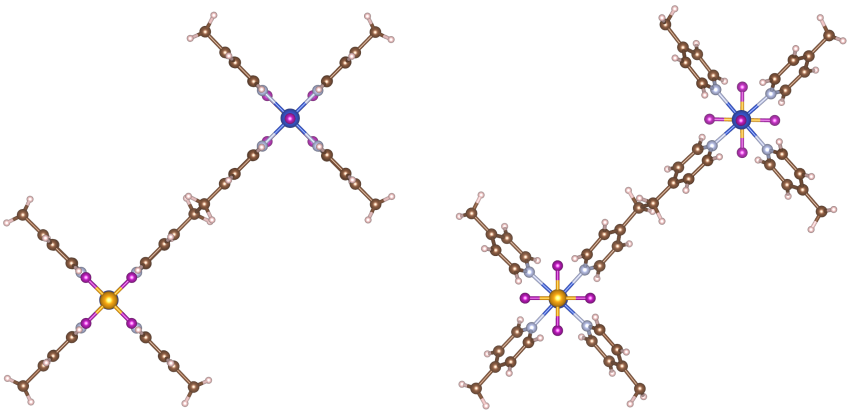

(a) Uncollapsed (b) Collapsed

Figure 69: Diagram shows the two DFT geometry minima found from a variety of starting configurations.

Table 19: DFT cell optimisation for six starting configurations of collapsed and uncollapsed unit cells.

| Starting Configuration | | | Final Configuration | | | Energy | Unit Cell Dimensions | | |
|---|---|---|---|---|---|---|---|---|---|
| Unit Cell | Fluorine Ring | HC Ring | Unit Cell | Fluorine Ring | HC Ring | (a.u) | A (Å) | B (Å) | C (Å) |
| Uncollapsed | Aligned | Vertical | Uncollapsed | Aligned | Vertical | -776.7565 | 19.13 | 19.15 | 8.50 |
| Uncollapsed | Aligned | S.P | Uncollapsed | Aligned | Vertical | -776.7569 | 19.13 | 19.15 | 8.50 |
| **Uncollapsed** | **Aligned** | **S.O** | **Uncollapsed** | **Aligned** | **Vertical** | **-776.7574** | **19.14** | **19.14** | **8.50** |
| Uncollapsed | Unaligned | Vertical | *Collapsed | Unaligned | S.O | -776.7535 | 19.08 | 19.09 | 8.12 |
| Uncollapsed | Unaligned | S.P | *Collapsed | Unaligned | S.P | -776.7549 | 19.18 | 18.98 | 8.12 |
| Uncollapsed | Unaligned | S.O | Collapsed | Unaligned | S.O | -776.7557 | 18.97 | 19.01 | 8.06 |
| Collapsed | Aligned | Vertical | Collapsed | Aligned | Vertical | -776.7654 | 18.91 | 18.93 | 8.51 |
| **Collapsed** | **Aligned** | **S.P** | **Collapsed** | **Aligned** | **Vertical** | **-776.7660** | **18.94** | **18.74** | **8.48** |
| Collapsed | Aligned | S.O | Collapsed | Aligned | Vertical | -776.7658 | 18.70 | 18.98 | 8.49 |
| Collapsed | Unaligned | Vertical | Collapsed | Unaligned | S.P | -776.7656 | 18.98 | 18.75 | 8.09 |
| Collapsed | Unaligned | S.P | Collapsed | Unaligned | S.P | -776.7651 | 18.69 | 19.07 | 8.09 |
| Collapsed | Unaligned | S.O | Collapsed | Unaligned | S.O | -776.7605 | 18.73 | 19.11 | 8.14 |

S.P- slanted parallel and S.O- slanted opposite (refer to Section 6.2.1)
*Collapsed- refers to partial collapse.

Table 19 shows that the further optimisation of the collapsed unit cell leads to the lowest (most favourable) energy of all the optimised structures, with fluorine rings aligned and aromatic rings in a vertical configuration. Interestingly, the energy difference between the most favourable collapsed and un-collapsed structure is only 22.6kJ/mol. The energy penalty for transforming from the collapsed to un-collapsed geometry is therefore within the energy scale of physisorption (which is generally between 20-40 kJ/mol[189]). This suggests that the adsorption of carbon dioxide could indeed cause the transformation of this structure, with initial adsorption of carbon dioxide prompting the more favourable collapsed structure to expand, enabling further adsorption of carbon dioxide at high pressures. It should be noted that in Table 19 there is a slight asymmetry in the x/y dimensions in some of the collapsed structures, which may suggest further refinement in the DFT optimisation is required, but this is expected to have a very small effect on the structures. The results thus illustrate that flexibility in this structure is likely, as the expected uncollapsed structure is less favourable even with this non-uniformity present in the collapsed geometry.

Additionally, the collapse appears linked to the initial fluorine positions, as all DFT calculations shows at least a partial collapse in the final configuration when the fluorine rings are out of alignment. This perhaps suggest that the fluorine rings play a role in the flexible transition of the MOF.

### 6.3.2 *Interpenetration*

In contrast to carbon dioxide adsorption (Figure 68), Figure 70 shows a type II isotherm for nitrogen at 77K. As adsorption in the nitrogen case is much lower in comparison to carbon dioxide, this suggests activated diffusion is taking place[190], in which an energy barrier is present for adsorption, requiring a minimal thermal energy to enable diffusion through the MOF to take place. As such, carbon dioxide at 273K was used instead to estimate the accessible surface area using the BET method with Rouquerol corrections[191]; the accessible surface area found was $306.3 \pm 1.1\ m^2g^{-1}$.[181]

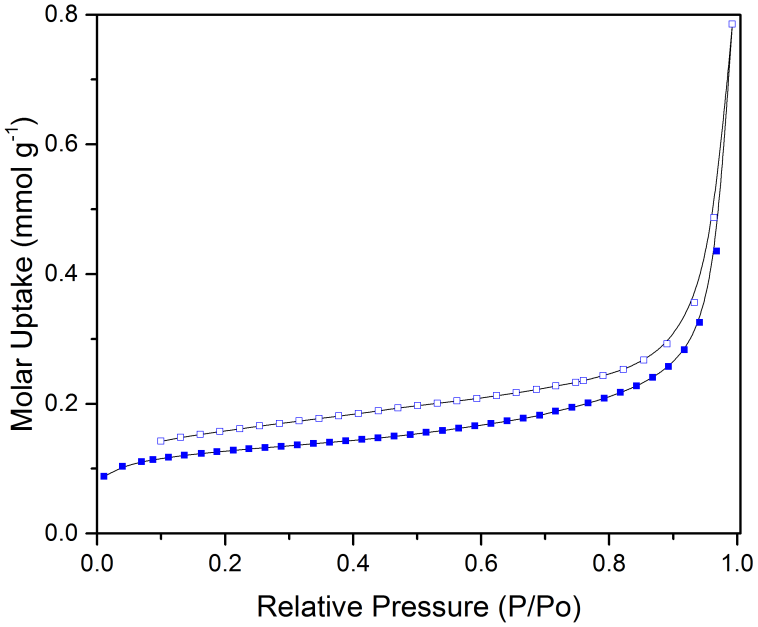


Figure 70: Experimental adsorption[181] of $N_2$ in $[Cu(bpetha)_2(SiF_6)_n]$. 77K, filled-adsorption, open-desorption.

The poreblazer software was used to calculate the simulated surface area of both the collapsed and un-collapsed MOF structures to discover if either could match this experimental value. The difference in accessible surface area for the collapsed and un-collapsed geometries was very slight, $2625 m^2 g^{-1}$ and $2666 m^2 g^{-1}$, respectively. Both these values are significantly higher than that of the experimental value, suggesting that there are differences between simulated and experimental structures. As mentioned, in the case of some of the MOFs within this SIFSIX family, interpenetration has been found to occur.[183, 185, 186] This could account for the large disparity in accessible surface areas if it were occurring for the new MOF.

Interpenetrated structures of $Cu(bpetha)_2SiF_6$, both collapsed and uncollapsed, were generated by replicating an identical MOF unit cell lattice on top of the existing MOF, but shifting the new lattice by half the unit cell dimensions along each axis (as found for similar interpenetrated SIFSIX structures[186]). The poreblazer interpenetrated accessible surface area for the collapsed and un-collapsed geometries was $0 m^2 g^{-1}$ and $2.83 m^2 g^{-1}$, respectively. As the experimental surface area falls between the non-interpenetrated and the interpenetrated accessible surface areas it suggests that the new MOF maybe partially interpenetrated, with large

areas of inaccessible interpenetrated pore volume and small areas of accessible non-interpenetrated volume. This highlights that if the experiment could be further refined to stop any interpenetration, then adsorption capacity could be greatly enhanced for carbon dioxide.

The percentage of interpenetration was estimated to be very high, $\approx 88\%$, in both the collapsed an uncollapsed structures, based on Equation 54.

$$S.A_{Actual} = S.A_{Int} \cdot X_{Int} + S.A_{Non-Int} \cdot X_{Non-Int} \tag{54}$$

where

| | |
|---|---|
| $S.A$ | Surface Area ($m^2 g^{-1}$) |
| $X$ | Fraction of Material Interpenetrated/Non-Interpenetrated |
| $Int$ | Interpenetrated |

## 6.4 CONCLUSION

This short chapter has illustrated, through modeling techniques, that the MOF created in the work of McAnally et al.[181], is likely flexible and also partially interpenetrated. Furthermore, it has highlighted that the original goal of increasing pore capacity in the SIFSIX family of MOFs could likely be achieved if the degree of interpenetration could be minimised during synthesis. This work overall highlighted that modeling can be an invaluable tool in the characterisation of new adsorbents and help better understand any unusual adsorption behaviour.

The next stage in this study will be a complementary GCMC study. This will be especially challenging, as to simulate carbon dioxide adsorption, framework point charges will need to be derived. The challenges and benefits of a GCMC studyof this material will be further discussed within Chapter 8 as future work.

Part IV

# SUMMARY

# 7

## SUMMARY

Since their recent characterisation, the scientific community's interest in Metal-Organic Frameworks (MOFs) has intensified. As a result of this growing interest there is a pressing need to better understand and quantify the performance of these adsorbents in practical applications. A comprehensive experimental study becomes infeasible for all but a select few MOFs, considering the full extent of variation inherent within these materials. As such, computational research could play an important role in initial assessment of MOFs thus enabling the highest performing MOFs to be properly researched for a given application. However, to fully utilise computational research a robust model is required to capture the behaviour of these MOFs. This is the major focus of this work; an attempt to improve MOF description within the field of adsorption. This work highlights structural and binding properties of MOFs that emphasise applicability in the field of adsorption.

The focus on adsorption stems from potential application in gas separations, since MOFs' pore size and binding sites can be tailored for a given gas mixture. There is then potential to generate high selectivities through these adsorbents. This is both true for large scale industrial applications, such as ethane/ethylene separations which are currently achieved through costly cryogenic distillation, as well as more specialist small scale applications. There are a number of drawbacks to these materials which are not within the remit of this thesis, such as high cost and potentially low thermal/mechanical stability. This thesis, instead focuses on optimsation of predictions of MOF performance for gas separations. Therafter, this tool can be utilised along with additional complexities of thermal stability, cost etc. in the future for design of MOFs for specific applications.

The Coordinatively Unsaturated Sites (CUS)-containing subset of MOFs is of special interest in this work, as CUS have been shown to strongly bind to certain adsorbates capable of electron donation to the MOF metal site. Thereby these CUS can be exploited to obtain high gas selectivities, in gas mixtures with components that have weak or no capability for electron donation. The challenge arises in computationally predicting adsorption in these MOFs. The standard forcefields commonly used have not been designed to account for the coordination bonds arising from CUS.

This thesis expands on the work of Fischer et al.[1], which looked into coupling Density Functional Theory (DFT) calculations with molecular simulations to better describe the CUS interaction for ethylene in HKUST-1. Chapter 3 further developed this model and investigated using the exact same CUS model parameters, obtained on HKUST-1, for other copper paddlewheel MOFs. The very good qualitative agreement found between simulation and experimental adsorption isotherms for these MOF variations was of key importance, highlighting the transferability of the CUS model across adsorbents. This transferability is important to demonstrate, as it is generally a prerequisite for use in large-scale simulation screening.

This work went on to apply the model in competitive binary adsorption of ethylene/ ethane in HKUST-1 (ethylene interacting with the CUS). The main outcome of the single component study was the identified poor performance of ethane simulation using standard forcefields. Furthermore, another approach from the work of Luna-Triguero et al.[93] was shown to perform poorly outside of conditions it was originally fit against in the case of ethylene, suggesting the adsorption mechanism was incorrectly captured. In the binary case, both the CUS and Luna-Triguero forcefields were shown to improve on the standard forcefield performance, although comparison with IAST and experiment concluded that further experimental datasets were required to properly quantify the models' performances any further. Although not conclusive, the reasonable performance of the CUS model for binary mixtures highlights its potential use for multi-component systems.

The CUS model was then expanded to carbon monoxide and nitrogen, which introduced the additional complexity of accounting for electrostatics. This work's benchmarking study of currently available carbon monoxide models showed deficiencies in all existing approaches, in terms of both isotherm agreement with experiment and correct capturing of the binding mechanism. The implementation of the CUS model greatly improved agreement with experiment for carbon monoxide in HKUST-1. The application of the CUS model for nitrogen was less successful, showing a slightly worse agreement with experiment than standard forcefields. It was determined that for nitrogen, additional experimental adsorption isotherms were required before definitive conclusions could be drawn.

The final results chapter looked into the characterisation of a new MOF, $Cu(bpetha)_2SiF_6$, in which a combination of DFT calculations and structural software analysis was able to identify possible flexible and interpenetrated characteristics within the new MOF. This novel application of computational research was relatively unrelated to the bulk of the investigation within this thesis, but highlighted the various roles computational work can fulfill.

Overall, this work has demonstrated a new and accurate approach for accounting for a unique and complex binding site. The development of the model focused on finding the best balance between accuracy and transferability, putting this model in a prime position for future use in large-scale screening simulations. Moreover, the generally strength of computational studies has been illustrated within this work, in which combination with experiment can only better the understanding of these unique, varied and at times 'unfathomable' materials.

# 8

# FUTURE WORK

## 8.1 CUS MODEL SIMULATIONS FOR OLEFINS AND PARAFFINS (CHAPTERS 3 AND 4)

1. The expansion of the CUS model to binary systems need further experimental datasets for validation. There is currently collaboration prospects with external groups to obtain this data. This would enable more reliable experimental data to be obtained, as there is strong evidence that the experimental datasets from the pelleted HKUST-1 sample (Chapter 4) are under adsorbing. Furthermore, a more detailed comparison of IAST, Luna-Triguero and the CUS model can be conducted at a wider range of conditions to more fully test the assumptions behind each approach. As can be observed in Figure 71, the L-T model and CUS model (see Chapter 4) shows very different adsorption behavior at higher coverage regions. The rapid uptake in adsorbed phased mol fraction for the CUS model is likely due to the adsorption at CUS, once these sites are filled the selectivity for ethylene over ethane decreases. This is not observed in the L-T model, likely because of the fact it does not capture the CUS binding mechanism correctly and the competition observed is occurring at other non-CUS sites (due to LJ parameters being modified).

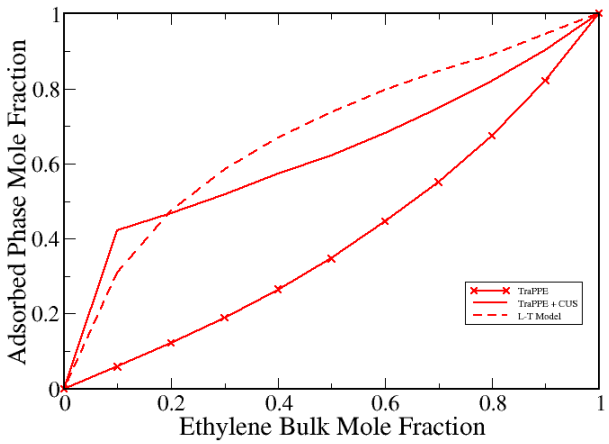


Figure 71: Adsorbed mole fraction of ethylene from binary ethane/ethylene mixtures in HKUST-1. Simulations (Lines), conditions: 273K and 4bar. No simulation points between 0-0.1 and 0.9-1.0 ethylene bulk mole fraction currently, due to preliminary nature of results.

2. Chapter 4 highlighted the shortcomings in the ethane description from standard forcefields, in HKUST-1 adsorption. The Luna-Triguero forcefield could be used to improve description of the ethane molecule. However, to maintain consistency in fluid-fluid forcefields (pertaining mainly to the cut-off schemes) the ethylene model will also need to be adapted; a possible candidate for this would be Liu et al.[142] modified TraPPE parameters. This will require the coding of a shifted potential into the CUS isolation code, which is planned future work, as well as rerunning GCMC simulation for the binary adsorption of ethane/ethylene in HKUST-1. However, until more reliable datasets are available, properly assessing the performance of these new parameters would be difficult.

3. After the proper validation of the CUS model for ethane/ethylene binary adsorption in HKUST-1, it would be interesting to predict the binary adsorption behaviour of similar copper paddlwheel MOFs, complementing the work of Chapter 3 but for the binary case.

## 8.2 CUS MODEL SIMULATIONS FOR CARBON MONOXIDE AND NITROGEN (CHAPTER 5)

1. In the case of nitrogen, further experimental adsorption isotherms are required at the relevant conditions. Currently, a collaboration in progress may yield the required datasets. This will enable the performance of the CUS model for nitrogen to be better understood.

2. After the CUS model performance of nitrogen is better known, the competitive binary adsorption of $CO/N_2$ could be investigated for CUS-containing MOFs.

## 8.3 SIFSIX MOFS INVESTIGATION (CHAPTER 6)

1. Chapter 6 concluded that a GCMC study would be useful, enabling the adsorption characteristics of the new MOF to be better understood. This would require deriving point charges for the framework while also attempting to account for flexibility, interpenetration and ring-rotation within the MOF. As such, it would first be advisable to conduct a point charge benchmarking analysis on a simpler member of the SIFSIX family, such as SIFSIX-2-Cu-i[192] which has fewer degrees of freedom, to first better assess point charge methods.

## 8.4 GENERAL FUTURE WORK

1. The expansion of the CUS model to other adsorbates capable of electron donation is a key driver behind future work. As the model has been successfully expanded to carbon monoxide, carbon dioxide would be a natural successor for this approach. Carbon dioxide is a very common gas and its separation is key in fields such as carbon capture, as such it is potentially a very important gas to be simulated accurately.

Part V

# APPENDIX

# A

# APPENDIX

## A.1 CUS SECTION- MUSIC CODE

This section is a copy of a condensed version of the CUS code used within music, it will include comments from previous Music developers.

Listing 1: CUS Interaction calculated within Music code (`listings` manual)

```
!
    ------------------------------------------------------------------------

! This module contains the routines specific to initializing and actually
! calculating OMS INTERACTIONS. It is initialized using file information in "
    OMS_init"
!
! Input units from file MUST be:
! Acon: Constant
! Bcon: Constant
! Rin:
! Din:
! Alpha:
!
! Ouput units are in kcal/mol (for energy) and kcal/mol/Angstrom (for forces)
!
! Needed Improvements:
! 1) addition of smoothing features from the old code.
! 2) use of the "reference" parameter
!
    ------------------------------------------------------------------------
```

```
Module OMS

  Use defaults, Only: RDbl, strLen, lstrLen, LOW_DIST_CUTOFF, OMS_kcalmole_kb,
       &
      HIGH_DIST_CUTOFF, xlstrlen, SIZE_OF_HOT, one, dbgflag, &
      defaults_virialsum, SHIFT_DIST_CUTOFF
  Use utils, Only: toupper, split, toreal, getlineswpair, real2str, int2str
  Use file, Only: file_getunit
  Use vector, Only: VecType, Assignment(=), Operator(+), Operator(-), &
      Operator(*), Operator(/), vector_getnormsq, vector_display, mag
  Use atom, Only: atom_getmass
  Use ffstate, Only: ffstate_acalc

  Implicit None
  Save

  Private
  Public :: OMS_Params, OMS_displayparams, OMS_calc_interaction, OMS_idstring,
       &
      OMS_isinit, OMS_displayRinDin, Assignment(=), &
      OMS_init, OMS_displayCutOffs, &
      !OMS_calc_interactionHOT,
      OMS_displayFactRatio, &
      OMS_getcutoff, OMS_display, OMS_grpint, OMS_snglint, OMS_snglintHOT,&
      OMS_snglint2, OMS_getcut, OMS_multint, OMS_getABCD

  Interface Assignment(=)
    Module Procedure OMS_copy
  End Interface

  Interface OMS_calc_interaction
    Module procedure OMS_calc_snglInteraction
    Module procedure OMS_calc_multInteraction
  End Interface
!!$
!!$  Interface OMS_calc_interactionHOT
!!$    Module procedure OMS_calc_multInteractionHOT
```

```
!!$  End Interface

  Type OMS_Params
    Character(len=strLen) :: atom_name1, atom_name2
    Character(len=strLen) :: source
    Logical               :: off
    Logical               :: initialized
    Logical               :: shifted        ! True if potential is truncated and
         shifted
    Real(kind=RDbl)       :: Bcon, Rin, Din, Alpha, Acon
    Real(kind=RDbl)       :: Fact, Ratio
    Character(len=100)    :: line
    Character(len=80)     :: reference   !** not being used, but good idea
    Real(kind=RDbl)       :: hicut,hicut2, shiftcut, shiftcut2
    Real(kind=RDbl)       :: ncut,ncut2    ! neighbor cutoff
    Real(kind=RDbl)       :: locut = 0.001_RDbl, locut2 = 1.0E-6_RDbl ! lower
        bound to prevent overflow
    Real(kind=RDBL)       :: nrgcutoff     ! potential energy at high cutoff.
        Used to shift the potential
  End Type OMS_Params

  Character(len=strLen), Parameter          :: OMS_idstring = 'OMS'

  Real(kind=RDbl), Parameter                :: OMS_NCUTOFF = 200.00_RDbl



Contains
  !
      ------------------------------------------------------------------------

  ! Initialize the interaction information from the file line
  ! Requires:  params -- OMS parameter structure to initialize
  !            line -- input command line to interpret
  !
      ------------------------------------------------------------------------

  Subroutine OMS_init(params,line)
```

```
Type(OMS_Params), Intent(InOut)    :: params
Character(*), Intent(In)           :: line

Integer                                  :: nfields,n,i,unit,ios
Integer                                  :: nlines
Character(len=150), Dimension(10)        :: lines
Character(len=strLen)                    :: filename,name1,name2
Character(len=strLen), Dimension(10)     :: fields,chunks

!** allow for the possibility that the line only contains the filename
!** where the actual potentials are stored
If (Index(Toupper(line),'FILE') /= 0) Then
  nfields = split(line,fields)
  name1 = Trim(fields(1))
  name2 = Trim(fields(2))
  filename = ''

  Do i = 1,nfields
    n = split(fields(i),chunks,'@')
    If (n > 1) Then
      If (Trim(chunks(1)) == 'FILE') Then
        filename = trim(chunks(2))
      End If
    End If
  End Do

  !** Open the file and get the line
  If (filename /= '') Then
    unit = file_getunit(filename)
    Open(unit=unit, file=filename, status='old', IOSTAT=ios)
    If (ios /= 0) Then
      Write(0,'(2a,i4,2a)') __FILE__,": ",__LINE__, &
          '  Could not open file ',trim(filename)
      Stop
    End If
    Call getlineswpair(unit,name1,name2,' ',nlines,lines)
    Close(unit=unit)
```

```
    If (nlines == 0) Then
      Write(0,'(2a,i4,2a)') __FILE__,": ",__LINE__, &
          ' Could not find matching line in file: ',Trim(filename)
      Stop
    End If
    If (nlines > 1) Then
      Write(0,'(2a,i4,2a)') __FILE__,": ",__LINE__, &
          ' Too many matching lines in file: ',Trim(filename)
      Stop
    End If
  Else
    Write(0,'(2a,i4,2a)') __FILE__,": ",__LINE__, &
        ' Could not find filename in line: ',Trim(line)
    Stop
  End If
Else
  lines(1) = line
End If

nfields = split(lines(1),fields)
params%line = lines(1)
params%off = .FALSE.
params%shifted = .FALSE.
params%locut = LOW_DIST_CUTOFF
params%locut2 = LOW_DIST_CUTOFF*LOW_DIST_CUTOFF
params%hicut = HIGH_DIST_CUTOFF
params%hicut2 = HIGH_DIST_CUTOFF*HIGH_DIST_CUTOFF
params%shiftcut = SHIFT_DIST_CUTOFF
params%shiftcut2 = SHIFT_DIST_CUTOFF*SHIFT_DIST_CUTOFF
params%ncut  = OMS_NCUTOFF
params%ncut2 = OMS_NCUTOFF*OMS_NCUTOFF
params%atom_name1 = Trim(fields(1))
params%atom_name2 = Trim(fields(2))

Do i = 4,nfields
  n = split(fields(i),chunks,'@')
  Select Case(toupper(chunks(1)))
```

```
Case('OFF')
  params%off = .True.
  !** Set the remaining parameters to zero
  params%Rin = 0.0_RDbl
  params%Acon = 0.0_RDbl
  params%Bcon = 0.0_RDbl
  params%Din = 0.0_RDbl
  params%Alpha = 0.0_RDbl
  params%hicut = 0.0_RDbl
  params%hicut2 = 0.0_RDbl
  params%shiftcut = 0.0_RDbl
  params%shiftcut2 = 0.0_RDbl

Case('RIN')
    params%Rin = toreal(chunks(2))

Case('DIN')
    params%Din = toreal(chunks(2))

Case('ACON')
    params%Acon = toreal(chunks(2))

Case('ALPHA')
    params%Alpha = toreal(chunks(2))

Case('BCON')
    params%Bcon = toreal(chunks(2))

Case('TRUNC')
  Write(0,'(2a,i4,2a)') __FILE__,":",__LINE__, &
      " WARNING: Use of the label TRUNC has been depreciated in favor",
          &
      " of HICUT"
  params%hicut = toreal(chunks(2))
  params%hicut2 = params%hicut**2

Case('HICUT')
  params%hicut = toreal(chunks(2))
```

```
        params%hicut2 = params%hicut**2

      Case('SHIFTCUT')
        params%shiftcut = toreal(chunks(2))
        params%shiftcut2 = params%shiftcut**2

      Case('LOWCUT')
       ! params%locut = toreal(chunks(2))
       ! params%locut2 = params%locut**2
        Write(0,'(2a,i4,2a)') __FILE__,":",__LINE__, &
            " WARNING: Use of the label LOWCUT has been depreciated in", &
            " favor of LOCUT"
        Write(0,*) 'LOCUT now coded as parameter = 0.001 A'
        Write(0,*) 'To alter, reset in variable declaration CMS.F90'

      Case('LOCUT')
       !params%locut = toreal(chunks(2))
       !params%locut2 = params%locut**2
       Write(0,*) 'LOCUT now coded as parameter = 0.001 A'
       Write(0,*) 'To alter, reset in variable declaration CMS.F90'

      Case('SHIFTED')
        params%shifted=.True.

      Case Default
        Write(0,'(2a,i4,2a)') __FILE__,": ",__LINE__, &
            'Unable to identify CMS interaction string ',Trim(chunks(1))
        Stop
      End Select
    End Do

!If shifted was to be added use below. (Otherwise ignore).
   If(params%shifted)Then
        params%nrgcutoff=0._RDbl
    Else
        params%nrgcutoff=0._RDbl
    Endif
```

```
  params%initialized = .True.
        params%source = "atm_atm"

End Subroutine OMS_init

!-----------------------------------------------------------------------
! Returns true if the fields of "params" have been initialized
!-----------------------------------------------------------------------
Logical Function OMS_isinit(params)
  Type(OMS_Params), Intent(in) :: params

  OMS_isinit = params%initialized
End Function OMS_isinit

!-----------------------------------------------------------------------
! Initialize params by copying from an existing params
! Requires: newparams -- new params, to be initialized
!           oldparams -- old params
!-----------------------------------------------------------------------
Subroutine OMS_copy(newparams,oldparams)
  Type(OMS_Params), Intent(Out)      :: newparams
  Type(OMS_Params), Intent(In)       :: oldparams

  newparams%atom_name1 = oldparams%atom_name1
  newparams%atom_name1 = oldparams%atom_name2
  newparams%source = oldparams%source
  newparams%off = oldparams%off
  newparams%initialized = oldparams%initialized
  newparams%Rin = oldparams%Rin
  newparams%Din = oldparams%Din
  newparams%Alpha = oldparams%Alpha
  newparams%Acon = oldparams%Acon
  newparams%Bcon = oldparams%Bcon
  newparams%Ratio = oldparams%Ratio
  newparams%Fact = oldparams%Fact
  newparams%line = oldparams%line
  newparams%reference = oldparams%reference
  newparams%hicut = oldparams%hicut
```

```
  newparams%hicut2 = oldparams%hicut2
  newparams%shiftcut = oldparams%shiftcut
  newparams%shiftcut2 = oldparams%shiftcut2
  newparams%ncut = oldparams%ncut
  newparams%ncut2 = oldparams%ncut2
  newparams%locut = oldparams%locut
  newparams%locut2 = oldparams%locut2
  newparams%shifted = oldparams%shifted
  newparams%nrgcutoff=oldparams%nrgcutoff

End Subroutine OMS_copy

!-----------------------------------------------------------------------
! Calculate the interaction
!-----------------------------------------------------------------------
Subroutine OMS_calc_snglInteraction(params,sepvec,pot,OMSflag)
  Type(OMS_Params), Intent(INOUT)              :: params
  Type(VecType), Intent(IN)                 :: sepvec
  Real(kind = RDbl), Intent(OUT)            :: pot
  Logical, Intent(Out)                      :: OMSflag

  Real(kind = RDbl)                         :: ratio,Fact,r2,r1

  !** Initialize the flag
  OMSflag = .True.

  !** Initialize the potential and (optionally) the force
  pot = 0.0_RDbl

  !** Check if the interaction is on
  If (params%off) Return

  !** Get the square of the distance
  r2 = vector_getnormsq(sepvec)
  r1 = SQRT(r2)
  params%Ratio = params%Acon / r1
  params%Fact = params%Alpha * (1-(r1/params%Rin))
```

```
    Ratio = params%Ratio
    Fact = params%Fact

!Shift distance is actually 0.5Ang, shown as 0.25 as its against hicut^2
!Also remeber the shifted function is (5-10r) so the twenty may need to be
    changed depending on 0.5

  !**Check if it is within the cut-off radius
    If (r2 > params%hicut2) Return

    If (r2 < params%locut2) Then
            OMSflag = .False.
            Return

    Else If (r2 < params%shiftcut2) Then

!for conversion see defaults.F90, ensure input units are correct.

    pot = OMS_kcalmole_kb * ((-1*(ratio**params%Bcon))+params%Din*(exp(Fact)
        -(2*exp((0.5*Fact)))))

    Else If (r2 < params%hicut2) Then

    pot = OMS_kcalmole_kb * ((-1*(ratio**params%Bcon))+params%Din*(exp(Fact)
        -(2*exp(0.5*Fact))))*(params%hicut-r1)*(1/(params%hicut-params%
        shiftcut))
    End If

    If(params%shifted)pot=pot-params%nrgcutoff

  End Subroutine OMS_calc_snglInteraction

  !
      ------------------------------------------------------------------------

  ! Returns the value of the high end cutoff. If the NEIGHBOR flag is
  ! present, check to see if the NEIGHBOR cutoff should be returned
  ! Neighbour cut-off is larger value than  high cutoff. It is useful while
```

```
! making list of intra-pairs in the beginning during molecule
! initialization.
! Requires: params -- OMS params
!           neighbor -- flag to get neighbor cutoff
!
    ------------------------------------------------------------------------

Real(Kind=RDbl) Function OMS_getcutoff(params,neighbor)
  Type(OMS_Params), Intent(In)        :: params
  Logical, Optional, Intent(In)       :: neighbor

  !** Default value
  OMS_getcutoff = params%hicut
  OMS_getcutoff = params%shiftcut

  !** Check if we need to return the neighbor cutoff
  If (Present(neighbor)) Then
    If (neighbor) Then
      OMS_getcutoff = params%ncut
    End If
  End If
End Function OMS_getcutoff

!-------------------------------------------------------
! Returns a string with the properly formatted OMS params
! Requires: params -- OMS params
!-------------------------------------------------------
Function OMS_displayparams(OMSparams)
  Character(len=strLen)        :: OMS_displayparams
  Type(OMS_Params), Intent(In) :: OMSparams
  Character(len=strLen)        :: strRin, strDin, strAcon, strAlpha, strBcon
  strRin=real2str(OMSparams%Rin,5)
  strDin=real2str(OMSparams%Din,5)
  strAcon=real2str(OMSparams%Acon,5)
  strBcon=real2str(OMSparams%Bcon,5)
  strAlpha=real2str(OMSparams%Alpha,5)
```

```
  If(.Not. OMSparams%shifted)Then
    Write(OMS_displayparams,'(1x,a,2x,a,2x,a,2x,a,2x,a)') Trim(strRin), Trim
        (strDin), &
         Trim(strAcon), Trim(strBcon), Trim(strAlpha)
  Else
    Write(OMS_displayparams,'(1x,a,2x,a,2x,a,2x,a,2x,a,2x,e23.15)') Trim(
        strRin), Trim(strDin), &
         Trim(strAcon), Trim(strBcon), Trim(strAlpha), OMSparams%nrgcutoff
  End If
End Function OMS_displayparams

!
    ------------------------------------------------------------------------

! Returns a string containing the Ro and Do values
! Requires: params -- OMS params
!
    ------------------------------------------------------------------------

Function OMS_displayRinDin(OMSparams)
  Character(len=lstrLen)      :: OMS_displayRinDin
  Type(OMS_Params), Intent(In) :: OMSparams

  Character(len=lstrLen)      :: string1,string2,string3,string4,string5

  If (OMSparams%off) Then
    Write(OMS_displayRinDin,'(a)') "OFF"
  Else
    string1 = real2str(OMSparams%Rin,6)
    string2 = real2str(OMSparams%Din,6)
    string3 = real2str(OMSparams%Acon,6)
    string4 = real2str(OMSparams%Bcon,6)
    string5 = real2str(OMSparams%Alpha,6)
    Write(OMS_displayRinDin,'(5(2a,1x,a,3x))') "Ro: ", &
        Trim(string1),"[ang]","Do: ",Trim(string2),"[kJ/mol]","A: ", &
        Trim(string3),"[L][E]","B: ",Trim(string4),"","Alpha: ", &
        Trim(string5),""
  End If
```

```
End Function OMS_displayRinDin

!
    ------------------------------------------------------------------------

! Returns a string containing nicely formated A and B values
! Requires: params -- OMS params
!
    ------------------------------------------------------------------------

Function OMS_displayFactRatio(OMSparams)
  Character(len=lstrLen)               :: OMS_displayFactRatio
  Type(OMS_Params), Intent(In)         :: OMSparams

  Character(len=xlstrLen)              :: string1,string2

  If (OMSparams%off) Then
    Write(OMS_displayFactRatio,'(a)') "OFF"
  Else
    string1 = real2str(OMSparams%Fact,8)
    string2 = real2str(OMSparams%Ratio,8)
    Write(OMS_displayFactRatio,'(2(2a,1x,a,3x))') "Factor: ", &
        Trim(string1),"","Ratio: ",Trim(string2),""
  End If

End Function OMS_displayFactRatio

!
    ------------------------------------------------------------------------

! Returns a string containing the cutoff Values
! Requires: params -- OMS params
!
    ------------------------------------------------------------------------

Function OMS_displayCutOffs(OMSparams)
  Character(len=lstrLen)          :: OMS_displayCutOffs
```

```
  Type(OMS_Params), Intent(In)     :: OMSparams

  Character(len=strLen)           :: string1,string2, string3

  If (OMSparams%off) Then
    Write(OMS_displayCutoffs,'(a)') "OFF"
  Else
    string1 = real2str(OMSparams%hicut,5)
    string2 = real2str(OMSparams%locut,5)
    string3 = real2str(OMSparams%shiftcut,5)
    Write(OMS_displayCutOffs,'(3(2a,1x,a,3x),f8.4)') &
        "high cutoff: ",Trim(string1),"Ang", &
        "low cutoff: ",Trim(string2),"Ang", &
        "Shift cutoff: ",Trim(string3),"Ang"
  End If

End Function OMS_displayCutOffs

!-----------------------------------------------------------------------
! Displays the full set of OMS parameters for the structure
! Requires: params -- the OMS parameters structure
!           indent -- number of spaces to indent
!           unit -- unit to write into
!-----------------------------------------------------------------------
Subroutine OMS_display(params,indent,unit)
  Type(OMS_Params), Intent(In)        :: params
  Integer, Intent(In)                 :: indent,unit

  Character(len=indent)       :: blank
  Character(len=xlstrLen)     :: string

  blank = Repeat(' ',indent)

  If (.Not. params%initialized) Return

  If (params%off) Then
    Write(unit,'(5a)') blank,Trim(params%atom_name1),'—', &
        Trim(params%atom_name2),' Interaction OFF'
```

```
  Else
    Write(unit,'(6a)') blank,Trim(params%atom_name1),'—',&
        Trim(params%atom_name2),' OMS parameters from ',Trim(params%source)
    string = OMS_displayRinDin(params)
    Write(unit,'(2x,2a)') blank,Trim(string)
    string = OMS_displayFactRatio(params)
    Write(unit,'(2x,2a)') blank,Trim(string)
    string = OMS_displayCutOffs(params)
    Write(unit,'(2x,2a)') blank,Trim(string)
  End If

End Subroutine OMS_display

!
    ------------------------------------------------------------------------

! Tina added
! Gets the A, B, C, D parameters of the Lennard-Jones potential
!
    ------------------------------------------------------------------------


 Subroutine OMS_getABCD(params_OMS,pot_param)

  Type(OMS_params), Intent(IN)     :: params_OMS
  Real(kind = RDbl), Dimension(7)  :: pot_param

  pot_param(1) = params_OMS%Acon
  pot_param(2) = params_OMS%Bcon
  pot_param(3) = params_OMS%Alpha
  pot_param(4) = params_OMS%Din
  pot_param(5) = params_OMS%Rin
  pot_param(6) = params_OMS%Fact
  pot_param(7) = params_OMS%Ratio

END Subroutine OMS_getABCD
```

```
  !
      ------------------------------------------------------------------------

  ! Tina added
  ! Gets the hicut and locut parameters of the Lennard-Jones potential
  !
      ------------------------------------------------------------------------


  Subroutine OMS_getcut(params_OMS,pot_param)

    Type(OMS_params), Intent(IN)      :: params_OMS
    Real(kind = RDbl), Dimension(3)   :: pot_param

    pot_param(1) = params_OMS%hicut
    pot_param(2) = params_OMS%locut
    pot_param(3) = params_OMS%shiftcut


  End Subroutine OMS_getcut

End Module OMS
```

## A.2 EFFECT OF UFF FORCEFIELD ON CO CUS MODEL

An additional validation which this work will tackle is investigating the effect that varying the fluid-fluid models has on the carbon monoxide CUS model developed in Chapter 5. To this end, the UFF model will be tested, in replacement of the M-C, in combination with the vdw-DF2 DFT profile to form a new CUS model (framework point charges from Castillo et al.[89]). The exact same CUS model fitting procedure and GCMC inputs are used as in Chapter 5, with the exception that UFF[155] carbon monoxide model is used in replacement of the Martín-Calvo et al.[157] (M-C) model.

Table 20: CUS parameters obtained from DFT fitting.

| $E_{xc}$ | Adsorbate | $R_o$ (Å) | $D_o$ (kJ/mol) | $\alpha$ | A | B |
|---|---|---|---|---|---|---|
| vdw-DF2 | Carbon Monoxide (M-C) | 2.75 | 9.829 | 8.25 | 3.243 | 10.1068 |
| vdw-DF2 | Carbon Monoxide (UFF) | 2.489 | 17.136 | 9.7511 | 3.187 | 11.0868 |

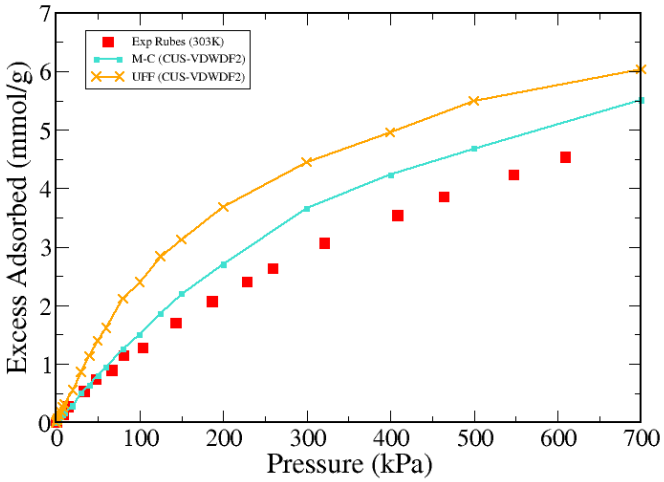


Figure 72: VDW-DF2 CUS model simulated (lines), and experimental[171] (points) carbon monoxide adsorption isotherms in HKUST-1.

The UFF model shows a larger increase in adsorption compared to the CUS M-C model, and agreement with experiment worsens. Figure 73 shows that the total

interaction at the CUS minimum is similar to that of the M-C, and matches DFT calculations well. The issue is due to the very different fluid-fluid point charges of the UFF model, as shown in Table 16 (Chapter 5), the CO carbon is postive in the UFF model while it is negative in the M-C model. Therefore at the CUS minimum, the electrostatic interaction of UFF is repulsive at $\approx$ +5 kJ/mol, while M-C is attractive at $\approx$ -7.5kJ/mol. This means that the CUS specific interaction has to be much stronger for the UFF model, to match the DFT minimum (this is indicated by the much larger UFF $D_0$ value in Table 20), this makes it harder to fit away from the minimum leading to poor agreement between the UFF CUS model and the DFT calculations across the latter part of the profile, seen in Figure 73.

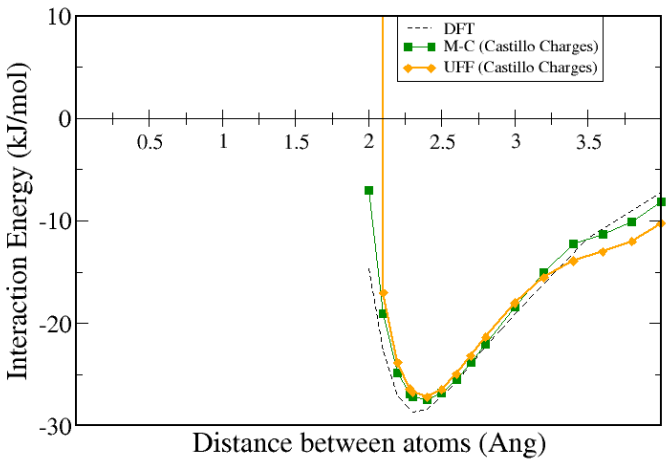


Figure 73: VDW-DF2 CUS model interaction energy (CUS + LJ + Electrostatics) along CUS profile for carbon monoxide in HKUST-1. Two different fluid-fluid models used; UFF[155] and M-C[157].

# BIBLIOGRAPHY


[1] Michael Fischer, José R. B. Gomes, Michael Fröba, and Miguel Jorge. "Modeling Adsorption in Metal-Organic Frameworks with Open Metal Sites: Propane/Propylene Separations." In: *Langmuir* 28.22 (2012), pp. 8537–8549.

[2] R. Jungk. *Brighter Than a Thousand Suns: A Personal History of the Atomic Scientists*. A Harvest book, HB182. Harcourt Brace, 1958. ISBN: 9780156141505.

[3] Hong-Cai Zhou, Jeffrey R. Long, and Omar M. Yaghi. "Introduction to Metal-Organic Frameworks." In: *Chemical Reviews* 112.2 (2012), pp. 673–674.

[4] CCDC. *How Many MOFs Are There In The CSD*. (Last accessed 16 August 2016). 2014. URL: `https://www.ccdc.cam.ac.uk/support-and-resources/support/case/?caseid=9833bd2c-27f9-4ff7-8186-71a9b415f012` (visited on 08/16/2016).

[5] Michael O'Keeffe, Nathan W. Ockwig, Hee K. Chae, Mohamed Eddaoudi, Jaheon Kim, and Omar M. Yaghi. "Reticular Synthesis and the Design of New Materials." In: *Nature* 423 (6941 2003), pp. 705–714.

[6] Christopher E. Wilmer, Michael Leaf, Chang Yeon Lee, Omar K. Farha, Brad G. Hauser, Joseph T. Hupp, and Randall Q. Snurr. "Large-scale Screening of Hypothetical Metal-Organic Frameworks." In: *Nature* 4 (2012), pp. 83–89.

[7] Yabing He, Wei Zhou, Taner Yildirim, and Banglin Chen. "A series of metal-organic frameworks with high methane uptake and an empirical equation for predicting methane storage capacity." In: *Energy Environ. Sci.* 6 (9 2013), pp. 2735–2744.

[8] Helge Bux, Christian Chmelik, Rajamani Krishna, and Juergen Caro. "Ethene/ethane separation by the {MOF} membrane ZIF-8: Molecular correlation of permeation, adsorption, diffusion." In: *Journal of Membrane Science* 369.1–2 (2011), pp. 284 –289.

[9] D. Farrusseng. *Metal-Organic Frameworks: Applications from Catalysis to Gas Storage*. Metal-organic Frameworks: Applications from Catalysis to Gas Storage. Wiley, 2011. ISBN: 9783527328703.

[10] Stephen S. Y. Chui, Samuel M.F. Lo, Jonathan P. H. Charmant, A. Guy Orpen, and Ian D. Williams. "A Chemically Functionalizable Nanoporous Material $[Cu_3(TMA)_2(H_2O)_3]_n$." In: *Science* 283.5405 (1999), pp. 1148–1150.

[11] Yichao Lin, Chunlong Kong, and Liang Chen. "Amine-functionalized metal-organic frameworks: structure, synthesis and applications." In: *RSC Adv.* 6 (39 2016), pp. 32598–32614.

[12] Sara Rojas, Francisco J. Carmona, Carmen R. Maldonado, Patricia Horcajada, Tania Hidalgo, Christian Serre, Jorge A. R. Navarro, and Elisa Barea. "Nanoscaled Zinc Pyrazolate Metal-Organic Frameworks as Drug-Delivery Systems." In: *Inorganic Chemistry* 55.5 (2016). PMID: 26886572, pp. 2650–2663.

[13] Lauren E. Kreno, Kirsty Leong, Omar K. Farha, Mark Allendorf, Richard P. Van Duyne, and Joseph T. Hupp. "Metal-Organic Framework Materials as Chemical Sensors." In: *Chemical Reviews* 112.2 (2012). PMID: 22070233, pp. 1105–1125.

[14] Yun-Nan Gong, Di-Chang Zhong, and Tong-Bu Lu. "Interpenetrating metal-organic frameworks." In: *CrystEngComm* 18 (15 2016), pp. 2596–2606.

[15] A. Schneemann, V. Bon, I. Schwedler, I. Senkovska, S. Kaskel, and R. A. Fischer. "Flexible metal-organic frameworks." In: *Chem. Soc. Rev.* 43 (16 2014), pp. 6062–6096.

[16] P. L. Llewellyn et al. "Complex Adsorption of Short Linear Alkanes in the Flexible Metal-Organic-Framework MIL-53(Fe)." In: *Journal of the American Chemical Society* 131.36 (2009). PMID: 19697934, pp. 13002–13008.

[17] Yiming Zhang, Baiyan Li, Rajamani Krishna, Zili Wu, Dingxuan Ma, Zhan Shi, Tony Pham, Katherine Forrest, Brian Space, and Shengqian Ma. "Highly Selective Adsorption of Ethylene Over Ethane in a MOF Featuring the Combination of Open Metal Site and [Small pi]-Complexation." In: *Chem. Commun.* 51 (13 2015), pp. 2714–2717.

[18] Miguel Jorge, Michael Fischer, José R. B. Gomes, Christophe Siquet, João C. Santos, and Alírio E. Rodrigues. "Accurate Model for Predicting Adsorption of Olefins and Paraffins on MOFs with Open Metal Sites." In: *Industrial & Engineering Chemistry Research* 53.40 (2014), pp. 15475–15487.

[19] Mikhail S. Nechaev, Víctor M. Rayón, and Gernot Frenking. "Energy Partitioning Analysis of the Bonding in Ethylene and Acetylene Complexes of Group 6, 8, and 11 Metals: $(CO)_5$TM-$C_2H_x$ and $Cl_4$TM-$C_2H_x$ (TM = Cr, Mo, W), $(CO)_4$TM-$C_2H_x$ (TM = Fe, Ru, Os), and TM+-$C_2H_x$ (TM = Cu, Ag, Au)." In: *The Journal of Physical Chemistry A* 108.15 (2004), pp. 3134–3142.

[20] David S. Sholl and Ryan P. Lively. "Seven chemical separations to change the world." In: *Nature* 532 (2016), pp. 435–437.

[21] A. Van Miltenburg, W. Zhu, F. Kapteijn, and J.A. Moulijn. "Adsorptive Separation of Light Olefin/Paraffin Mixtures." In: *Chemical Engineering Research and Design* 84.5 (2006), pp. 350 –354.

[22] Marco Tagliabue, David Farrusseng, Susana Valencia, Sonia Aguado, Ugo Ravon, Caterina Rizzo, Avelino Corma, and Claude Mirodatos. "Natural gas treating by selective adsorption: Material science and chemical engineering interplay." In: *Chemical Engineering Journal* 155.3 (2009), pp. 553 – 566.

[23] Brian Joseph Maring and Paul A. Webley. "A new simplified pressure/-vacuum swing adsorption model for rapid adsorbent screening for CO2 capture applications." In: *International Journal of Greenhouse Gas Control* 15.0 (2013), pp. 16–31.

[24] Jarad A. Mason, Kenji Sumida, Zoey R. Herm, Rajamani Krishna, and Jeffrey. R. Long. "Evaluating metal-organic frameworks for post-combustion carbon dioxide capture via temperature swing adsorption." In: *Energy Environ. Sci.* 4 (8 2011), pp. 3030–3040.

[25] Vinay Mulgundmath and F.Handan Tezel. "Optimisation of carbon dioxide recovery from flue gas in a TPSA system." English. In: *Adsorption* 16.6 (2010), pp. 587–598.

[26] R.T. Yang. *Gas Separation by Adsorption Processes*. Butterworths series in chemical engineering. Elsevier Science, 2013, pp. 275–280.

[27] João Pires, Joana Fernandes, Ana C. Fernandes, and Moisés Pinto. "Reverse selectivity of zeolites and metal-organic frameworks in the ethane/ethylene separation by adsorption." In: *Separation Science and Technology* 52.1 (2017), pp. 51–57.

[28] Taku Watanabe and David S. Sholl. "Accelerating Applications of Metal-Organic Frameworks for Gas Adsorption and Separation by Computational Screening of Materials." In: *Langmuir* 28.40 (2012), pp. 14114–14128.

[29] Benjamin J. Sikora, Christopher E. Wilmer, Michael L. Greenfield, and Randall Q. Snurr. "Thermodynamic analysis of Xe/Kr selectivity in over 137 000 hypothetical metal-organic frameworks." In: *Chem. Sci.* 3 (7 2012), pp. 2217–2223.

[30] Zhenlan Fang, Bart Bueken, Dirk E. De Vos, and Roland A. Fischer. "Defect-Engineered Metal-Organic Frameworks." In: *Angewandte Chemie International Edition* 54.25 (2015), pp. 7234–7254.

[31] David S. Sholl and Ryan P. Lively. "Defects in Metal-Organic Frameworks: Challenge or Opportunity?" In: *The Journal of Physical Chemistry Letters* 6.17 (2015). PMID: 26268796, pp. 3437–3444.

[32] L. Sarkisov. "Molecular Simulation of Low Temperature Argon Adsorption in Several Models of IRMOF-1 with Defects and Structural Disorder." In: *Dalton Trans.* 45 (10 2016), pp. 4203–4212.

[33] Jason A. Gee and David S. Sholl. "Effect of Framework Flexibility on C8 Aromatic Adsorption at High Loadings in Metal-Organic Frameworks." In: *The Journal of Physical Chemistry C* 120.1 (2016), pp. 370–376.

[34] D. Fairen-Jimenez, S. A. Moggach, M. T. Wharmby, P. A. Wright, S. Parsons, and T. Düren. "Opening the Gate: Framework Flexibility in ZIF-8 Explored by Experiments and Simulations." In: *Journal of the American Chemical Society* 133.23 (2011). PMID: 21553843, pp. 8900–8902.

[35] Michael Fischer, José R.B. Gomes, and Miguel Jorge. "Computational Approaches to Study Adsorption in MOFs with Unsaturated Metal Sites." In: *Molecular Simulation* 40.7-9 (2014), pp. 537–556.

[36] Cigdem Altintas and Seda Keskin. "Computational Screening of MOFs for $C_2H_6/C_2H_4$ and $C_2H_6/CH_4$ Separations." In: *Chemical Engineering Science* 139 (2016), pp. 49 –60.

[37] Yabing He, Rajamani Krishna, and Banglin Chen. "Metal-organic Frameworks with Potential for Energy-efficient Adsorptive Separation of Light Hydrocarbons." In: *Energy Environ. Sci.* 5 (10 2012), pp. 9107–9120.

[38] Miguel Angelo da Silva Jorge. "Molecular simulation of the adsorption of water." In: (2003).

[39] Roman Petrenko and Jaroslaw Meller. "Molecular Dynamics." In: *ENCYCLOPEDIA OF LIFE SCIENCES* (2001), pp. 1–8.

[40] T.L. Hill. *An Introduction to Statistical Thermodynamics*. Addison-Wesley series in chemistry. Dover Publications, 1960. ISBN: 9780486652429.

[41] Daan Frenkel and Berend Smit. "Chapter 3 - Monte Carlo Simulations." In: *Understanding Molecular Simulation (Second Edition)*. Ed. by Daan Frenkel and Berend Smit. Second Edition. San Diego: Academic Press, 2002, pp. 23 –163.

[42] Nicholas Metropolis, Arianna W. Rosenbluth, Marshall N. Rosenbluth, Augusta H. Teller, and Edward Teller. "Equation of State Calculations by Fast Computing Machines." In: *The Journal of Chemical Physics* 21.6 (1953), pp. 1087–1092.

[43] M. Tuckerman. *Statistical Mechanics: Theory and Molecular Simulation*. Oxford Graduate Texts. OUP Oxford, 2010. ISBN: 9780191523465.

[44] "The classical equation of state of gaseous helium, neon and argon." In: *Proceedings of the Royal Society of London A: Mathematical, Physical and Engineering Sciences* 168.933 (1938), pp. 264–283.

[45] Philip M. Morse. "Diatomic Molecules According to the Wave Mechanics. II. Vibrational Levels." In: *Phys. Rev.* 34 (1 1929), pp. 57–64.

[46] Tony Pham, Katherine A. Forrest, Adam Hogan, Keith McLaughlin, Jonathan L. Belof, Juergen Eckert, and Brian Space. "Simulations of hydrogen sorption in rht-MOF-1: identifying the binding sites through explicit polariza-

tion and quantum rotation calculations." In: *J. Mater. Chem. A* 2 (7 2014), pp. 2088–2100.

[47] Abdulnour Y. Toukmaji and John A. Board Jr. "Ewald summation techniques in perspective: a survey." In: *Computer Physics Communications* 95.2–3 (1996), pp. 73 –92.

[48] Hark Lee and Wei Cai. "Ewald summation for Coulomb interactions in a periodic supercell." In: *Lecture Notes, Stanford University* 3.1 (2009), pp. 1–12.

[49] D. Wolf, P. Keblinski, S. R. Phillpot, and J. Eggebrecht. "Exact method for the simulation of Coulombic systems by spherically truncated, pairwise $r^{-1}$ summation." In: *The Journal of Chemical Physics* 110.17 (1999).

[50] Eleftherios E. Gdoutos, Ravi Agrawal, and Horacio D. Espinosa. "Comparison of the Ewald and Wolf methods for modeling electrostatic interactions in nanowires." In: *International Journal for Numerical Methods in Engineering* 84.13 (2010), pp. 1541–1551.

[51] De-Li Chen, Abraham C. Stern, Brian Space, and J. Karl Johnson. "Atomic Charges Derived from Electrostatic Potentials for Molecular and Periodic Systems." In: *The Journal of Physical Chemistry A* 114.37 (2010). PMID: 20795694, pp. 10225–10233.

[52] Randall Q. Snurr, Alexis T. Bell, and Doros N. Theodorou. "Prediction of Adsorption of Aromatic Hydrocarbons in Silicalite from Grand Canonical Monte Carlo Simulations with Biased Insertions." In: *The Journal of Physical Chemistry* 97.51 (1993), pp. 13742–13752.

[53] Marcus G. Martin and J. Ilja Siepmann. "Transferable Potentials for Phase Equilibria. 1. United-Atom Description of n-Alkanes." In: *The Journal of Physical Chemistry B* 102.14 (1998), pp. 2569–2577.

[54] Collin D Wick, Marcus G Martin, and J Ilja Siepmann. "Transferable Potentials for Phase Equilibria. 4. United-atom Description of Linear and Branched Alkenes and Alkylbenzenes." In: *The Journal of Physical Chemistry B* 104.33 (2000), pp. 8008–8016.

[55] A. K. Rappe, C. J. Casewit, K. S. Colwell, W. A. Goddard, and W. M. Skiff. "UFF, A Full Periodic Table Force Field for Molecular Mechanics and Molecular Dynamics Simulations." In: *Journal of the American Chemical Society* 114.25 (1992), pp. 10024–10035.

[56] Stephen L. Mayo, Barry D. Olafson, and William A. Goddard. "DREIDING: A Generic Force Field for Molecular Simulations." In: *The Journal of Physical Chemistry* 94.26 (1990), pp. 8897–8909.

[57] Allison L. Dzubak, Li-Chiang Lin, Jihan Kim, Joseph A. Swisher, Roberta Poloni, Sergey N. Maximoff, Berend Smit, and Laura Gagliardi. "Ab Initio Carbon Capture in Open-Site Metal-Organic Frameworks." In: *Nature Chemistry* 4 (2012), pp. 810–816.

[58] Christopher Campbell, Carlos A. Ferreiro-Rangel, Michael Fischer, José R. B. Gomes, and Miguel Jorge. "A Transferable Model for Adsorption in MOFs with Unsaturated Metal Sites." In: *The Journal of Physical Chemistry C* 121.1 (2017), pp. 441–458.

[59] Christopher E. Wilmer, Ki Chul Kim, and Randall Q. Snurr. "An Extended Charge Equilibration Method." In: *The Journal of Physical Chemistry Letters* 3.17 (2012). PMID: 26292141, pp. 2506–2511.

[60] Dalar Nazarian, Jeffrey S. Camp, and David S. Sholl. "A Comprehensive Set of High-Quality Point Charges for Simulations of Metal-Organic Frameworks." In: *Chemistry of Materials* 28.3 (2016), pp. 785–793.

[61] A. L. Myers and P. A. Monson. "Adsorption in Porous Materials at High Pressure: Theory and Experiment." In: *Langmuir* 18.26 (2002), pp. 10261–10273.

[62] Jorge Kohanoff. "Density functional theory." In: *Electronic Structure Calculations for Solids and Molecules: Theory and Computational Methods*. Cambridge University Press, 2006, 51–74.

[63] Takao Tsuneda. "Exchange-Correlation Functionals." In: *Density Functional Theory in Quantum Chemistry*. Tokyo: Springer Japan, 2014, pp. 1–124.

[64] H. Eschrig. *The fundamentals of density functional theory*. Teubner-Texte zur Physik. Teubner, 1996. ISBN: 9783815430309.

[65] R.M. Martin. *Electronic Structure: Basic Theory and Practical Methods*. Cambridge University Press, 2004. ISBN: 9780521782852.

[66] Astrid Marthinsen. "Fundamentals and applications of density functional theory."

[67] W. Kohn and L. J. Sham. "Self-Consistent Equations Including Exchange and Correlation Effects." In: *Phys. Rev.* 140 (4A 1965), A1133–A1138.

[68] I. Kondov. *Multiscale Modelling Methods for Applications in Materials Science: CECAM Tutorial, 16-20 September 2013, Forschungszentrum Jülich, Lecture Notes*. Schriften des Forschungszentrums Jülich: IAS series. Forschungszentrum Jülich, Zentralbibliothek, 2013. ISBN: 9783893368990.

[69] Sergio Tosoni, Christian Tuma, Joachim Sauer, Bartolomeo Civalleri, and Piero Ugliengo. "A comparison between plane wave and Gaussian-type orbital basis sets for hydrogen bonded systems: Formic acid as a test case." In: *The Journal of Chemical Physics* 127.15 (2007), p. 154102.

[70] Ernest R. Davidson and David Feller. "Basis set selection for molecular calculations." In: *Chemical Reviews* 86.4 (1986), pp. 681–696.

[71] S.F. Boys and F. Bernardi. "The calculation of small molecular interactions by the differences of separate total energies. Some procedures with reduced errors." In: *Molecular Physics* 19.4 (1970), pp. 553–566.

[72] N.W. Ashcroft and N.D. Mermin. *Solid state physics*. Science: Physics. Saunders College, 1976. ISBN: 9780030493461.

[73] T. Daniel Crawford and Henry F. Schaefer. "An Introduction to Coupled Cluster Theory for Computational Chemists." In: *Reviews in Computational Chemistry*. John Wiley & Sons, Inc., 2007, pp. 33–136.

[74] E.G. Lewars. *Computational Chemistry: Introduction to the Theory and Applications of Molecular and Quantum Mechanics*. Springer International Publishing, 2016. ISBN: 9783319309163.

[75] D. R. Hartree. "The Wave Mechanics of an Atom with a Non-Coulomb Central Field. Part 2. Some Results and Discussion." In: *Mathematical Proceedings of the Cambridge Philosophical Society* 24.1 (1928), pp. 111–132.

[76] Lev Sarkisov and Alex Harrison. "Computational Structure Characterisation Tools in Application to Ordered and Pisordered porous Materials." In: *Molecular Simulation* 37.15 (2011), pp. 1248–1257.

[77] Eric D. Bloch, Wendy L. Queen, Rajamani Krishna, Joseph M. Zadrozny, Craig M. Brown, and Jeffrey R. Long. "Hydrocarbon Separations in a Metal-Organic Framework with Open Iron(II) Coordination Sites." In: *Science* 335.6076 (2012), pp. 1606–1610.

[78] Seda Keskin, Jinchen Liu, Rees B. Rankin, J. Karl Johnson, and David S. Sholl. "Progress, Opportunities, and Challenges for Applying Atomically Detailed Modeling to Molecular Adsorption and Transport in Metal-Organic Framework Materials." In: *Industrial & Engineering Chemistry Research* 48.5 (2009), pp. 2355–2371.

[79] Qingyuan Yang, and Chongli Zhong. "Molecular Simulation of Adsorption and Diffusion of Hydrogen in Metal-Organic Frameworks." In: *The Journal of Physical Chemistry B* 109.24 (2005), pp. 11862–11864.

[80] Alper Uzun and Seda Keskin. "Site Characteristics in Metal Organic Frameworks for Gas Adsorption." In: *Progress in Surface Science* 89.1 (2014), pp. 56 –79.

[81] Yang Liu, Jing Liu, and Y.S. Lin. "Strong Binding Site Molarity of MOFs and its Effect on $CO_2$ Adsorption." In: *Microporous and Mesoporous Materials* 214 (2015), pp. 242 –245.

[82] Mircea Dincă, Anne Dailly, Yun Liu, Craig M. Brown, Dan. A. Neumann, and Jeffrey R. Long. "Hydrogen Storage in a Microporous Metal-Organic Framework with Exposed Mn2+ Coordination Sites." In: *Journal of the American Chemical Society* 128.51 (2006), pp. 16876–16883.

[83] Carlos A. Grande and Alírio E. Rodrigues. "Propane/Propylene Separation by Pressure Swing Adsorption Using Zeolite 4A." In: *Industrial & Engineering Chemistry Research* 44.23 (2005), pp. 8815–8829.

[84] J. S. Dewar. "A review of the pi-Complex Theory." In: *Bull. Soc. Chim. Fr* 18 (1951), pp. C71–C19.

[85] J. Chatt and L. A. Duncanson. "586. Olefin Co-ordination Compounds. Part III. Infra-red Spectra and Structure: Attempted Preparation of Acetylene Complexes." In: *J. Chem. Soc.* (0 1953), pp. 2939–2947.

[86] Nabil Lamia, Miguel Jorge, Miguel A. Granato, Filipe A. Almeida Paz, Hubert Chevreau, and Alírio E. Rodrigues. "Adsorption of Propane, Propylene and Isobutane on a Metal-Organic Framework: Molecular Simulation and Experiment." In: *Chemical Engineering Science* 64.14 (2009), pp. 3246 –3259.

[87] Miguel Jorge, Nabil Lamia, and Alírio E. Rodrigues. "Molecular Simulation of Propane/Propylene Separation on the Metal-Organic Framework CuBTC." In: *Colloids and Surfaces A: Physicochemical and Engineering Aspects* 357.1–3 (2010), pp. 27 –34.

[88] Pragya Verma, Xuefei Xu, and Donald G. Truhlar. "Adsorption on Fe-MOF-74 for C1-C3 Hydrocarbon Separation." In: *The Journal of Physical Chemistry C* 117.24 (2013), pp. 12648–12660.

[89] Juan Manuel Castillo, Thijs J. H. Vlugt, and Sofìa Calero. "Understanding Water Adsorption in Cu-BTC Metal-Organic Frameworks." In: *The Journal of Physical Chemistry C* 112.41 (2008), pp. 15934–15939.

[90] Michael Fischer, Frank Hoffmann, and Michael Fröba. "Metal-Organic Frameworks and Related Materials for Hydrogen Purification: Interplay of Pore Size and Pore Wall Polarity." In: *RSC Adv.* 2 (10 2012), pp. 4382–4396.

[91] Tim M. Becker, Jurn Heinen, David Dubbeldam, Li-Chiang Lin, and Thijs J. H. Vlugt. "Polarizable Force Fields for $CO_2$ and $CH_4$ Adsorption in M-MOF-74." In: *The Journal of Physical Chemistry C* 121.8 (2017), pp. 4659–4673.

[92] Linjiang Chen, Lukáš Grajciar, Petr Nachtigall, and Tina Düren. "Accurate Prediction of Methane Adsorption in a Metal-Organic Framework with Unsaturated Metal Sites by Direct Implementation of an ab Initio Derived Potential Energy Surface in GCMC Simulation." In: *The Journal of Physical Chemistry C* 115.46 (2011), pp. 23074–23080.

[93] A. Luna-Triguero, J. M. Vicent-Luna, P. Gómez-Álvarez, and S. Calero. "Olefin/-Paraffin Separation in Open Metal Site Cu-BTC Metal-Organic Framework." In: *The Journal of Physical Chemistry C* 121.5 (2017), pp. 3126–3132.

[94] Katherine A. Forrest, Tony Pham, Keith McLaughlin, Jonathan L. Belof, Abraham C. Stern, Michael J. Zaworotko, and Brian Space. "Simulation of the Mechanism of Gas Sorption in a Metal–Organic Framework with Open Metal Sites: Molecular Hydrogen in PCN-61." In: *The Journal of Physical Chemistry C* 116.29 (2012), pp. 15538–15549.

[95] Douglas Franz, Katherine A. Forrest, Tony Pham, and Brian Space. "Accurate $H_2$ Sorption Modeling in the rht-MOF NOTT-112 Using Explicit Polarization." In: *Crystal Growth & Design* 16.10 (2016), pp. 6024–6032.

[96] F. Coester and H. Kümmel. "Short-range correlations in nuclear wave functions." In: *Nuclear Physics* 17.Supplement C (1960), pp. 477 –485.

[97] Joshua Borycz, Davide Tiana, Emmanuel Haldoupis, Jeffrey C. Sung, Omar K. Farha, J. Ilja Siepmann, and Laura Gagliardi. "$CO_2$ Adsorption in M-IRMOF-10 (M = Mg, Ca, Fe, Cu, Zn, Ge, Sr, Cd, Sn, Ba)." In: *The Journal of Physical Chemistry C* 120.23 (2016), pp. 12819–12830.

[98] Joshua Borycz, Li-Chiang Lin, Eric D. Bloch, Jihan Kim, Allison L. Dzubak, Rémi Maurice, David Semrouni, Kyuho Lee, Berend Smit, and Laura Gagliardi. "$CO_2$ Adsorption in $Fe_2$(dobdc): A Classical Force Field Parameterized from Quantum Mechanical Calculations." In: *The Journal of Physical Chemistry C* 118.23 (2014), pp. 12230–12240.

[99] Hyun Seung Koh, Malay Kumar Rana, Antek G. Wong-Foy, and Donald J. Siegel. "Predicting Methane Storage in Open-Metal-Site Metal–Organic Frameworks." In: *The Journal of Physical Chemistry C* 119.24 (2015), pp. 13451–13458.

[100] Rocio Mercado et al. "Force Field Development from Periodic Density Functional Theory Calculations for Gas Separation Applications Using Metal–Organic Frameworks." In: *The Journal of Physical Chemistry C* 120.23 (2016), pp. 12590–12604.

[101] Jurn Heinen, Nicholas C. Burtch, Krista S. Walton, Célia Fonseca Guerra, and David Dubbeldam. "Predicting Multicomponent Adsorption Isotherms in Open-Metal Site Materials Using Force Field Calculations Based on Energy Decomposed Density Functional Theory." In: *Chemistry - A European Journal* 22.50 (2016), pp. 18045–18050.

[102] C. Fonseca Guerra, J. G. Snijders, G. te Velde, and E. J. Baerends. "Towards an order-N DFT method." In: *Theoretical Chemistry Accounts* 99.6 (1998), pp. 391–403.

[103] G. te Velde, F. M. Bickelhaupt, E. J. Baerends, C. Fonseca Guerra, S. J. A. van Gisbergen, J. G. Snijders, and T. Ziegler. "Chemistry with ADF." In: *Journal of Computational Chemistry* 22.9 (2001), pp. 931–967.

[104] Ambarish R. Kulkarni and David S. Sholl. "Screening of Copper Open Metal Site MOFs for Olefin/Paraffin Separations Using DFT-Derived Force Fields." In: *The Journal of Physical Chemistry C* 120.40 (2016), pp. 23044–23054.

[105] Michael Fischer, Frank Hoffmann, and Michael Fröba. "New Microporous Materials for Acetylene Storage and $C_2H_2/CO_2$ Separation: Insights from Molecular Simulations." In: *ChemPhysChem* 11.10 (2010), pp. 2220–2229.

[106] Jürg Hutter, Marcella Iannuzzi, Florian Schiffmann, and Joost VandeVondele. "cp2k: atomistic simulations of condensed matter systems." In: *Wiley Interdisciplinary Reviews: Computational Molecular Science* 4.1 (2014), pp. 15–25.

[107] C. Hartwigsen, S. Goedecker, and J. Hutter. "Relativistic Separable Dual-space Gaussian Pseudopotentials from H to Rn." In: *Phys. Rev. B* 58 (7 1998), pp. 3641–3662.

[108] John P. Perdew, Kieron Burke, and Matthias Ernzerhof. "Generalized Gradient Approximation Made Simple." In: *Phys. Rev. Lett.* 77 (18 1996), pp. 3865–3868.

[109] Michael Fischer, Bogdan Kuchta, Lucyna Firlej, Frank Hoffmann, and Michael Fröba. "Accurate Prediction of Hydrogen Adsorption in Metal-Organic Frameworks with Unsaturated Metal Sites via a Combined Density-Functional Theory and Molecular Mechanics Approach." In: *The Journal of Physical Chemistry C* 114.44 (2010), pp. 19116–19126.

[110] Joao P. Prates Ramalho, José R. B. Gomes, and Francesc Illas. "Accounting for van der Waals Interactions Between Adsorbates and Surfaces in Density Functional Theory Based Calculations: Selected Examples." In: *RSC Adv.* 3 (32 2013), pp. 13085–13100.

[111] Alexandre Tkatchenko and O. Anatole von Lilienfeld. "Adsorption of Ar on Graphite using London Dispersion Forces Corrected Kohn-Sham Density Functional Theory." In: *Phys. Rev. B* 73 (15 2006), p. 153406.

[112] Erin R. Johnson, Iain D. Mackie, and Gino A. DiLabio. "Dispersion Interactions in Density-functional Theory." In: *Journal of Physical Organic Chemistry* 22.12 (2009), pp. 1127–1135.

[113] M. Krack. "Pseudopotentials for H to Kr Optimized for Gradient-Corrected Exchange-Correlation Functionals." In: *Theoretical Chemistry Accounts* 114.1 (2005), pp. 145–152.

[114] S. Goedecker, M. Teter, and J. Hutter. "Separable Dual-space Gaussian Pseudopotentials." In: *Phys. Rev. B* 54 (3 1996), pp. 1703–1710.

[115] B. Delley. "An All-Electron Numerical Method for Solving the Local Density Functional for Polyatomic Molecules." In: *The Journal of Chemical Physics* 92.1 (1990), pp. 508–517.

[116] B. Delley. "From Molecules to Solids with the DMol3 Approach." In: *The Journal of Chemical Physics* 113.18 (2000), pp. 7756–7764.

[117] Accelrys Inc. *Material Studio Version 5*. 2011. URL: `http://accelrys.com/products/collaborative-science/biovia-materials-studio/`.

[118] John D. Weeks, David Chandler, and Hans C. Andersen. "Role of Repulsive Forces in Determining the Equilibrium Structure of Simple Liquids." In: *The Journal of Chemical Physics* 54.12 (1971), pp. 5237–5247.

[119] J.D. Weeks D. Chandler and H.C. Andersen. "van der Waals Picture of Liquids, Solids, and Phase Transformations." In: *Science* 220 (1983), pp. 787–794.

[120] Amit Gupta, Shaji Chempath, Martin J. Sanborn, Louis A. Clark, and Randall Q. Snurr. "Object-oriented Programming Paradigms for Molecular Modeling." In: *Molecular Simulation* 29.1 (2003), pp. 29–46.

[121] Ding Yu Peng and Donald B. Robinson. "A New Two-Constant Equation of State." In: *Industrial & Engineering Chemistry Fundamentals* 15.1 (1976), pp. 59–64.

[122] Hanjun Fang, Hakan Demir, Preeti Kamakoti, and David S. Sholl. "Recent developments in first-principles force fields for molecules in nanoporous materials." In: *J. Mater. Chem. A* 2 (2 2014), pp. 274–291.

[123] Derya Dokur and Seda Keskin. "Effects of Force Field Selection on the Computational Ranking of MOFs for $CO_2$ Separations." In: *Industrial & Engineering Chemistry Research* 57.6 (2018), pp. 2298–2309.

[124] Jared B. DeCoste, Gregory W. Peterson, Bryan J. Schindler, Kato L. Killops, Matthew A. Browe, and John J. Mahle. "The Effect of Water Adsorption on the Structure of the Carboxylate Containing Metal-Organic Frameworks Cu-BTC, Mg-MOF-74, and UiO-66." In: *The Journal of Materials Chemistry A* 1 (38 2013), pp. 11922–11932.

[125] Stefan Marx, Wolfgang Kleist, and Alfons Baiker. "Synthesis, Structural Properties, and Catalytic Behavior of Cu-BTC and Mixed-Linker Cu-BTC-PyDC in the Oxidation of Benzene Derivatives." In: *Journal of Catalysis* 281.1 (2011), pp. 76 –87.

[126] Michael Fischer. "Molecular Simulations of Hydrogen Storage and Gas Separation in Metal-Organic Frameworks." eng. PhD thesis. Universität Hamburg, 2011.

[127] Lukáš Grajciar, Andrew D. Wiersum, Philip L. Llewellyn, Jong-San Chang, and Petr Nachtigall. "Understanding $CO_2$ Adsorption in CuBTC MOF: Comparing Combined DFT-ab Initio Calculations with Microcalorimetry Experiments." In: *The Journal of Physical Chemistry C* 115.36 (2011), pp. 17925–17933.

[128] Charles Edwin Webster, Russell S. Drago, and Michael C. Zerner. "Molecular Dimensions for Adsorptives." In: *Journal of the American Chemical Society* 120.22 (1998), pp. 5509–5516.

[129] Yunxia Hu, Shengchang Xiang, Wenwei Zhang, Zhuxiu Zhang, Lei Wang, Junfeng Bai, and Banglin Chen. "A new MOF-505 Analog Exhibiting High Acetylene Storage." In: *Chem. Commun.* (48 2009), pp. 7551–7553.

[130] Daofeng Sun, Shengqian Ma, Jason M. Simmons, Jian-Rong Li, Daqiang Yuan, and Hong-Cai Zhou. "An Unusual Case of Symmetry-Preserving Isomerism." In: *Chem. Commun.* 46 (8 2010), pp. 1329–1331.

[131] Mian Li, Dan Li, Michael O'Keeffe, and Omar M. Yaghi. "Topological Analysis of Metal-Organic Frameworks with Polytopic Linkers and/or Multiple Building Units and the Minimal Transitivity Principle." In: *Chemical Reviews* 114.2 (2014), pp. 1343–1370.

[132] Jason M. Simmons, Hui Wu, Wei Zhou, and Taner Yildirim. "Carbon Capture in Metal-Organic Frameworks-A Comparative Study." In: *Energy Environ. Sci.* 4 (6 2011), pp. 2177–2185.

[133] Xiang Lin, Junhua Jia, Xuebo Zhao, K. Mark Thomas, Alexander J. Blake, Gavin S. Walker, Neil R. Champness, Peter Hubberstey, and Martin Schröder. "High $H_2$ Adsorption by Coordination-Framework Materials." In: *Angewandte Chemie International Edition* 45.44 (2006), pp. 7358–7364.

[134] Banglin Chen, Nathan W. Ockwig, Andrew R. Millward, Damacio S. Contreras, and Omar M. Yaghi. "High $H_2$ Adsorption in a Microporous Metal-Organic Framework with Open Metal Sites." In: *Angewandte Chemie* 117.30 (2005), pp. 4823–4827.

[135] Jingjing Jiao, Huimin Liu, Dongjie Bai, and Yabing He. "A Chemically Cross-Linked NbO-Type Metal-Organic Framework: Cage or Window Partition?" In: *Inorganic Chemistry* 55.8 (2016), pp. 3974–3979.

[136] Antek G. Wong-Foy, Olivier Lebel, and Adam J. Matzger. "Porous Crystal Derived from a Tricarboxylate Linker with Two Distinct Binding Motifs." In: *Journal of the American Chemical Society* 129.51 (2007), pp. 15740–15741.

[137] Zhiyong Guo, Hui Wu, Gadipelli Srinivas, Yaming Zhou, Shengchang Xiang, Zhenxia Chen, Yongtai Yang, Wei Zhou, Michael O'Keeffe, and Banglin Chen. "A Metal-Organic Framework with Optimized Open Metal Sites and Pore Spaces for High Methane Storage at Room Temperature." In: *Angewandte Chemie International Edition* 50.14 (2011), pp. 3178–3181.

[138] Nadeen Al-Janabi, Xiaolei Fan, and Flor R. Siperstein. "Assessment of MOF's Quality: Quantifying Defect Content in Crystalline Porous Materials." In: *The Journal of Physical Chemistry Letters* 7.8 (2016), pp. 1490–1494.

[139] D.M. Ruthven. *Principles of Adsorption and Adsorption Processes*. Wiley-Interscience publication. Wiley, 1984. Chap. 4. ISBN: 9780471866060.

[140] A. L. Myers and J. M. Prausnitz. "Thermodynamics of mixed-gas adsorption." In: *AIChE Journal* 11.1 (1965), pp. 121–127.

[141] Jiahui Chen, Leslie S. Loo, and Kean Wang. "An Ideal Absorbed Solution Theory (IAST) Study of Adsorption Equilibria of Binary Mixtures of Methane and Ethane on a Templated Carbon." In: *Journal of Chemical & Engineering Data* 56.4 (2011), pp. 1209–1212.

[142] Bei Liu, Berend Smit, Fernando Rey, Susana Valencia, and Sofía Calero. "A New United Atom Force Field for Adsorption of Alkenes in Zeolites." In: *The Journal of Physical Chemistry C* 112.7 (2008), pp. 2492–2498.

[143] D. Dubbeldam, S. Calero, T. J. H. Vlugt, R. Krishna, T. L. M. Maesen, and B. Smit. "United Atom Force Field for Alkanes in Nanoporous Materials." In: *The Journal of Physical Chemistry B* 108.33 (2004), pp. 12301–12313.

[144] F. SIPERSTEIN, A.L. MYERS, and O. TALU. "Long range corrections for computer simulations of adsorption." In: *Molecular Physics* 100.13 (2002), pp. 2025–2030.

[145] Vanessa F.D. Martins, Ana M. Ribeiro, Alexandre Ferreira, U-Hwang Lee, Young Kyu Hwang, Jong-San Chang, José M. Loureiro, and Alírio E. Rodrigues. "Ethane/ethylene separation on a copper benzene-1,3,5-tricarboxylate MOF." In: *Separation and Purification Technology* 149.Supplement C (2015), pp. 445 –456.

[146] Qing Min Wang, Dongmin Shen, Martin Bülow, Miu Ling Lau, Shuguang Deng, Frank R. Fitch, Norberto O. Lemcoff, and Jessica Semanscin. "Metallo-organic molecular sieve for gas separation and purification." In: *Microporous and Mesoporous Materials* 55.2 (Sept. 2002), pp. 217–230.

[147] Krista S. Walton and David S. Sholl. "Predicting multicomponent adsorption: 50 years of the ideal adsorbed solution theory." In: *AIChE Journal* 61.9 (2015), pp. 2757–2762.

[148] J.G. Speight. *Handbook of Industrial Hydrocarbon Processes*. Elsevier Science, 2010. ISBN: 9780080942711.

[149] U.S. Department of Labor Occupational Safety and Health Administration. *Workplace Safety and Health Topics- CARBON MONOXIDE*. 2002. URL: `https://www.cdc.gov/niosh/topics/co-comp/default.html` (visited on 10/10/2017).

[150] Jürgen Bierhals. "Carbon Monoxide." In: *Ullmann's Encyclopedia of Industrial Chemistry*. Wiley-VCH Verlag GmbH and Co. KGaA, 2000. ISBN: 9783527306732. DOI: 10.1002/14356007.a05_203.

[151] M. Peer, S. Mehdi Kamali, M. Mahdeyarfar, and T. Mohammadi. "Separation of Hydrogen from Carbon Monoxide Using a Hollow Fiber Polyimide Membrane: Experimental and Simulation." In: *Chemical Engineering and Technology* 30.10 (2007), pp. 1418–1425.

[152] National Center for Biotechnology Information. *PubChem Compound*. 2016. URL: https://pubchem.ncbi.nlm.nih.gov/compound (visited on 10/10/2017).

[153] S. Bordiga, L. Regli, F. Bonino, E. Groppo, C. Lamberti, B. Xiao, P. S. Wheatley, R. E. Morris, and A. Zecchina. "Adsorption properties of HKUST-1 toward hydrogen and other small molecules monitored by IR." In: *Phys. Chem. Chem. Phys.* 9 (21 2007), pp. 2676–2685.

[154] Janos Szanyi, Marco Daturi, Guillaume Clet, Donald R. Baer, and Charles H. F. Peden. "Well-studied Cu-BTC still serves surprises: evidence for facile Cu2+/Cu+ interchange." In: *Phys. Chem. Chem. Phys.* 14 (13 2012), pp. 4383–4390.

[155] Andrew Sirjoosingh, Saman Alavi, and Tom K. Woo. "Grand-Canonical Monte Carlo and Molecular-Dynamics Simulations of Carbon-Dioxide and Carbon-Monoxide Adsorption in Zeolitic Imidazolate Framework Materials." In: *The Journal of Physical Chemistry C* 114.5 (2010), pp. 2171–2178.

[156] Jagadeswara R. Karra and Krista S. Walton. "Effect of Open Metal Sites on Adsorption of Polar and Nonpolar Molecules in Metal-Organic Framework Cu-BTC." In: *Langmuir* 24.16 (2008). PMID: 18630977, pp. 8620–8626.

[157] Ana Martíin-Calvo, Francisco D. Lahoz-Martín, and Sofía Calero. "Understanding Carbon Monoxide Capture Using Metal-Organic Frameworks." In: *The Journal of Physical Chemistry C* 116.11 (2012), pp. 6655–6663.

[158] L. Valenzano, B. Civalleri, S. Chavan, G. T. Palomino, C. O. Areán, and S. Bordiga. "Computational and Experimental Studies on the Adsorption of CO, $N_2$, and $CO_2$ on Mg-MOF-74." In: *The Journal of Physical Chemistry C* 114.25 (2010), pp. 11185–11191.

[159] Jagadeswara R. Karra and Krista S. Walton. "Molecular Simulations and Experimental Studies of $CO_2$, CO, and $N_2$ Adsorption in Metal-Organic Frameworks." In: *The Journal of Physical Chemistry C* 114.37 (2010), pp. 15735–15740.

[160] Martin Walker, Andrew J. A. Harvey, Ananya Sen, and Caroline E. H. Dessent. "Performance of M06, M06-2X, and M06-HF Density Functionals for Conformationally Flexible Anionic Clusters: M06 Functionals Perform Better than B3LYP for a Model System with Dispersion and Ionic Hydrogen-Bonding Interactions." In: *The Journal of Physical Chemistry A* 117.47 (2013). PMID: 24147965, pp. 12590–12600.

[161] Kyuho Lee, Éamonn D. Murray, Lingzhu Kong, Bengt I. Lundqvist, and David C. Langreth. "Higher-accuracy van der Waals density functional." In: *Phys. Rev. B* 82 (8 2010), p. 081101.

[162] Stefan Grimme. "Semiempirical GGA-type density functional constructed with a long-range dispersion correction." In: *Journal of Computational Chemistry* 27.15 (2006), pp. 1787–1799.

[163] Rosendo Valero, José R. B. Gomes, Donald G. Truhlar, and Francesc Illas. "Density functional study of CO and NO adsorption on Ni-doped MgO(100)." In: *The Journal of Chemical Physics* 132.10 (2010), p. 104701.

[164] Sijie Luo, Yan Zhao, and Donald G. Truhlar. "Improved CO Adsorption Energies, Site Preferences, and Surface Formation Energies from a Meta-Generalized Gradient Approximation Exchange–Correlation Functional, M06-L." In: *The Journal of Physical Chemistry Letters* 3.20 (2012). PMID: 26292236, pp. 2975–2979.

[165] Lara Ferrighi, Georg K. H. Madsen, and Bjørk Hammer. "Self-consistent meta-generalized gradient approximation study of adsorption of aromatic molecules on noble metal surfaces." In: *The Journal of Chemical Physics* 135.8 (2011), p. 084704.

[166] Yan Zhao and Donald G. Truhlar. "The M06 suite of density functionals for main group thermochemistry, thermochemical kinetics, noncovalent interactions, excited states, and transition elements: two new functionals and

systematic testing of four M06-class functionals and 12 other functionals." In: *Theoretical Chemistry Accounts* 120.1 (2008), pp. 215–241.

[167] Paolo Giannozzi et al. "QUANTUM ESPRESSO: a modular and open-source software project for quantum simulations of materials." In: *Journal of Physics: Condensed Matter* 21.39 (2009), p. 395502.

[168] M. J. Frisch et al. *Gaussian 16 Revision A.03*. Gaussian Inc. Wallingford CT. 2016.

[169] Yan Zhao and Donald G. Truhlar. "A new local density functional for main-group thermochemistry, transition metal bonding, thermochemical kinetics, and noncovalent interactions." In: *The Journal of Chemical Physics* 125.19 (2006), p. 194101.

[170] Quantum Espresso. *Pseudopotentials*. 2017. URL: `http://www.quantum-espresso.org/pseudopotentials/` (visited on 10/10/2017).

[171] Miroslav Rubeŝ, Lukáŝ Grajciar, Ota Bludský, Andrew D. Wiersum, Philip L. Llewellyn, and Petr Nachtigall. "Combined Theoretical and Experimental Investigation of CO Adsorption on Coordinatively Unsaturated Sites in CuBTC MOF." In: *ChemPhysChem* 13.2 (2012), pp. 488–495.

[172] Barbara Supronowicz, Andreas Mavrandonakis, and Thomas Heine. "Interaction of Small Gases with the Unsaturated Metal Centers of the HKUST-1 Metal Organic Framework." In: *The Journal of Physical Chemistry C* 117.28 (2013), pp. 14570–14578.

[173] Dalar Nazarian, Jeffrey S. Camp, Yongchul G. Chung, Randall Q. Snurr, and David S. Sholl. "Large-Scale Refinement of Metal-Organic Framework Structures Using Density Functional Theory." In: *Chemistry of Materials* 29.6 (2017), pp. 2521–2528.

[174] Jeffrey J. Potoff and J. Ilja Siepmann. "Vapor-liquid equilibria of mixtures containing alkanes, carbon dioxide, and nitrogen." In: *AIChE Journal* 47.7 (2001), pp. 1676–1682.

[175] Krista S. Walton and Randall Q. Snurr. "Applicability of the BET Method for Determining Surface Areas of Microporous Metal-Organic Frameworks." In: *Journal of the American Chemical Society* 129.27 (2007). PMID: 17580944, pp. 8552–8556.

[176] John E. Straub and Martin Karplus. "Molecular dynamics study of the photodissociation of carbon monoxide from myoglobin: Ligand dynamics in the first 10 ps." In: *Chemical Physics* 158.2 (1991), pp. 221 –248.

[177] J. Piper, J.A. Morrison, and C. Peters. "The adsorption of carbon monoxide on graphite." In: *Molecular Physics* 53.6 (1984), pp. 1463–1480.

[178] Hailian Li, Mohamed Eddaoudi, M. O'Keeffe, and Omar M. Yaghi. "Design and synthesis of an exceptionally stable and highly porous metal-organic framework." In: *Nature* 402 (1991), pp. 276–279.

[179] Dipendu Saha and Shuguang Deng. "Adsorption Equilibria and Kinetics of Carbon Monoxide on Zeolite 5A, 13X, MOF-5, and MOF-177." In: *Journal of Chemical & Engineering Data* 54.8 (2009), pp. 2245–2250.

[180] J. Rother and T. Fieback. "Multicomponent adsorption measurements on activated carbon, zeolite molecular sieve and metal–organic framework." In: *Adsorption* 19.5 (2013), pp. 1065–1074.

[181] Craig Mcanally. "Characterisation of Metal-Organic Frameworks with Inherent Functionalisation for Carbon Capture Methods." eng. PhD thesis. University of Strathclyde, 2017.

[182] Stephen D. Burd, Shengqian Ma, Jason A. Perman, Benjamin J. Sikora, Randall Q. Snurr, Praveen K. Thallapally, Jian Tian, Lukasz Wojtas, and Michael J. Zaworotko. "Highly Selective Carbon Dioxide Uptake by [Cu(bpy-n)$_2$(SiF$_6$)] (bpy-1 = 4,4'-Bipyridine; bpy-2 = 1,2-Bis(4-pyridyl)ethene)." In: *Journal of the American Chemical Society* 134.8 (2012). PMID: 22316279, pp. 3663–3666.

[183] Katherine A. Forrest et al. "Computational Studies of $CO_2$ Sorption and Separation in an Ultramicroporous Metal-Organic Material." In: *The Journal of Physical Chemistry C* 117.34 (2013), pp. 17687–17698.

[184] Katherine A. Forrest, Tony Pham, Patrick Nugent, Stephen D. Burd, Ashley Mullen, Lukasz Wojtas, Michael J. Zaworotko, and Brian Space. "Examining the Effects of Different Ring Configurations and Equatorial Fluorine Atom Positions on $CO_2$ Sorption in [Cu(bpy)$_2$SiF$_6$]." In: *Crystal Growth & Design* 13.10 (2013), pp. 4542–4548.

[185] Shin-ichiro Noro, Susumu Kitagawa, Mitsuru Kondo, and Kenji Seki. "A New, Methane Adsorbent, Porous Coordination Polymer [CuSiF6(4,4'-bipyridine)2n]." In: *Angewandte Chemie International Edition* 39.12 (2000), pp. 2081–2084.

[186] Tony Pham, Katherine A. Forrest, Keith McLaughlin, Brant Tudor, Patrick Nugent, Adam Hogan, Ashley Mullen, Christian R. Cioce, Michael J. Zaworotko, and Brian Space. "Theoretical Investigations of $CO_2$ and $H_2$ Sorption in an Interpenetrated Square-Pillared Metal-Organic Material." In: *The Journal of Physical Chemistry C* 117.19 (2013), pp. 9970–9982.

[187] Dalar Nazarian, P. Ganesh, and David S. Sholl. "Benchmarking density functional theory predictions of framework structures and properties in a chemically diverse test set of metal-organic frameworks." In: *J. Mater. Chem. A* 3 (44 2015), pp. 22432–22440.

[188] Li-Ming Yang, Ponniah Vajeeston, Ponniah Ravindran, Helmer Fjellvåg, and Mats Tilset. "Theoretical Investigations on the Chemical Bonding, Electronic Structure, And Optical Properties of the Metal-Organic Framework MOF-5." In: *Inorganic Chemistry* 49.22 (2010). PMID: 20961146, pp. 10283–10290.

[189] S.J. Gregg and K.S.W. Sing. *Adsorption, surface area, and porosity*. Academic Press, 1991. ISBN: 9780123009562.

[190] Ashleigh J. Fletcher, K. Mark Thomas, and Matthew J. Rosseinsky. "Flexibility in metal-organic framework materials: Impact on sorption properties." In: *Journal of Solid State Chemistry* 178.8 (2005). Reticular Chemistry: Design, Synthesis, Properties and Applications of Metal-Organic Polyhedra and Frameworks, pp. 2491 –2510.

[191] P. Llewellyn J. Rouquerol and F. Rouquerol. "Is the BET equation applicable to microporous adsorbents?" In: *Studies in Surface Science and Catalysis* 13.2 (2007), pp. 49–56.

[192] P. Nugent et al. "Porous Materials with Optimal Adsorption Thermodynamics and Kinetics for $CO_2$ Separation." In: *Nature* 495.7439 (2013), pp. 80–84.

# DECLARATION

I declare that this thesis is the result of the author's original research. The thesis has in full been composed by the author, and has not been previously submitted for examination which has led to the award of a degree.



*Glasgow, March 2018*

Christopher Campbell